



Université Mohamed Khider -BISKRA
Faculté des Sciences exactes et science
de la nature et de la vie
Département: science de la matière

جامعة محمد خيضر ببسكرة
كلية العلوم الدقيقة و علوم الطبيعة و الحياة
قسم: علوم المادة
المرجع:.....

Réf :.....

Thèse présentée en vue de l'obtention
du diplôme de :

Doctorat en sciences en: Physique

Option: Physique des Semi-conducteurs

Présenté par:

Mr. Soufiane BENHAMIDA

THEME

**Caractérisation Des Couches Minces D'oxyde De Nickel (NiO)
Elaboré Par Spray Pyrolyse**

Soutenue publiquement le : 21/ 11 / 2018

Devant le jury composé de :

M : Kamel Eddine AIADI	Professeur à l'Université d'Ouargla	Président
M : Rachid GHERIANI	Professeur à l'Université d'Ouargla	Examineur
M : Saïd LAKEL	Professeur à l'Université de Biskra	Examineur
M : Abdelkrim NAAS	MCA à l'Université de Djelfa	Examineur
M : Saïd BENRAMACHE	MCA à l'Université de Biskra	Examineur
M : Boubaker BEN HAOUA	Professeur à l'Université d'El oued	Rapporteur

Acknowledgements

First of all I thank the Almighty Allah, whose Grace enabled me to continue this work and overcome all difficulties and our prophet Mohammed (peace and blessings of Allah be upon him) who invites us to science and knowledge.

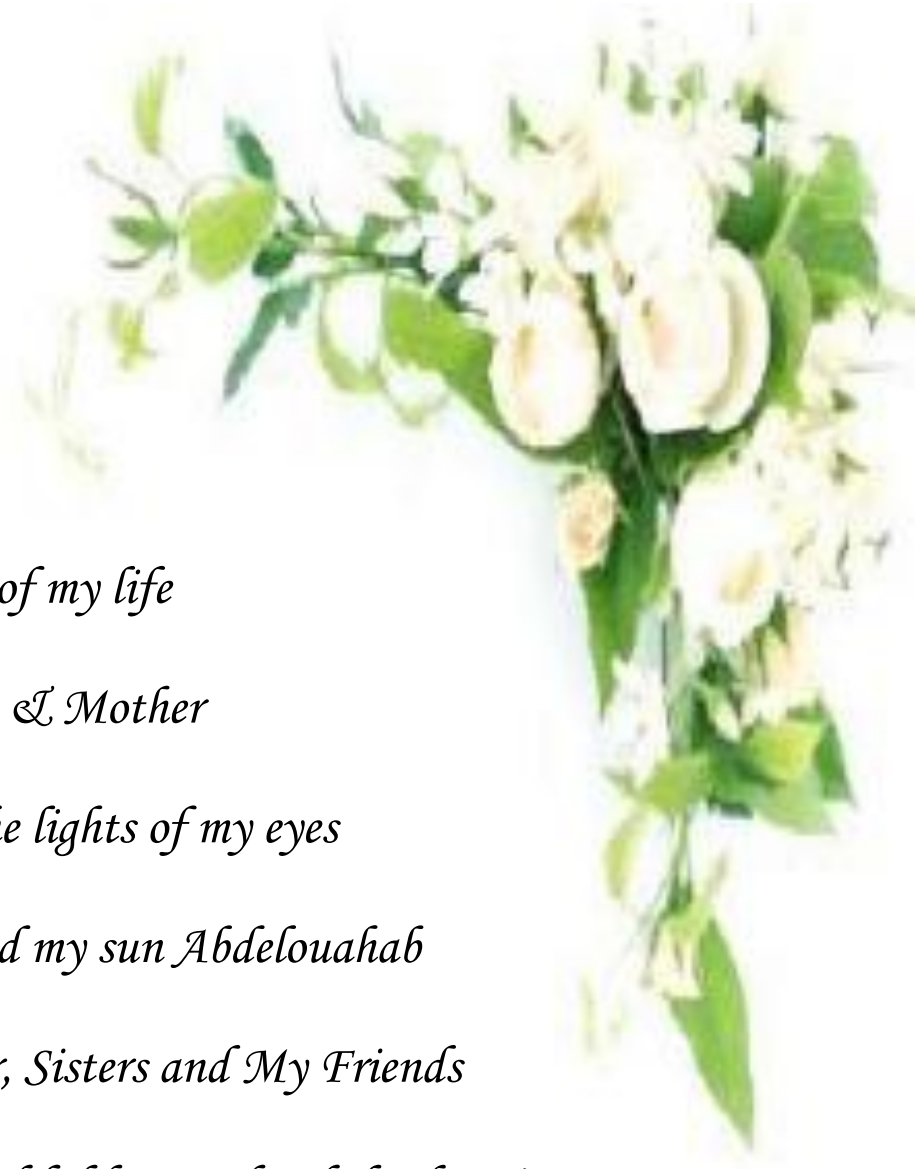
This thesis would not have been feasible without the guidance and the support of Several individuals who in one way or another contributed and extended their precious Assistance in the preparation and completion of this study

*First and foremost I would like to express the deepest gratitude to my research supervisor Prof. **Boubaker BENHAOUA** for his guidance and support. I express my deepest and heartfelt gratitude to him for the valuable guidance, timely suggestions, moral support and encouragement given by him during the course of the research work,*

*Besides, I owe my sincere thanks to the Prof. **Kamel Eddine AIADI**, Prof. **Rachid GHERJANI**, Prof. **Said LAKEF**, Dr. **Abdelkrim NAAS** and Dr. **Said BENRAMACHE**, for their acceptance to judge this modest work,*

*I am thankful to my colleagues of our VTRS laboratory Dr. **Achour RAHAL**, Dr. **Athmane BENHAOUA**; they have helped me immensely in several occasions.*

Soufiane BENHAMIDA



Dedication

To

The lights of my life

Father & Mother

The lights of my eyes

My wife and my son Abdelouahab

Brother, Sisters and My Friends

All faithful hearts that helped me in

The journey of my life.



Soufiane

Contents

Contents

Acknowledgements	
Dedication	
Contents	i
List of figures	v
List of tables	viii
General introduction	1

Chapter I : Literature Review and Technical Background

1.1 Introduction to transparent conducting oxides	7
1.2 History - Past, present and future of TCOs	7
1.3 Classification of TCOs	9
1.3.1 N-type TCOs	9
1.3.2 P-type TCOs	9
1.4 Basic properties of transparent conducting oxides	10
1.4.1 Electrical Conductivity	10
1.4.2 Optical properties	11
1.4.3 Defects and impurities in TCO materials	13
1.5 Intrinsic and extrinsic doping of TCOs	13
1.5.1 Intrinsic doping	13
1.5.2 Extrinsic doping	14
1.6 Figure of Merit for TCOs	14
1.7 Criteria for choosing TCOs	14
1.8 Application of TCOs	15
1.8.1 TCO Electrodes for Solar Cell Applications	15
1.8.2 Light and heat control	16
1.8.3 Transparent electronics	16
1.8.4 Photocatalysis application	18
1.8.5 Gas sensors	19
1.9 Fundamental properties of nickel oxide (NiO) material	19
1.9.1 Physical and Chemical Properties of NiO	19
1.9.2 Crystal structure	20
1.9.3 Nickel thermal oxidation	21
1.9.4 Defects and impurities in NiO crystal	22
1.9.5 Electronic structure	23
1.9.6 Optical properties	24
1.9.7 Electrical properties	24
1.9.8 Magnetic properties	26
1.10 NiO thin films	27
1.11 Review of earlier work done on NiO based thin films	27
1.11.1 Undoped NiO thin films	27
1.11.2 Doped NiO thin films	34
References	38

Chapter II : Synthesis, methods and materials characterization

2.1 Introduction	49
2.2 Mechanism of thin films formation	49
2.3 Thin Film Growth Process	49
2.3.1 Condensation	50
2.3.2 Nucleation	50
2.3.3 Growth	51
2.3.3.1 The Island Stage	51
2.3.3.2 The Coalescence Stage	51
2.3.3.3 The Channel Stage	52
2.3.3.4 Continuous Film Stage	52
2.4 Thin Film Deposition Techniques	52
2.5 Criteria for selection of a deposition technique	53
2.6 Physical method of deposition	53
2.6.1 RF Sputtering	54
2.6.2 Pulsed Laser Deposition	54
2.6.3 Thermal evaporation	55
2.7 Chemical method of deposition	55
2.7.1 Chemical Vapor Deposition	56
2.7.2 Chemical bath deposition	56
2.7.3 Electrodeposition	57
2.7.4 Sol-gel technique	58
2.8 Spray pyrolysis technique (SPT)	58
2.8.1 Introduction	58
2.8.2 Principle	59
2.8.3 Scheme of pyrolysis and formation of thin films	60
2.8.3.1 Precursor solution	60
2.8.3.2 Atomization of precursor solution	60
2.8.3.3 Decomposition of precursor	60
2.9 Factors governing the formation of thin film using spray pyrolysis technique	61
2.10 Merit of spray pyrolysis technique	61
2.11 Thin Film Characterization Techniques	62
2.11.1 Thickness measurement	62
2.11.1.1 Weight difference method	62
2.11.1.2 Interference method	62
2.11.2 Structural characterization	63
2.11.2.1 X-ray diffraction (XRD)	63

2.11.2.2 Identification of phases	65
2.11.2.3 Structural Parameters	65
2.11.2.3.1 Interplanar spacing	65
2.11.2.3.2 Crystallite size (Grain size)	66
2.11.2.3.3 The texture coefficient	66
2.11.2.3.4 Microstrain	66
2.11.2.3.5 Dislocation density	66
2.11.3 Surface characterization	67
2.11.3.1 Scanning electron microscopy (SEM)	67
2.11.3.2 Energy dispersion X-Ray (EDX)	68
2.11.4 Optical characterization	69
2.11.4.1 UV-Vis-NIR Spectrophotometer	69
2.11.4.2 Absorption coefficient	70
2.11.4.3 Optical band gap energy	71
2.11.4.4 Urbach Energy	72
2.11.4.5 Optical Constants	73
2.11.5 Fourier transforms infrared spectroscopy (FTIR)	74
2.11.6 Photoluminescence (PL) Spectroscopy	75
2.11.7 Electrical Characterization	76
2.11.7.1 Conduction nature of Films	76
2.11.7.2 Linear four probe technique	77
2.11.7.3 Hall Effect measurements	79
References	81

Chapter III : Elaboration and characterizations of undoped NiO thin films

3.1 Introduction	85
3.2 Effect of solvents nature	85
3.2.1 Experimental procedure	85
3.2.2 Films preparation	85
3.2.3 Films characterization	86
3.2.4 Result and discussions	86
3.2.4.1 Structural properties	86
3.2.4.2 Optical properties	88
3.2.4.3 Electrical properties	91
3.3 Effect of Precursor Concentration	92
3.3.1 Experimental procedure	92
3.3.2 Films preparation	92
3.3.3 Films characterization	93
3.3.4 Result and discussions	93

3.3.4.1 Structural properties	93
3.3.4.2 Fourier Transform Infrared (FT-IR) Analysis	95
3.3.4.3 Optical properties	97
3.3.4.4 Electrical properties	100
3.4 Effect of sprayed solution volume	101
3.4.1 Experimental procedure	101
3.4.2 Films preparation	101
3.4.3 Films characterization	101
3.4.4 Result and discussions	102
3.4.4.1 Structural properties	102
3.4.4.2 Fourier Transform Infrared (FT-IR) analysis	104
3.4.4.3 Optical properties	105
3.4.4.4 Electrical properties	107
References	109

Chapter IV : Synthesis and characterizations of doped NiO thin films

4.1 Introduction	115
4.2 Effect of Copper doping NiO thin films	115
4.2.1 Experimental procedure	115
4.2.2 Synthesis of thin films	115
4.2.3 Thin films characterization	116
4.2.4 Result and discussions	116
4.2.4.1 Structural properties	116
4.2.4.2 Fourier Transform Infrared (FT-IR) analysis	119
4.2.4.3 Optical properties	120
4.2.4.4 Photoluminescence studies	122
4.2.4.5 Electrical properties	124
4.3 Effect of Lithium doping NiO thin films	126
4.3.1 Experimental procedure	126
4.3.2 Synthesis of thin films	126
4.3.3 Thin films characterization	126
4.3.4 Result and discussions	127
4.3.4.1 Structural properties	127
4.3.4.2 Fourier Transform Infrared (FT-IR) analysis	129
4.3.4.3 Optical properties	130
4.3.4.3 Photoluminescence studies	133
4.3.4.4 Electrical properties	135
References	137
Summary and Conclusion	142
Publication	146

List of Figures

Figure 1	Concepts of transparent displays: (a) early vision; (b) recent concepts	1
Figure I.1	Path of the conduction electrons scattering of the ions in the material according to the Drude model	11
Figure I.2	The ‘optical window’ of TCOs set by its plasma edge (p) at longer wavelengths (lower energy) and optical band gap at short wavelengths (high energy)	12
Figure I.3	representation of the electronic bands structure of a TCO material in (a) undoped and (b) doped cases where the Fermi level (E_F) is pushed up into the conduction band and makes the system conductive	13
Figure I.4	Illustration of a low-e glass	16
Figure I.5	Emerging Applications; (a) transparent electronics (b) Flexible displays	17
Figure I.6	Display market revenue evolution and forecast, adapted from Display bank	18
Figure I.7	Schematic diagram explaining the principle of photocatalysis	19
Figure I.8	The rhombohedral primitive cell of a face central cubic cell of nickel oxide	21
Figure I.9	Ni-O phase diagram	21
Figure I.10	Gibbs free energy versus temperature in nickel oxidation for the formation of NiO	22
Figure I.11	Type of defects inside crystal	23
Figure I.12	A schematic molecular orbital diagram of the NiO molecule	24
Figure I.13	A schematic of pure stoichiometric NiO crystal	25
Figure I.14	A schematic of pure non-stoichiometric NiO crystal	26
Figure I.15	Ordered arrangement of spins Ni ²⁺ ions in NiO/the O ²⁻ ions are not shown	26
Figure II.1	Different stages of thin film growth	51
Figure II.2	Schematic diagram of classifications of thin films deposition techniques	53
Figure II.3	Schematic diagram of RF sputtering system	54
Figure II.4	Schematic diagram of PLD system	55
Figure II.5	Schematic diagram of Thermal evaporation system	55
Figure II.6	Schematic diagram of Chemical bath deposition system	57
Figure II.7	Schematic diagram of Electrodeposition system	57
Figure II.8	Schematic summary of the sol-gel process	58
Figure II.9	Schematic diagram of Spray pyrolysis system	59
Figure II.10	Mechanism of thin films formation by Spray pyrolysis method	61
Figure II.11	Interference method for thickness measurement	63
Figure II.12	Schematic diagram of X-ray diffractometer	64
Figure II.13	Diffraction in crystals	64
Figure II.14	Schematic diagram of SEM	68
Figure II.15	Schematic diagram of Energy dispersion X-Ray (EDX)	69
Figure II.16	Schematic diagram of UV-Vis-NIR Spectrophotometer	70
Figure II.17	E-K diagram showing (a) direct band and (b) indirect band transition	71
Figure II.18	$(ah\nu)^2$ vs $(h\nu)$ plot for determining direct energy band gap	72
Figure II.19	Basic schematic of the spread of density of states in the band gap energy	73
Figure II.20	Schematic diagram of FTIR Spectrophotometer	75
Figure II.21	Energy level diagram	76
Figure II.22	Hot probe technique for measuring Conduction nature of thin Film	77
Figure II.23	Schematic of four point probe configuration	78
Figure II.24	Schematic diagram of Hall Effect measurements	79
Figure III.1	XRD patterns of NiO films using different solvents	87
Figure III.2	Variation of crystallite size and mean strain of NiO thin films using different solvents	88
Figure III.3	Transmittance spectra of NiO thin films using different solvents	89
Figure III.4	Estimation of band gap energy (E_g) from Tauc’s relation of NiO thin films using different	90

	solvents	
Figure III.5	Estimation of Urbach energy (E_u) of NiO thin films using different solvents	90
Figure III.6	Variation of band gap energy (E_g) and Urbach energy (E_u) of NiO thin films using different solvents	91
Figure III.7	Variation of Conductivity (σ) and film thickness (t) of NiO thin films using different solvents	92
Figure III.8	X-ray patterns of NiO thin films prepared at 500°C with different of precursor concentration	94
Figure III.9	Variations of grain size and band gap (E_g) of NiO thin films as function of precursor concentration prepared at 500°C	95
Figure III.10	FT-IR spectra of NiO thin films prepared at 500°C with different precursor concentration, (d, e) samples prepared with 0.05 and 0.1 M, (a, b, c) with 0.015, 0.03, and 0.04M	96
Figure III.11	Spectral transmittance plots of NiO thin films prepared at at 500°C with different of precursor concentration	98
Figure III.12	Band gap (E_g) estimation from Tauc's relation of NiO thin films prepared at 500°C with different of precursor concentration	99
Figure III.13	Urbach energy (E_u) estimation of NiO thin films prepared at 500°C with different of precursor concentration	100
Figure III.14	Variations of conductivity and thickness (t) of NiO thin films as function of precursor concentration prepared at 500°C	100
Figure III.15	X-ray patterns of NiO thin films prepared at 500°C with different sprayed volume	102
Figure III.16	Variation of grain size of NiO thin films prepared at 500°C with different sprayed volume	103
Figure III.17	FT-IR spectra of NiO thin films prepared at 500°C with sprayed volume (a) from 5ml to 15ml, (b) from 20ml to 30ml	104
Figure III.18	Spectral transmittance plots of NiO thin films prepared at 500°C with different sprayed volume	105
Figure III.19	Variation of NiO thin films thickness prepared at 500°C with different sprayed volume	106
Figure III.20	Estimation of band gap energy (E_g) from Tauc's relation of NiO thin films prepared at 500°C with different sprayed volume	106
Figure III.21	Estimation of Urbach energy (E_u) of NiO thin films prepared at 500°C with different sprayed volume	107
Figure III.22	Variation of band gap energy (E_g) and Urbach energy (E_u) of NiO thin films prepared at 500°C with different sprayed volume	107
Figure III.23	Variations of Resistivity and grain size (G) of NiO thin films as prepared at 500°C with different sprayed volume	108
Figure IV.1	X-ray patterns of undoped and Cu-doped NiO thin films variation of diffraction intensity in the range 2θ (36.8°–37.9°) corresponding to the (111) peak for undoped and Cu-doped NiO thin films	117
Figure IV.2	Variation of crystallite size and mean strain size of NiO thin films as a function to the copper concentration	119
Figure IV.3	FT-IR spectra of undoped and Cu-doped NiO thin films	119
Figure IV.4	Transmittance spectra of undoped and Cu-doped NiO thin films	120
Figure IV.5	Estimation of band gap energy (E_g) from Tauc's relation of undoped and Cu-doped NiO thin films	121
Figure IV.6	Photoluminescence spectra of undoped and Cu-doped NiO thin films	122
Figure IV.7	Deconvoluted photoluminescence spectra of undoped and Cu-doped NiO thin films	123
Figure IV.8	Schematic energy level diagram of undoped and Cu-doped NiO thin films	124
Figure IV.9	Variation of the conductivity of NiO thin films as a function to the copper concentration	125
Figure IV.10	X-ray patterns of undoped and Li-doped NiO thin films variation of diffraction intensity in the range 2θ (37–38) corresponding to the (111) peak for undoped and Li-doped NiO thin films	127
Figure IV.11	Variation of crystallite size and mean strain size of NiO thin films as a function to the Li concentration	129
Figure IV.12	FT-IR spectra of undoped and Li-doped NiO thin films	130
Figure IV.13	Transmittance spectra of undoped and Li-doped NiO thin films	131
Figure IV.14	Estimation of band gap energy (E_g) from Tauc's relation of undoped and Cu-doped NiO thin	132

	films	
Figure IV.15	Estimation of Urbach energy (E_u) of undoped and Li-doped NiO thin films	133
Figure IV.16	Photoluminescence spectra of undoped and Li-doped NiO thin films	134
Figure IV.17	Deconvoluted photoluminescence spectra of undoped and Li-doped NiO thin films	135
Figure IV.18	Schematic energy level diagram of undoped and Li-doped NiO thin films	135
Figure IV.19	Variation of the resistivity of NiO thin films as a function to the Li concentration	136

List of Tables

Table I.1	Minimum required properties of TCOs	15
Table I.2	Standard thermodynamic properties of nickel and NiO	22
Table III.1	Values of Bragg angle (2θ), lattice constants (a), crystallite size (D) and mean strain (ε) for the (111) plane of NiO thin films using different solvents.	87
Table III.2	Values of thickness (t), optical band gap energy (E_g), Urbach energy (E_u) and conductivity (σ) of NiO thin films using different solvents	89
Table III.3	Values of Bragg angle 2θ , lattice constants a , full width at half maximum β , grain size G , mean strain ε and dislocation density δ for the (111) plane of NiO thin films prepared at 500°C with different of precursor concentration	94
Table III.4	The assignments of the most important bands in the FT-IR spectra of NiO thin films sprayed at 500°C with different of precursor concentration	97
Table III.5	Values of thickness t , average transmittance, optical band gap energy E_g , and Urbach energy E_u of NiO thin films prepared at 500°C with different of precursor concentration	98
Table III.6	Values of Bragg angle 2θ , lattice constants a , grain size G , mean strain ε and dislocation density δ for the (111) plane of NiO thin films prepared at 500°C with different sprayed volume	103
Table III.7	Values of thickness t , band gap energy E_g and Urbach energy E_u of NiO thin films prepared at 500°C with different sprayed volume	105
Table IV.1	Values of Bragg angle 2θ , lattice constants a , crystallite size D , mean strain ε and dislocation density δ for the (111) plane of NiO thin films as a function to the copper concentration	118
Table IV.2	Values of thickness t , optical band gap energy E_g , Urbach energy E_u and Conductivity σ of NiO thin films as a function to the copper concentration	121
Table IV.3	Values of Bragg angle 2θ , lattice constants a , crystallite size D and mean strain ε for the (111) plane of NiO thin films as a function to the Li concentration	128
Table IV.4	Values of thickness t , optical band gap energy E_g , Urbach energy E_u and Resistivity ρ of NiO thin films as a function to the Li concentration	132

General Introduction

General introduction

The fast-growing and more development of the worldwide market of energy (photovoltaics, architectural and window glasses) and information (displays) technologies will be only sustainable if either, low-cost materials, environmentally friendly and low-temperature processing technologies will be used [1]. Transparent electronics is showing as one of the most advantageous technologies for future electronic products, away from the traditional silicon technology. The fact that circuits founded on conventional semiconductors as silicon and conductors as copper can be turned transparent by using different materials, the so-called transparent semiconducting and conducting oxides (TSOs and TCOs, respectively), is of great importance and enable to defining innovative and high added value application fields. The viability of this technology depends to a large extent on the performance, reliability, and cost of the transparent electronic [2]. The most immediate event of transparent electronics would be the realization of a transparent display, something that has been envisaged already for a long time, at least from the 1930s when H.G. Wells imagined it in his science fiction novel “The shape of things to come” (Fig.1a). Nowadays, with the coming of TSOs and TCOs, which besides transparency also allow for low temperature, low processing costs and high performance, transparent displays start becoming truly conceivable and soon the futuristic concepts shown in Fig.1b will certainly be real [2].



Figure 1: Concepts of transparent displays: (a) early vision; (b) recent concepts [1]

Recent years, research in TSOs thin films has assumed significance due to high stability, important optical characteristics, and excellent electrical properties. TCOs are basically metal oxide semiconductors grouped as either n-type or p-type. Coatings of n-type semiconductors, such as indium tin oxide, zinc oxide etc., are required in many technological applications such as transparent electronics and nanodevices [3-5].

Among various n-type semiconductors, ZnO, a direct band gap (3.37 eV) material, has been extensively used in the optoelectronic devices during past decade. Furthermore, in recent years, a great interest has been devoted to thin films of a p-type semiconductor due to their important applications in optoelectronic devices such as changeable reflectance mirror and elements for information display light shutter. However, not much study has been achieved on p-type wide band gap energy semiconductors. Such p-type semiconductors could allow the use of new classes of organic compounds. Regrettably, relatively few metal oxides tend to be p-type [6].

Recently, widely attention has been paid to the Nickel oxide (NiO) films and devices because of its promising properties such as UV transparent conductivity, wide band gap semiconductor with the absorption edge in the near UV-visible region, natural p-type semiconductor, which has been useful in the fields of UV detectors, gas sensors and heterojunction LEDs and LDs [7-11]. Moreover, the attractiveness of NiO as a p-type conducting material with exceptional chemical or/and physical properties such as; has low cost and good chemical stability compared to the high-quality p-type ZnO and GaN materials, which are difficult to realize because of the high resistance and less stability of this material [12]. The properties of the NiO thin films highly depend on the process of formation. Numerous techniques have been exercised for NiO thin film preparation with emphasis on reliability and cost. These methods can be classified as physical and chemical processes. According to the literature, NiO films can be produced with co-precipitation method [13], sol-gel techniques [14] vacuum evaporation [15], atomic layer deposition [16], pulsed laser deposition [17], and spray pyrolysis method (SPM) [18].

SPM is a very significant method to fabricate the TCO films because it is a relatively simple component, using atmospheric pressure deposition process, and it is an inexpensive technique for wide area coating. It has since been used in the glass industry and in solar cell production to deposit electrically conducting electrodes. Through this technique, powders, dense, porous oxide films, and ceramic coatings can be prepared. It represents a very easy and relatively cost-effective method, especially regarding equipment cost [19, 20]. Materials obtained by SPM find an enormous range of applications in the solar absorber, optoelectronic devices, gas sensors ...etc [21-23].

The main objective of the present study is to prepare good quality nano-structured nickel oxide (NiO) thin films using SPM. Films grown with this method are found to exhibit enhanced performance when compared to films obtained by other conventional deposition

techniques. A wide variety of thin films has been deposited with SPM. Also, various devices such as solar cells, sensors, and solid oxide fuel cells have been prepared by using these films [24].

Mainly involved in SPM the growth of films can easily be controlled by one or more deposition parameters such as spray rate, substrate surface temperature, atomization of the precursor solution, doping concentration, nozzle distance and carrier gas flow-rate. We focused in this study on the effect of preparative parameters such as solvents nature, the concentration of precursor and volume of the sprayed solution on structural, optical and electrical properties of NiO thin films in order to optimize the deposition conditions. Furthermore to enhance several physical properties of NiO thin films such as transparency, conductivity, defect structure. Incorporation of doping using metallic elements is an effective way to change physical properties of NiO thin films. In the present investigation, the effects of copper (Cu) and lithium (Li) doping concentration on, structural, compositional, optical, photoluminescence and electrical properties of NiO thin films prepared by spray pyrolysis method will be studied.

The thesis is composed of four chapters, organized as follows; starting with the **general introduction, the chapter 1** will give an overview of the technical and theoretical background of the transparent conducting oxides (TCOs), importance, basic properties and applications areas of TCOs. This chapter also gives the state of the art of nickel oxide (NiO) thin films, its different chemical and physical properties and applications of the current research status. Furthermore, review of works done by many researchers is selected field on undoped and doped NiO thin films have been carried out in this chapter.

Chapter 2 describes diverse synthesis techniques employed to prepare thin films and principles of the characterization technique utilized to characterize and study the various physical properties of the thin films.

Chapter 3 focuses on the results and discussion of the investigation of the influences of deposition parameters such as solvent nature, precursor solution concentration and sprayed solution volume of undoped NiO thin films prepared by spray pyrolysis method on the structural, optical, compositional and electrical properties.

Chapter 4 describes the results and discussion of study the doping effects of copper and lithium of NiO thin films prepared by spray pyrolysis method on the structural, optical, compositional, photoluminescence and electrical properties.

Finally, **the summary and conclusion** present the synthesis of all results obtained, concluding remarks and suggestions for future works.

References

- [1] N. M. Pinto Neves, Al-doped ZnO ceramic sputtering targets based on nanocrystalline powders produced by emulsion detonation synthesis deposition and application as a transparent conductive oxide material, PhD thesis, Nova de Lisboa university, 2015.
- [2] P.M. Cândido Barquinha, Transparent Oxide Thin-Film Transistors: production, characterization, PhD thesis, Nova de Lisboa University, 2010.
- [3] R. Sharma, A.D. Acharya, S.B. Shrivastava, M. M. Patidar, M. Gangrade, T. Shripathi, V. Ganesan, Studies on the structure optical and electrical properties of Zn-doped NiO thin films grown by spray pyrolysis, *Optik*, 127 11 (2016) 4661-4668.
- [4] J. F. Wager, Transparent electronics, *Science*, 300 (2003) 1245-1246.
- [5] H. Hosono, Recent progress in transparent oxide semiconductors: Materials and device application, *Thin Solid Films*, 515 (2007) 6000-6014.
- [6] R. Romero, F. Martin, J.R. Ramos-Barrado, D. Leinen, Synthesis and characterization of nanostructured nickel oxide thin films prepared with chemical spray pyrolysis, *Thin Solid Films*, 518 (2010)4499-4502.
- [7] Y. Zhao, H. Wang, X. Gong, J. Wang, H. Li, M. Tang, X. Li, Effect of lithium-ion doping concentration on structural and optical properties of NiO films fabricated by magnetron sputtering, *Vacuum*, 137(2017) 56-59.
- [8] B.A. Reguing, A. Khalil, L. Cattin, M. Morsli, J.C. Bernede, Properties of NiO thin films deposited by intermittent spray pyrolysis process, *Appl. Surf. Sci.*, 253(2007) 4330-4334.
- [9] R. Deng, B. Yao, Y.F. Li, Y. Xu, J.C. Li, B.H. Li, Z.Z. Zhang, L.G. Zhang, H.F. Zhao, D.Z. Shen, Ultraviolet electroluminescence from n-ZnO/p-NiO hetero-junction light-emitting diode, *Journal of Luminescence*, 134 (2013) 240-243.
- [10] Z.F. Shi, Y.T. Zhang, X.J. Cui, S.W. Zhuang, B. Wu, J.Y. Jiang, X.W. Cui, X. Dong, B.L. Zhang, G.T. Du, Near infrared electroluminescence from n-InN/p-NiO hetero-junction light-emitting diode, *Cryst. Eng. Comm.*, 17 (2015) 40.
- [11] H. Wang, Y. Zhao, C. Wu, X. Dong, B.L. Zhang, G.G. Wu, Y. Ma, G.T. Du, Ultraviolet electroluminescence from n-ZnO/NiO/p-GaN light-emitting diode fabricated by MOCVD, *Journal of Luminescence* 158 (2015) 6-10.
- [12] Y. Zhao, H. Wang, G.G. Wu, Q. Jing, F.B. Gao, W.C. Li, B.L. Zhang, G.T. Du, Influence of InN epilayers on structural, electrical and optical properties of NiO films grown by magnetron sputtering, *Vacuum*, 124 (2016) 72e75.
- [13] J.F. Wang, J.N. Cai, Y.H. Lin, C.W. Nan, Room-temperature ferromagnetism observed in Fe-doped NiO, *Appl. Phys. Lett.*, 87 (2005) 202501.
- [14] D.S. Dalavi, R.S. Devan, R. S. Patil, Y-R. Ma, P. S. Patil, Electrochromic performance of sol-gel deposited NiO thin film, *Materials Letters*, 90 (2013) 60-63.
- [15] B. Sasi, K.G. Gopchandran, P.K. Manoj, P. Koshy, P. P. Rao, V.K. Vaidyan, Preparation of transparent and semiconducting NiO films, *Vacuum*, 68 (2003) 149-154.

- [16] E. Dashjav, M. Lipińska-Chwałek, D. Grüner, G. Mauer, M. Luysberg, F. Tietz, Atomic layer deposition and high-resolution electron microscopy characterization of nickel nanoparticles for catalyst applications, *Surface and Coatings Technology*, 307(2016) 428-435.
- [17] S.D. Singh, Arijeet Das, R.S. Ajimsha, M.N. Singh, A. Upadhyay, R. Kamparath, C. Mukherjee, P. Misra, S.K. Rai, A.K. Sinha, T. Ganguli, Studies on structural and optical properties of pulsed laser deposited NiO thin films under varying deposition parameters, *Materials Science in Semiconductor Processing*, 66(2017) 186-190.
- [18] R.S. Kate, S.A. Khalate, R.J. Deokate, Electrochemical properties of spray deposited nickel oxide (NiO) thin films for energy storage systems, *Journal of Analytical and Applied Pyrolysis*, 125(2017) 289-295.
- [19] V. Khanaa, K. Mohanta, synthesis and structural characterization of SnO₂ thin films prepared by spray pyrolysis technique, *International Journal of Advanced Research*, 1(2013) 666-669.
- [20] P. Dainius, Thin film deposition by spray pyrolysis and the application in solid oxide fuel cells, Swiss Federal institute of technology Zurich, 2003.
- [21] C. Mrabet, M. Ben Amor, A. Boukhachem, M. Amlouk, T. Manoubi, Physical properties of La-doped NiO sprayed thin films for optoelectronic and sensor applications, *Ceramics International*, 42 (2016) 5963-5978.
- [22] E. Ienei, L. Isac, C. Cazan, A. Duta, Characterization of Al/Al₂O₃/NiO_x solar absorber obtained by spray pyrolysis, *Solid State Sciences*, 12(2010) 1894-1897.
- [23] I. G. Wilches, J.C. Alonso, Hydrogen sensors fabricated with sprayed NiO, NiO:Li and NiO:Li, Pt thin films, *International Journal of Hydrogen Energy*, 38(2013) 4213-4219.
- [24] P. Kumar, Magnetism and magnetotransport in half and over doped manganites impact of substrate induced strain and Polycrystalline Disorder, PhD thesis, Jaypee Institute of Information Technology, 2013.

Chapter I

Literature Review and Technical Background

Transparent electronics have received more attention in last decade and come to be an important branch in material science. The development in this branch necessitates of understanding the fundamental properties of transparent conducting oxides (TCOs). This chapter is classified into two sections. Section I gives an introductory background to the basic principles of transparent conducting oxides (TCOs), a brief discussion of the description of the important properties of TCOs, followed by their current and emerging applications. Section II gives the fundamentals properties of Nickel Oxide (NiO) material, with mention of its most prominent applications to technology and research. also, a review of works done by many researchers are selected field on undoped and doped nickel oxide thin films prepared by different deposition methods have been carried out in this section.

1.1 Introduction to transparent conducting oxides

Semiconductor physics has developed broadly in the field of research and industry in the previous few decades. One of the important fields that represent a class of materials is a transparent conductive oxide (TCO). TCOs are materials combining high electrical conductivity ($10^3 \sim 10^4 \text{ S/cm}^{-1}$) and high optical transparency (above 80%) in the visible spectrum [1- 4]. They are different from the well-known conductors such as metals, semimetals or carbon materials, or transparent materials such as oxide glasses. The metals are excellent electric conductors owing to the enormous concentration of delocalized mobile electrons, but they strongly absorb visible light and hence are not transparent. Besides, the oxide glasses are highly transparent and their wide band-gap energy (over 3 eV), but the absence of enough free charge carriers generally determine their low electrical conduction behavior. The combination of the seemingly contradictory properties, namely high electrical conductivity and the high optical transparency, is however featured by the TCO materials [5- 8].

1.2 History - Past, present and future of TCOs

Over the centuries, each material was associated with intrinsic properties. When characterized as thin films, for instance, metals are normally described as having a high electrical conductivity and opacity. In turn, ceramics are generally seen as electrical insulating materials and optically transparent for the reason to their usually large band gap ($E_g \geq 3 \text{ eV}$). Thus, the discovery of simultaneously conductive and transparent materials has changed the world. The first material where this combination of properties was observed dates from 1907, when Badeker produced the first TCO, the cadmium oxide (CdO) [9].

However, it took about 40 years until the development of new TCOs with superior properties, especially the ones based on SnO_2 , In_2O_3 and ZnO due to the improvements in production and characterization techniques. It was during the Second World War that brought the first applications of these materials. By that time, SnO_2 was used as defroster at high altitudes in the warplanes, thereby enabling the aircraft pilots to maintain visibility [7, 10]. Since then, SnO_2 which was produced using spray pyrolysis, used in several applications such as window defroster or transparent electrical contacts replacing metals commonly used in these applications such as gold or silver. However, despite its low electrical resistivity ($\sim 10^{-5} \Omega\cdot\text{cm}$), these films had an optical transmittance below 80 %, which was a limitation, especially when used as transparent electrical contacts. Nevertheless, this limitation was suppressed in 1956 with the appearance of the $\text{SnO}_2\text{-Sb}_2\text{O}_3$ TCO with a transmittance above 85 % in the visible region and an acceptable electrical resistivity of about $10^{-2} \Omega\cdot\text{cm}$, turning this kind of materials as an alternative to metal thin films [10]. Moreover, $\text{SnO}_2\text{-Sb}_2\text{O}_3$ thin films also presented high chemical stability, mechanical strength and good compatibility with different substrates [4, 10].

During the following decades, the severe increase in oil prices led to the search for alternative energy sources, in particular, photovoltaics, which indirectly resulted in a strong and ongoing progress in TCOs development [11]. Besides polycrystalline TCOs, the 90s was marked by the creation of a novel class of amorphous oxides with properties comparable to those of polycrystalline materials.

In 1990, Belligham et al. in an early work [12] presented amorphous In_2O_3 with electrical and optical properties comparable to those of widely studied polycrystalline In_2O_3 . In 1996, Hosono et al. boosted singularly the improvement of this class of oxides with the presentation of a new theory for the formation of amorphous oxides [13]. Also, the first p-type TCOs were developed in this decade using NiO [14, 15].

Nowadays, TCOs are used in a broad range of applications, where flat panel displays and thin film solar cells are the larger markets for TCOs. Both have costs constraints as the global prices are decreasing fast. Thus, the searches for low-priced and abundant material become challenging and several alternatives appeared, including conductive polymers, carbon nanotubes, or graphene [16, 17]. Recently, TCOs have generated a new area of electronics acknowledged as transparent electronics.

The transparent metal oxides besides a passive character (TCOs) can perform also as an active component. Used as semiconductor material (called by TSO-Transparent

Semiconductor Oxide) in thin film transistors (TFTs), these materials are in direct competition with traditional silicon-based technology [18, 19].

1.3 Classification of TCOs

On the basis of majority charge carriers, all TCOs can be classified into two groups; n-type and p-type.

1.3.1 N-type TCOs

An n-type TCO is one in which the majority charge carriers are the negatively charged electrons. The majority of the TCOs are n-type and consequently are most commonly found in practical applications [20]. The conduction band for these materials is formed from metal cation electron states, with the precise energy state depending on the cation.

The valence band is normally constructed of oxygen 2p states [22, 23]. Because oxygen has high electro negativity, and because the energy level of the 2p state is significantly lower than that of most outer sub-shell cation states, any electron- holes are trapped or localized beside individual oxygen atoms [21-24]. This means that for most oxide semiconductors, holes have a highly effective mass and so low mobility [23, 4]. Because the metal cations whose electron states typically form the conduction band tends to be much less electronegative, electrons usually have a much lower effective mass and so higher mobility. This demonstrates why most metal oxides show n-type behavior [23, 25].

1.3.2 P-type TCOs

In p-type TCOs the majority charge carriers are positively charged holes [20, 26]. The p-type TCOs have generally less conductivity than that reported for n-type TCOs. The large electro negativity of oxygen could be producing a strong localization of the valence band edge of oxides thereby producing a deep trap where positive holes are localized [27]. These holes cannot migrate even under an applied field. Thus efforts should be made to modulate or modify the energy band structure to reduce the localization of the valence band edge so as to increase the mobility of the holes, for example, Cu_2O and Ag_2O show p-type conductivity. However, their low band gap ($\sim 2\text{eV}$) makes it impossible to use them as transparent conductors. Analyzing the structure of these compounds shows linear coordination of two oxygen ions to Cu^+ ion this could be an indication of the fact that the $3d^{10}$ electrons of Cu^+ have comparable energy with $\text{O } 2p^6$ electrons. This could be reducing the localization effects of the traps produced at the valence band edge. But the three-dimensional interaction of Cu^+ ions should be increasing the band edge effectively reducing the band gap. Thus if the Cu^+

interactions could be reduced while the linear coordination with two oxygen atoms is retained in any crystal structure, this would produce p-type transparent conductors [28].

1.4 Basic properties of transparent conducting oxides

1.4.1 Electrical Conductivity

Numerous researchers have been done on the electrical properties of TCO films to comprehend the conduction phenomena involved [28-31]. The mechanism of conductivity in TCOs can be acknowledged with the help of classical (Drude like) explanation of charge transport in metals. In 1900, a model was proposed by Paul Drude to give details about the transport properties of electrons in metals, commonly known as Drude model [32].

He assumed that matter consists of light negatively charged electrons which are mobile, and heavy, static, positively charged ions which are immobile. The only interactions are electron-core collisions, which have effect in a very little time span τ . (Long-range interaction between the electrons and the ions or between the electrons were neglected) [37].

Figure I.1 shows a pathway of the conduction electrons scattering off the ions in the material, according to the Drude model. Electrons are affected to attain thermal stability through collisions, and the probability of an electron suffering a collision in a short time dt is dt/τ , where $1/\tau$ is the scattering rate. The equation of motion for an electron moving in the crystal is interpreted by the second law of Newton, and if τ is the average time between collisions, the average drift speed is [37]:

$$v_d = \frac{eE\tau}{m^*} = \mu E \quad (\text{I. 1})$$

where E is the electric field, m^* is the electron effective mass, and e is the electric charge. The conductivity of the material as a function of the number of charge carrier's n is given by:

$$\sigma = \frac{ne^2\tau}{m^*} = n\mu e \quad (\text{I. 2})$$

The above relation displays the dependence of material conductivity with the number of charge carriers n , their effective mass m^* , and the relaxation time τ . The high conductivity in TCO films outcome essentially from non-stoichiometric. The conduction electrons in TCO films are set up from donor sites related to oxygen vacancies or excess metal ions [33].

The carrier mobility is the main crucial factors affecting the conductivity in TCO films. In the polycrystalline film, the carrier mobility is associated with scattering phenomena in the lattice imperfections. The different scattering process concerned in thin films are; acoustic deformation potential scattering, piezoelectric scattering, optical phonon scattering,

neutral impurity scattering, ionized impurity scattering, electron-electron scattering and grain boundary scattering [34-36].

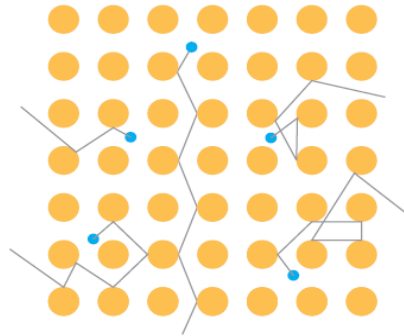


Figure I.1: Path of the conduction electrons scattering of the ions in the material according to the Drude model

1.4.2 Optical properties

The optical properties of TCO thin films provide powerful tools to known energy band structure, impurity levels, localized defects, lattice vibrations etc. The optical properties of TCO films, and therefore the optical constants, strongly related to the deposition parameters, microstructure, level of impurities and growth technique. Brief literature has been achieved by various workers in this area [38-40].

The typical spectral dependence of TCOs is represented in Figure I.2. The transmission window is limited between two regions where no light is transmitted due to different phenomena. At short wavelengths ($\lambda < \lambda_{\text{gap}}$) the absorption as a result of the fundamental band gap dominates. The photon energy in this near-and deep-UV part of the spectrum is high enough to equal the band gap energy (3 - 4 eV). This energy is absorbed in band to band transitions, and no light is transmitted because of this quantum phenomenon [41].

From wavelength varied in the range 400 -1000 nm, the photon energy is too low and the TCO film is transparent. If the TCO is adequately flat, an interference structure will be observed and related to the thickness of the film and refractive index. The absorption in this zone is small.

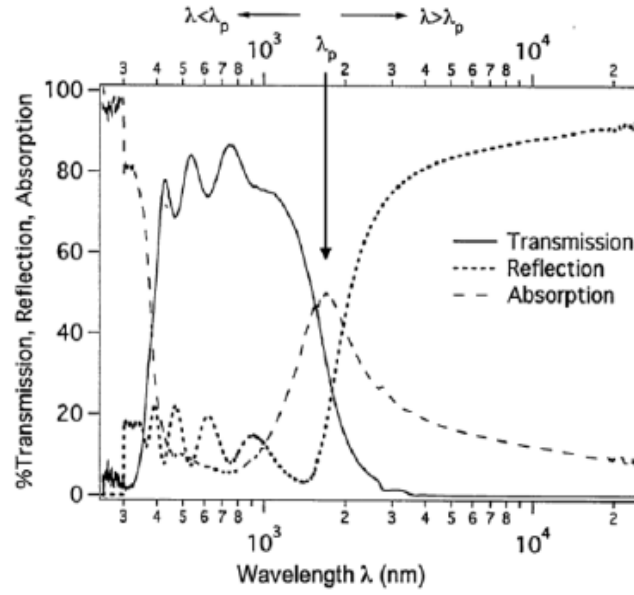


Figure I.2 The ‘optical window’ of TCOs set by its plasma edge (p) at longer wavelengths (lower energy) and optical band gap at short wavelengths (high energy). [41]

In the near of IR zone, the absorption and reflection become important for the reason that the free carriers in the CB (or VB for p-type TCOs). This behavior can be interpreted using the classical Drude theory: the free carriers oscillate with an applied field, like the free electrons in metals (plasma oscillations). The plasmon frequency, ω_p given by [42]:

$$\omega_p = \frac{(ne^2)^{1/2}}{(m^* \epsilon_0)^{1/2}} \quad (\text{I. 3})$$

or

$$\lambda_p = 2\pi c \frac{(m^* \epsilon_0)^{1/2}}{(ne^2)^{1/2}} \quad (\text{I. 4})$$

where λ_p is the plasma wavelength, n is the free carrier density, m^* is the electron effective mass, c is the speed of light in vacuum and ϵ_0 is the permittivity of free space. λ_p corresponds to the front rise of the reflectivity in the IR and accounts for a metallic nature of the TCO; it corresponds to intra-band absorption in the (CB) energy of the electrode material, when resonance occurs between the incident energy and the plasma oscillation of the (quasi) free electrons in the (CB) energy [43]. At this frequency the dielectric-like visible transmittance equals the metallic-like IR reflectance ($T=R$). Thus the IR reflectivity of the material as it may be tuned, which is Important for heat reflecting or low emissive window applications [44, 45].

1.4.3 Defects and impurities in TCO materials

Doping with the presence of native point defects alters the quantity of charge carriers (electrons for 'n-type' and holes for 'p-type') in semiconductors and can highly affect their conductivity. Figure I.3 shows the representation of the band energy structure of a TCO material in both undoped and doping cases. In the doped case, the Fermi level (E_F) is pushed up into the CB energy and makes the system conductive. The knowledge of defects and impurities is an important research area in semiconductor physics. They are used to adapt the electronic structure and optoelectronic properties of materials [37, 46].

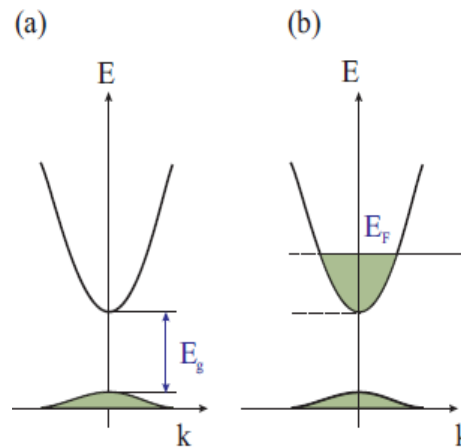


Figure I.3: representation of the electronic bands structure of a TCO material in (a) undoped and (b) doped cases where the Fermi level (E_F) is pushed up into the conduction band and makes the system conductive [37].

1.5 Intrinsic and extrinsic doping of TCOs

Stoichiometric metal oxides include gap energy greater than 3 eV and are therefore practically insulators at room temperature. There is two type of doping process to obtain a higher charge carrier concentration in TCOs. In this case, the material becomes n-type. These mechanisms are named intrinsic doping and extrinsic doping [47].

1.5.1 Intrinsic doping

Intrinsic doping is becoming to defects in the lattice structure, away from stoichiometry. This suggests to a small oxygen deficiency and vacancies in those materials. These vacancies provide an increase to shallow donor states under the (CB) energy and perform as an n-type impurity band. It has been assumed that transparent conductivity is correlated to the existence of shallow donor levels near the CB energy, formed by a large concentration of oxygen vacancies. Having a shallow donor level means that these additional

energy levels are not more than $3k_bT$ (0.075 eV at room temperature) away from the lowest conduction band edge, where k_b is the Boltzmann constant [48-50].

1.5.2 Extrinsic doping

By changing the original bulk metal ions (cations) and bulk oxygen ions (anions) with ions having respectively a higher and lower valence, the carrier concentration can be increased further. This increase leads to shifting in the Fermi level within the conduction band. The incorporation of extrinsic defects (aliovalent ions) into the TiO₂ lattice, for example, leads to the creation of donors and acceptors when their valency is higher and lower than that of host lattice ions [41].

1.6 Figure of Merit for TCOs

A figure of merit (FOM) is parameter considered to compare different transparent conductive oxide electrode technologies. This parameter is the proportion of the sheet resistance to the intrinsic transparency of a transparent conductive electrode. The (FOM) is based on the Lambert-Beer law of a thin metallic film. The figure of merit was developed by Iles and Soclof given by [51, 52]:

$$FOM = -\{R_s \ln(T + R)\}^{-1} = \frac{\sigma}{\alpha} \quad (\text{I. 5})$$

where R_s is the sheet resistance, T the total visible transmission, and R the total visible reflectance. By this definition, a lower value of the figure of merit indicates films of better quality.

1.7 Criteria for choosing TCOs

For each application, the most suitable TCO is the one that shows good electrical conductivity along with good optical transparency. The physical, chemical and thermal durability, plasma wavelength, thickness, deposition temperature, toxicity, and cost are other factors that may also influence the choice of transparent conducting material for any particular application, as shown from Table I.1 [7].

The existing TCO materials have limitations in one way or the other. For example, the limited use of ITO in flexible electronics is caused by the fragility of ITO thin films. Least development of the “transparent electronics” because of the unavailability of efficient p-type TCO materials High transparency (>85%) combined with useful electrical conductivity

($>10^3 \text{ S.cm}^{-1}$) is achieved by selecting a broadband gap oxide through the introduction of suitable dopants [53-56].

Parameters	Transparent conductive Materials
Band gap	$>3.1 \text{ eV}$ (380nm)
Transparency at 550nm	$>90\%$ (for n-type) and $>85\%$ (for p-type)
Resistivity	$10^{-4} \Omega \text{ cm}$ (for n-type) and $10^{-3} \Omega \text{ cm}$ (for p-type)
Carrier Concentration	$>10^{20} \text{ cm}^{-3}$ (for n-type) and $>10^{18} \text{ cm}^{-3}$ (for p-type)
Mobility	$>40 \text{ cm}^2 (\text{V s})^{-1}$ (for n-type) and $>20 (\text{V s})^{-1}$ (for p-type)
Sheet resistance	$\leq 10 \text{ k}\Omega/\text{square}$ (for 20nm thickness)

Table I.1: Minimum required properties of TCOs [56]

1.8 Application of TCOs

TCOs are a technologically important type of materials that merge electrical conductivity and optical transparency together. TCOs are necessary for many photovoltaic and optoelectronic applications. Some of these applications are briefly depicted in the following.

1.8.1 TCO Electrodes for Solar Cell Applications

TCO materials play an integral part of the photovoltaic industry as they serve as the transparent electrode for solar cells such as amorphous silicon solar cells, dye-sensitized solar cells (DSSCs) and organic based photovoltaic devices [57-60]. TCO materials are most useful in that they are simply fabricated on a large scale via online processes. There are certain requirements however when choosing a TCO to serve as the electrode for a photovoltaic device. Matching photovoltaic performance to the TCO is vital and it should be well-known that:

- as the TCO layer thickness increases the current of short circuit decreases;
- the charge carrier density of the TCO decreases the current of the short circuit in the PV device;
- The band gap matching of the TCO with the solar spectrum can result in high exchange efficiencies.

In addition to the requirements mentioned above the TCO layer must have high durability, high adhesion and show resilience to high processing temperatures often required for thin film solar cell manufacturing [61].

Another important criterion for TCOs to serve as electrodes in PV devices is that the refractive index of the TCO material has to be chosen such that reflective losses of incident

light are minimized and light trapping using scattering centers at the film interface is maximized [62].

1.8.2 Light and heat control

By quantity, the most important application of TCOs is fluorine-doped SnO₂ (FTO) glass coatings, which are usually applied by a chemical vapor deposition (CVD) process during the float-glass production [4, 7, 63]. These so-called low emittance (“low-e”) glasses are transparent infrared reflectors [64] and allow solar control and energy saving heat management for buildings as well as for transport vehicles. Figure I.4: Illustration of low-e glass windows with tin oxide coatings are efficient in preventing radiative heat loss due to tin oxide’s low emissivity of about 0.16 [65]. The plasma wavelength on the one part and the band gap absorption of the TCO on the further part limit the transparent frequency range of the material, which can be adapted with choice of the TCO and its doping concentration. This enables the material to reflect IR-light in order to keep the building's interior cool in summer. In winter it minimizes heat losses through windows. This basic technology has been recognized early and currently not a very active field of research. In addition, TCOs are an essential part of other and new functional window designs like e.g. electrochromic windows [66- 69]. Here, the idea is to change the absorption characteristics of a window within a few minutes or seconds by applying a voltage [70].

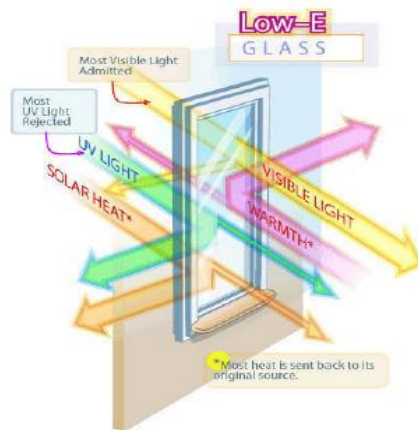


Figure I.4: Illustration of a low-e glass [70]

1.8.3 Transparent electronics

Transparent electronics is a high profile and very advanced topic for an immense range of device applications, with transparent semiconducting materials being the key factor for the improvement in this area. Passive uses of TCOs can be combined with oxide-based transparent thin film transistors (TFTs) to fabricate an extensive range of new and disruptive

technology: transparent electronics. If fabricated at low temperatures, these transparent devices can be even made on a plastic substrate for the fabrication of flexible electronics. Figure I.5 illustrates some of the envisioned applications of TSOs [71].

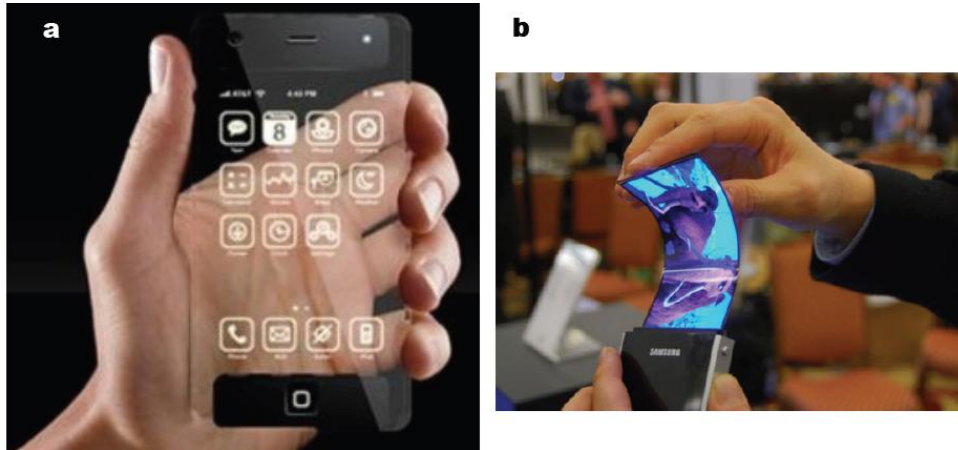


Figure I.5: Emerging Applications; (a) transparent electronics (b) Flexible displays [71]

According to the most novel display market forecast from the market research firm Display bank, transparent display technologies will dominate the market by 2030 with a projected market around US\$150 billion [72], as shown in Figure I.6. Beginning in 2010, display companies like Samsung Electronics, LG Electronics, and Sharp Electronics, among others, have demonstrated oxide-based displays with enhanced performance when compared with conventional silicon-based ones [73,74]. The key parameter for improved display performance has been the replacement of a-Si: H for TSOs materials, specifically IGZO, as the active element in the thin film transistors used as the switching/driving current elements for pixel control. Just recently in 2012, Samsung announced for the first time the production of a fully transparent LCD with 90% energy consumption reduction when compared with a conventional LCD [75]. The improved energy efficiency arises from the elimination of the backlight required in the conventional LCD, as the fully transparent display uses the ambient light, significantly reducing the power consumption [71].

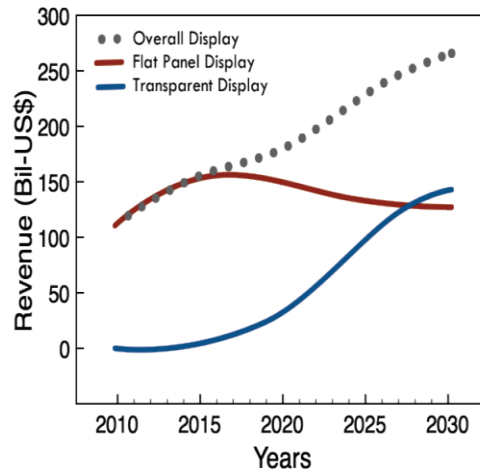


Figure I.6: Display market revenue evolution and forecast, adapted from Display bank [72].

1.8.4 Photocatalysis application

Photocatalysis is the procedure that enables change of solar energy into chemical energy needed for the decomposition of dyes or organic pollutants. The photocatalytic reactions usually occur on the semiconductor's surface. Metal oxide semiconductor (MOS) are considered as activators that help in catalyzing the complex radical chain reaction involved in the photocatalytic oxidation processes [76]. Generally, metal oxide photocatalysis is achieved using developed oxidation method which is realized by exercising a strong oxidizing species of OH radicals usually produced in situ. The OH radicals form the trigger to initiate a sequence of reactions that crumbles the complex dye macro-molecule into simpler and smaller, less harmful components [77-79].

A photocatalytic reaction is initiated while the particle of material semiconductor absorbs photon energy, this energy more than its gap energy. The photo-excited electron is moved from valence band energy (VB) to the conduction band energy (CB). The electron-hole pairs were created and diffused out to the surface of the photocatalyst and participate in the chemical reaction with the electron donor and acceptor groups of a compound. The electron-hole pairs modify the adjoining oxygen or water molecules into OH free radicals with super strong oxidization leading to stable end products as shown in Figure I.7 [80].

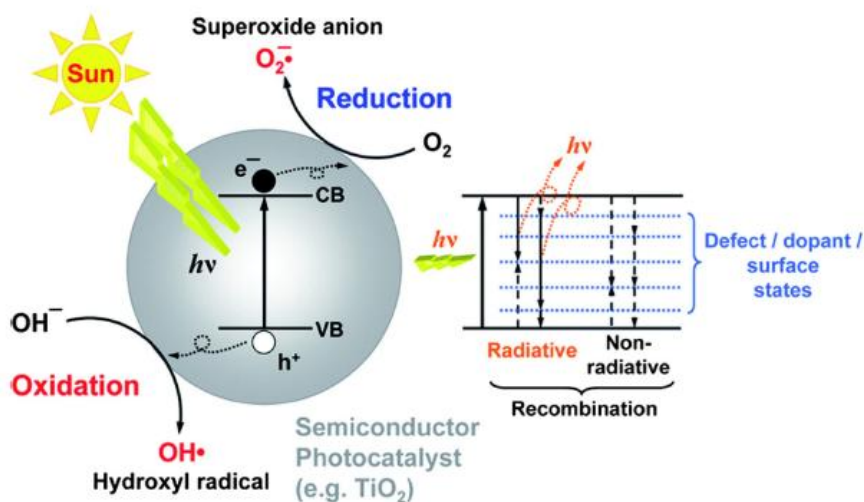


Figure I.7: Schematic diagram explaining the principle of photocatalysis [79]

1.8.5 Gas sensors

Transition metal oxides belong to a wide type of materials, with insulating, semiconducting and conducting metallic properties and make such materials extremely interesting from both the fundamental and technological viewpoint in the advancement of sensors [81, 82]. Gas sensors are an area in which it plays a fundamental function in monitoring environmental pollution. Gas detectors based on metal oxides semiconductor related to the difference of conductance induced by the phenomena of gases adsorption by subsequent surface reactions. As technology developments are growing so are environmental concerns and required to detect, a variety of kinds of pollutant and toxic gases for example; carbon monoxide (CO), carbon dioxide (CO₂), methane (CH₄), nitrogen oxides (NO₃), ammonia (NH₃), hydrogen sulphide (H₂S), ozone (O₃), and hydrochloric acid (HCl) also well-known as acid rain in the atmosphere. Thin films of porous SnO₂ and ZnO were the first established as gas sensing devices [83]. The addition of small amounts of noble metals such as platinum (Pt) and palladium (Pd) to these oxides was found to be effective in improving their sensing properties. Other significant metal oxide materials used as gas sensors for monitoring environmental pollutants include WO₃, MoO₃, TiO₂ etc [84-87].

1.9 Fundamental properties of nickel oxide (NiO) material

1.9.1 Physical and Chemical Properties of NiO

Nickel oxide (synonymous to nickelous oxide, green nickel oxide, nickel monoxide), also known as bunsenite after R. Bunsen, was discovered in 1858 and is only found pure in nature in a few locations around the world. Nickel (II) oxide has the chemical formula NiO

and is a chemically stable material. NiO is the most main marketable forms of refined, relatively pure nickel [88]. NiO actually very rare in nature, therefore, is typically produced artificially. Around numerous million of kilograms are formed annually [89]. NiO mainly exists in two forms such as black NiO and green NiO. The green crystal has almost exactly the stoichiometric composition of one Ni to one O atom, corresponding to the formula $\text{Ni}_{1.00} \text{O}_{1.00}$. The black material has an excess of O i.e., a deficiency of Ni with formula averaging $\text{Ni}_{0.98} \text{O}_{1.00}$ and belongs to the class of non-stoichiometric compounds. NiO is negligibly soluble; solubility in water is 1.1 mg/L at 20°C, the density of NiO is 6.67 g.cm^{-3} and the melting point is 2233 K. [88].

Numerous techniques used to produce NiO. Among this, heating greater than 400 °C, nickel powder with the company of oxygen this leads to the production of NiO. Also, green nickel oxide can be made using a heating mixture of nickel powder compound and water at 1000 °C, this method was used in several commercial processes, the rate for this reaction can be increased by the addition of NiO [90, 91]. The simplified and successful technique of fabrication using pyrolysis of a nickel (II) salts like hydroxide, nitrate, and carbonate, which yield a light green powder. Synthesis of the elements using heating the metal in oxygen or air atmosphere can yield grey to black powders which indicate non-stoichiometry [92].

1.9.2 Crystal structure

Nickel oxide crystallizes in a rock salt type lattice as shown in Figure I.8 each cubic unit cell has four nickel atoms and four oxygen atoms. Each nickel atom is bounded by six oxygen atoms and the same thing for oxygen atom has six nickel atoms surrounding it. This face-centered cubic (F.C.C) structure has a parameter of 4.1769 \AA at 26°C and the space group is $Oh^5 (Fm3m)$. Along any one of its triad axes, the (F.C.C) structure has a primitive rhombohedral cell with $\alpha = 60^\circ$. Figure I.8 shows a rhombohedral unit cell in the face-centered cubic cell. For nickel oxide, X-ray diffraction shows that the cubic lattice is slightly shifted to give a structure of rhombohedral cell with $\alpha = 60^\circ 4.2'$ at room temperature. The nickel-nickel distance is 2.9518 \AA for the distorted rhombohedral ($\alpha = 60^\circ 4.2'$ at 18°C), while this distance should be 2.9535 \AA for a cubic cell ($\alpha = 60^\circ$ and $a = 4.1769 \text{ \AA}$). This departure from the ideal-face centered cubic structure also was found to be temperature dependent. The amount of the distortion increases with the decrease of temperature [92, 93].

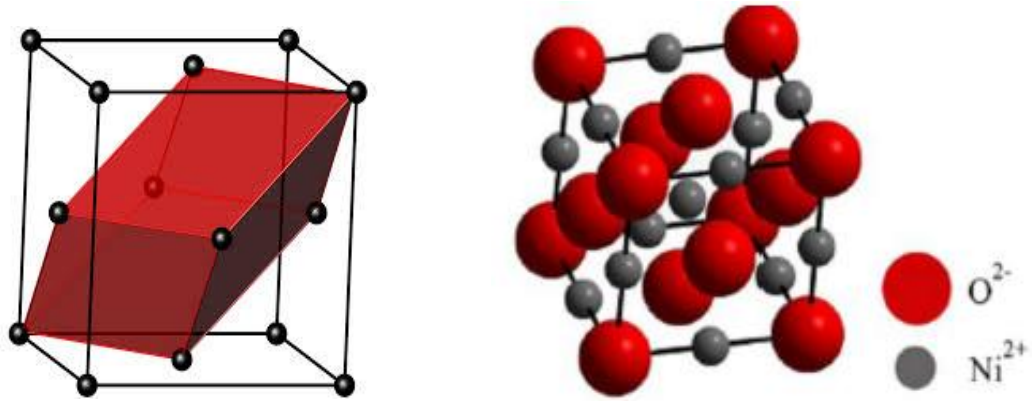


Figure I.8: The rhombohedral primitive cell of a face central cubic cell of nickel oxide [93]

Figure I.9 shows the phase diagram of a Ni-O binary system. The stable crystal structure of nickel oxide at a high temperature is polymorph bunsenite. By cooling the crystal, NiO converts to rhombohedral. It should be mentioned that these crystal structures form during thermodynamically stable transitions [94].

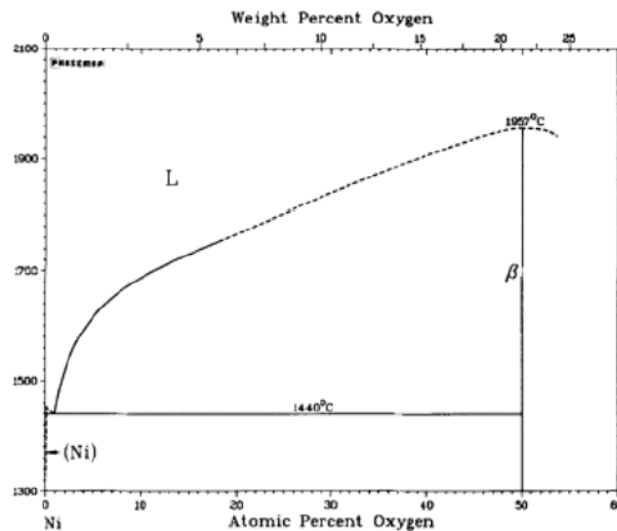


Figure I.9: Ni-O phase diagram [94]

1.9.3 Nickel thermal oxidation

Oxidation of the nickel has been a subject of great interest during almost a century, due to its application in several technologies. Bunsenite (NiO), as explained before, is one of the most common phases of nickel oxides. Other phases such as Ni_2O_3 and NiO_2 have also been claimed [95, 96]. These investigations, as shown before, concluded that NiO is a metal with a p-type semiconductor, in which nickel vacancies are the dominant defects.

In the Table I.2 some typical thermodynamic characteristics for nickel and NiO are presented. It is also possible to plot the behavior of G in an Ellingham diagram (Figure I.10) for the reaction (I.6).

	ΔH_f (kJ mol ⁻¹)	ΔG_f (kJ mol ⁻¹)	ΔS_f (kJ mol ⁻¹)
Ni(s)	0	/	29.9
NiO(s)	-239.701	-211.539	37.991

Table I.2: Standard thermodynamic properties of nickel and NiO [96]

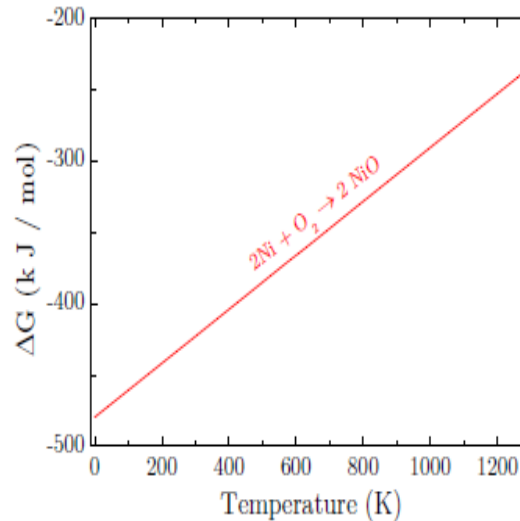


Figure I.10: Gibbs free energy versus temperature in nickel oxidation for the formation of NiO [96]

The conversion of nickel that occurs in the oxidation route is predicted to follow the reaction:



Using the Gibbs free energy and the shown in the Table I.2, it is possible to achieve that the reaction (I.2) is favorable ($\Delta G < 0$) and the NiO structure is formed.

1.9.4 Defects and impurities in NiO crystal

Crystalline solids show a periodic of atom in the crystal structure. A perfect stoichiometric metal oxide is an insulator and by introducing different defects inside the crystal, the mechanical, optical and electrical property of the oxide changes, respectively. Various categories of defects inside the crystal can exist such as point, line, planar and bulk defects.

Point defects are common in different crystals due to a small size of impurity atoms in the material. Interstitial, substitutional atoms and vacancies are common examples of point

defects in the crystal. Figure I.11 shows different point defects in a crystal. Dislocations (edge, screw or mixed) are examples of line defects. Planar defects can be devised into grain boundaries and stacking faults. The grain boundaries occur when various crystallographic planes reach together. The stacking fault structure is common in closed packed structures such as FCC and HCP and is caused by misalignment of several layers of atoms in a preferred orientation. The physical properties of a sample may be altered by modifying the defects number in the crystal. Fabrication processes, the percentage of impurities and annealing temperature have strong parameters affected by the film properties [97].

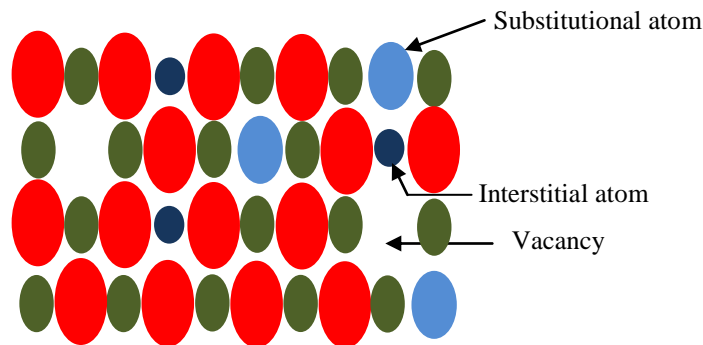


Figure I.11: Type of defects inside crystal

1.9.5 Electronic structure

Numerous calculations have been achieved on the structure of the NiO diatomic and its ground-state properties. The bonding between Ni and O can be observed as Ni^+O^- . The valence molecular orbitals (MOs) of NiO can be studied as derived from Ni^+ and O^- , as schematically shown in Figure I.12. The ${}^3\Sigma^-$ ground state of NiO is well established with the $1\sigma^2 1\pi^4 1\delta^2 1\pi^2$ configuration. The 1σ and 1π MOs are bonding orbitals between $\text{O}2p \sigma$ - $3d \sigma$ and $\text{O}2p \pi$ - $3d \pi$, respectively; the 2σ and 2π MOs are slightly anti-bonding; the 1δ is a nonbonding MO with the pure 3d character [98].

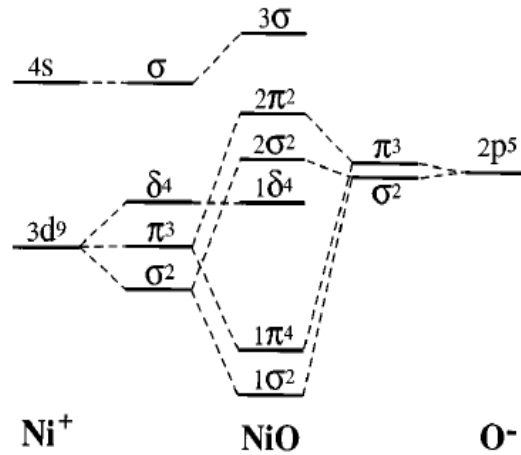


Figure I.12: A schematic molecular orbital diagram of the NiO molecule [98]

1.9.6 Optical properties

Nickel oxide is a broad band-gap semiconductor. The absorption edge is localized in the ultraviolet region, the existence of Ni^{3+} ions inner the oxide lattice shows charge transfer transition with the resulting absorption in the visible region [99, 100]. Various researchers have estimated the absorption of photon energy for NiO [101- 104]. Reported gap energy value for the NiO is in the range of 3.6 to 4 eV, however, the refractive index is 2.33 at the photon energy of 2 eV [105]. The valence band consists of localized nickel $3d$ -bands with a width of 4.3-4.4 eV [106, 107] at about 2eV above the Fermi level at -8.74 eV. Oxygen at the $2p$ band with large energy about 4–8 eV; were coupled with the nickel $3d$ states. However, the conduction band composes of unoccupied states of nickel $3d$, $4s$, and $4p$ [108]. Two main theories proposed for explaining the optical absorption gap in NiO: it is due to either a $p \rightarrow d$ transition in one Ni atom [109] or a $d \rightarrow d$ transition throughout two adjacent Ni atoms in the lattice [110].

1.9.7 Electrical properties

NiO has p-type oxide semiconductor character with broadband gap energy. Nominally pure stoichiometric NiO is an insulator as in Figure I.13 with a room temperature resistivity of the order of $10^{13} \Omega\text{-cm}$ is classified as a Mott-Hubbard insulator. Various theories have been done to explicate the insulating behavior of NiO; they include localized electron theory, band theory, chemical band approach and cluster theory. After intense theoretical and experimental investigations, the electronic structure of NiO remains controversial [111].

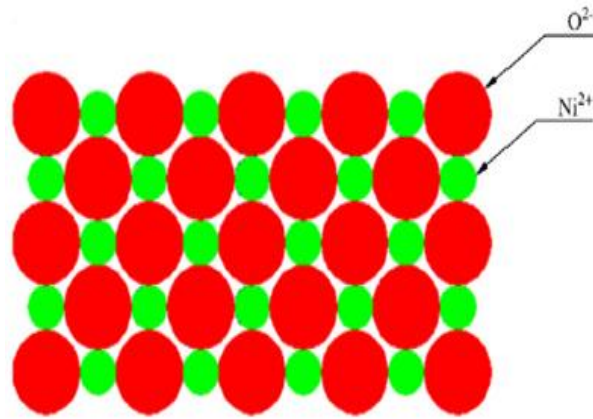


Figure I.13: A schematic of pure stoichiometric NiO crystal

Stoichiometric NiO is pale green. Black color in NiO has been attributed to the appearance of Ni^{3+} ions. Such ions are present in NiO as charge compensation for nickel vacancies [14]. Different samples have different conductivities suggesting conduction is dominated by the effect of random impurities or lattice defects. The appearance of nickel vacancies besides some other impurities like OH^- , CO_3^{2-} in defect nickel oxide affects the electronic structure of the oxygen atom where extra O1s peaks with greater binding energy are observed by XPS also the typical O1s peaks of oxygen in stoichiometric NiO [112].

Electronic conduction in undoped NiO is suggested to be due to the appearance of nickel vacancies or excess of oxygen. In the ionic crystal of NiO, the orientation of the film is usually affected by the orientation of O^{2-} when the active species of nickel and oxygen impinge separately on the growth of the film surface. This is because NiO has no directivity of a mixture between Ni^{2+} and O^{2-} and the radius of O^{2-} (0.140 nm) is superior to that of Ni^{2+} (0.069 nm) [113]. The oxygen atom is too large to permit any considerable concentration of interstitial O atoms in the structure. As a resulting overload of O in NiO creates vacancies in the normally occupied Ni sites as in Figure I.14. However, to preserve overall electrical neutrality in the crystal, two Ni^{2+} ions should be converted to Ni^{3+} for every vacant Ni^{2+} site. The Ni^{3+} ions introduced within the crystal in this way can be advised to be positive centers capable of jumping from one Ni^{2+} site to another. When an electron hops from a Ni^{2+} to a Ni^{3+} site, it is as if a positive hole moves around the Ni^{2+} sites. Thus overload of oxygen makes the NiO as p-type semiconductor [92].

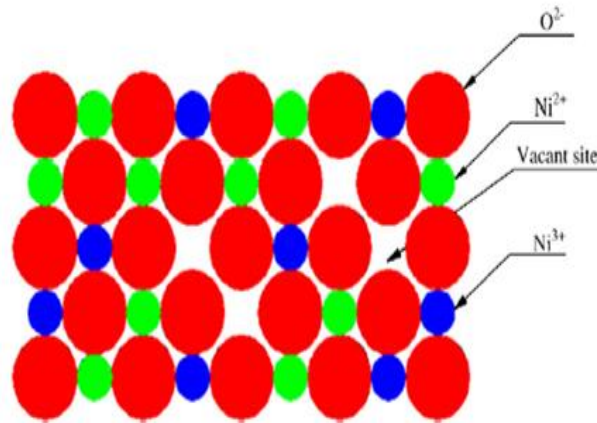


Figure I.14: A schematic of pure non-stoichiometric NiO crystal

1.9.8 Magnetic properties

Any modification in the structure of crystal with temperature actually is interrelated with the magnetic properties of NiO. The Néel temperature (TN) is the temperature at which antiferromagnetism changes to paramagnetism. Nickel oxide is antiferromagnetic at room temperature and paramagnetic above its Néel temperature $TN=250^{\circ}\text{C}$. At a temperature above TN, the structure of the crystal is cubic; whereas below TN, the lattice structure becomes distorted to rhombohedral. This distortion consists of diminution in the cubic structure along the (111) axes. Furthermore, the spin configuration in nickel oxide has been validated using neutron diffraction work. Figure I.15 shows the ordered arrangement of spin of the nickel ions in NiO under the TN temperature. Apparently; each magnetic unit cell contains four chemical unit cells [114].

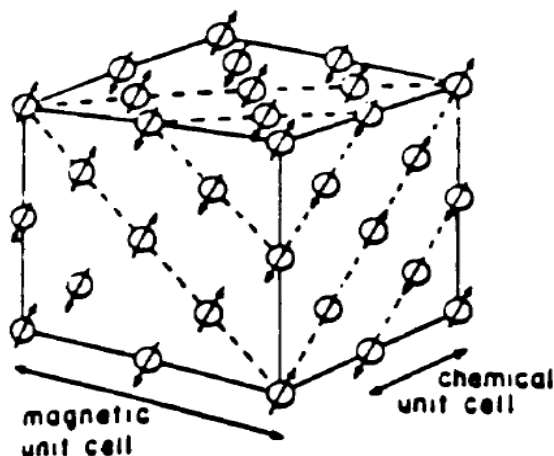


Figure I.15: Ordered arrangement of spins Ni²⁺ ions in NiO/the O²⁻ ions are not shown [114]

1.10 NiO thin films

Recently, NiO thin films were increased rapidly due to their importance in many applications in science and technology. NiO is one of the important P-type classes of semiconducting materials, which has attracted a good amount of research interest. This is because of the fact that NiO has unique optical, electrical and magnetic properties and finds a vast diversity of applications in energy efficient smart windows, automobile mirrors, building glazing, optoelectronic devices and hetero-junction solar cells... etc [115]. Nickel oxides is a wide band gap, low cost, advantageous ion storage material in points of cyclic stability and find applications in electrochromic devices transition metals, which reversibly changes the optical properties in the presence of electric field. Furthermore, NiO was applied to produce the Ni-Cd rechargeable batteries. NiO is now exploited in the recyclable protein separation and as biosensors. In addition, there are many applications and properties of nickel oxide based materials were investigated and proved in the field of antimicrobial activity, control infections and excessive antibiotic resistance [115-127].

1.11 Review of earlier work done on NiO based thin films

Various methods of deposition have been reviewed to prepare NiO thin films by many researchers, also diverse conditions with different characterization techniques were achieved. NiO materials in thin films, as well as powder forms, doped and undoped forms, have employed in the next sections [128,129].

1.11.1 Undoped NiO thin films

In (2002), Patil et al. [121] employed chemical spray pyrolysis (CSP) technique to deposit nickel oxide (NiO) thin films from hydrated nickel chloride salt solution on glass substrates. They studied the influence of sprayed solution volume on structural and optical characteristics by using X-ray diffraction (XRD), infrared (IR) and optical absorption. It was established that increase in volume solution leads an increase in the thickness and improvement of crystallinity of the film, consequently in the gap energy ranged in 3.58-3.4 eV.

In (2002), Hotovy et al. [130] deposited NiO thin films using DC reactive sputtering and reported the results concerning the characterization of some deposition parameters, as the oxygen quantity in the reactive plume and the sputtering mode (metal or oxide sputtering mode). They were found advantageous sensitivity and response towards NO₂ concentrations ranged from 1 to 10 ppm at low temperatures (160-200 °C). They also observed that the humidity was ameliorated in the NO₂ sensing properties, but further analysis we necessary to

comprehend the effective role of vapor of water on NiO surface.

In (2002), Lu et al. [122] have deposited nickel oxide thin layers using RF sputtering from a Ni target with mixture of oxygen and Argon gases onto heated Si and glass substrates and investigated the influence of process parameters including RF power, O₂/Ar ratio, and substrate temperature on the film properties like structure, transmittance and resistivity. They have established that the transmittance of films shows a strong dependence on the O₂/Ar percentage and it decays with the increase in the O₂/Ar ratio. Furthermore, it was reported that the increases of resistivity affected with an increase of substrate temperature.

In (2004), Kamal et al. [123] have deposited NiO thin films at different temperature using spray pyrolysis technique on a glass substrate. They have reported from the absorption spectra analysis that the electronic transitions are clearly affected by temperature and the dark electrical resistivity decreases with the increase of temperature.

In (2004), Sakata et al. [131] reported the structural analysis of NiO ultrathin films using laser molecular beam epitaxy on sapphire substrates. They explained the growth compartment of a NiO crystal domain along both an in the plane and out of plane directions at the nanoscale. They were drastically changed around 10-15 nm thick film range. They were observed dominated thermodynamic factors on the nucleation and growth in an ultrathin film range. However, they have reported that the step boundaries or terrace width of the substrate limited the growth speed in a thicker film range.

In (2005), Chen et al. [132] deposited nickel oxide thin layers using RF sputtering on glass substrates with pure oxygen and RF power 200 W, the correlation of structural properties on the thickness of the film were investigated. The X-ray diffraction (XRD) and transmission electron microscope (TEM) analyses indicated a polycrystalline structure. The films thicknesses were ranged in 50-300 nm. This leads to change the structural parameters, such as; strain, crystallite size, and dislocation density, with substrate temperature and thickness, was investigated. They observed increases in the crystallite size of the film as thickness increases; however the density of dislocation and strain decrease as the thickness increases.

In (2005), Franta et al. [133] examined the optical characterization of NiO thin layers by PLD method onto the quartz substrate and was performed using a multi-sample modification of the combined optical method had on measuring and explained the experimental data. They establish that the defects consisting in boundary roughness and index refraction profile in optical properties of the NiO films. Using AFM, they have obtained the roughness parameters of 55 and 72 nm thickness films were ranged in 4.9-5.8 nm.

In (2006), Reguig et al. [134] NiO thin films were elaborated using spray pyrolysis method from nickel chloride hexahydrate ($\text{NiCl}_2 \cdot 6\text{H}_2\text{O}$) solution in water at different concentrations of 0.05 to 0.5 M. They maintained substrate temperature during deposition is around 350°C with the solution flow rate fixed at 10 ml/min. They observed that at 350°C the reaction kinetic allows complete transformation of $\text{NiCl}_2 \cdot 6\text{H}_2\text{O}$ in cubic NiO. When the molar concentration is lower than 0.3 M they establish that the films are a p-type semiconductor and they convert into n-type for higher concentrations.

In (2007), Reguig et al. [127] studied nickel oxide thin layers grown on glass slides using cyclic spray pyrolysis method. Nickel chloride were dissolved in distilled water, by an easy perfume atomizer. The effects molarity of precursor on the physical properties was investigated and compared with other classical spray systems. After deposition, it was observed that the films crystallized. For all solution molarity utilized, it was observed the grain sizes of the films was between 25-30 nm with (111) direction as preferential orientation.

In (2007), Ghodsi et al. [135] NiO thin layers were prepared from $\text{NiCl}_2 \cdot 6\text{H}_2\text{O}$ precursor using the sol-gel route. On glass slides, the produced films were elaborated using a dip-coating technique. The impact of annealing temperature, number of layers, and dipping rate on the optical and structural characteristics of elaborated films were studied. From X-ray diffraction (XRD), the microstructure of deposited films and powder were characterized. Different peaks diffraction of NiO was observed from the XRD analysis. UV-visible spectrophotometers were achieved for the optical characteristics and the results proved that the films were transparent from the visible range. Optical constants such as index of refraction, extinction coefficient ...etc; have varied by changing the annealing of temperature, dipping rate and the number of layers.

In (2008), Ezema et al. [136] deposited NiO_x thin film on glass slides from aqueous solutions of nickel chloride and ammonia. Ammonia and hydroxyl solution was achieved as a complex agent with. X-ray diffraction and photomicrograph were investigated for the structure and optical properties. The optical properties showed that the films have band gap ranged from 2.10-3.90 eV and thickness varied from 0.061 to 0.346 μm . The average optical transmittance of the films was ranged from 50% to 91% in the UV-VIS-NIR wavelength. The obtained films can be exploited as optical coatings for poultry houses.

In (2008), Song et al. [137] prepared NiO nanorods using the microwave-assisted technique at different temperature (320 , 350 , and 400°C). They have established that the width of the NiO peaks decreases with an increase in the decomposition temperature upper than 400°C .

They have studied the optical absorption gap energy of the polycrystalline NiO nanorod. The value of gap energy of the as-deposited product was 3.7 eV. This result is smaller compared with the value of bulk material (4.0 eV). This effect was associated with the existence of defects or vacancies in the inter-granular regions and generating novel energy level to decrease the gap energy.

In (2009), Igwe et al. [138] have prepared nickel oxide thin films by chemical bath deposition technique on glass substrates using 3 ml of 1M of NiSO₄, 4 ml of 1M of KCl₄, and 1M of Ammonia for the reason of mixed agent. The films after that were annealed with various temperatures, 100, 150, 200, and 300°C. Ni(OH)₂ were decomposed under The thermal treatment to NiO_x thin film. The samples were very moderate materials with excellent electrochromic properties, firmly adhered to the substrate and resistant to chemicals. A higher transmittance was observed however the reflectance was lower with wavelength increases. Under various thermal treatments, the gap energy obtained was between 1.90 and 4.4 eV. The thickness achieved was ranged in 0.12-0.14 μm. This result supports other important applications, for example, P-type transparent conducting films and preparation of alkaline batteries (as a cathode material) anti-ferromagnetic layers.

In (2009), Pulimi et al. [139] attempted to synthesize NiO nanostructures using different anions such as nitrate, chloride, sulfate, and acetate through precipitation method. The crystallite size of samples is ranged from 2 to 6 nm. The films prepared with nickel sulfate or nickel acetate have lower crystallite size (2 nm), while the use of nickel nitrate and nickel chloride lead to relatively bigger crystallite size (4-6 nm). Magnetic measurements on nanocrystalline NiO indicate super-paramagnetic behavior for all the samples. NiO samples with lower crystallite size possess higher Ms (1.2-1.8 emu/g), compared to those with bigger crystallite size that show lower Ms Values (0.1- 0.4 emu/g).

In (2010), Saadati et al. [140] prepared NiO thin films at room temperature by using the e-beam physical vapor method on glass substrates for different thicknesses ranging in 285-645 nm. X-ray diffraction (XRD) and atomic force microscopy (AFM) was used for investigation of nanostructures of the prepared films. It was observed that the films grown belong (200) plane with preferred orientation and increased with a thickness of the film. In addition, crystallite size achieved from XRD study and grain size performed from AFM analysis increased with film thickness. Also, transmittance spectra of samples were investigated between 340-850 nm. The thickness and Refractive indices of the films were established using Swanepoel technique. Homogenous structures were performed from Optical functions of the films and the results are in excellent conformity with other reported using

different methods.

In (2010), Nibras et al. [141] prepared nickel oxide (NiO) thin films on cleaned glass substrates at 498 K temperature using spray pyrolysis deposition technique of thickness (1451.8Å). Optical properties of the film were examined using the measurement of the absorbance in the region varied from 300 to 1100 nm. Optical parameters like gap energy, index of refraction, absorption coefficient, extinction coefficient and optical conductivity, were calculated. High transmittances (~55-87%) of the films were found and high absorbance values at UV region which they decrease rapidly in the visible / near infrared region. Optical gap energy was evaluated and about 3.694eV.

In (2011), Patil et al. [142] employed a sol-gel spin technique for the deposition of nanocrystalline (NiO) thin films. Annealing the films in air for 1 h was done at 400°C - 700°C and the changes in the structural, morphological, and optical properties were investigated. The structure of NiO films was achieved by X-ray diffraction (XRD), all samples were the cubic phase structure and present a random orientation were reported. It is observed that the surface of the NiO film includes of nanocrystalline grains and uniform coverage the surface of the substrate with arbitrary orientation. After annealing NiO films, a decrease in the gap energy ranged from 3.86 to 3.47 eV was showed. It was reported that the annealing of NiO films enhances optical quality.

In (2011), Guziewicz et al. [143] fabricated NiO films by RF magnetron sputtering. Optical parameters of the samples were characterized using transmittance measurements. After annealing in oxygen or argon at the temperature ranged from 300°C to 900°C, a P-type conductivity of as-deposited films was verified. It was shown from NiO films that the transmittance meanly related to the amount of oxygen and temperature during sputtering. At room temperature films formed with an absence of oxygen had transmittance near 50% in the visible range and resistivity about 65 Ω cm. An increase in oxygen amount in deposition gas mixture leads to higher conductivity, but transmittance decreased below 6%.

In (2011), Venter et al. [144] resistively deposited nickel (Ni) on glass substrates and oxidized at temperatures ranging from 300 to 600°C. The oxidized Ni layers were subsequently characterized using scanning electron microscopy (SEM), X-ray diffraction (XRD) and UV-visible spectrophotometer ranged from 200 to 1000 nm. SEM results revealed a strong dependence of the surface texture and particle size on the oxidation temperature and time. XRD performed on the oxidized Ni indicated progressive transformation from nano grained polycrystalline Ni to NiO at high temperatures. Particle sizes, gap energy, refractive indices and film thicknesses were estimated using absorbance and transmission data.

In (2011), Thayumanavan et al. [145] developed an automated thin film formation technique to deposit NiO films at low temperatures using different molarities. To get better crystalline structure the produced films were annealed at 310°C. The Structural and optical properties were examined for the grown thin films with the developed instrument. The gap energy of the produced films was ranged from of 3.73 to 3.35 eV. The optical measurements confirmed that the transmittance of the grown film is up to 80 % and decreases with increasing of molarity of the solution.

In (2011), Mahmoud et al. [146] prepared crystalline and non-crystalline (NiO) thin layers using chemical spray pyrolysis technique on glass substrates with nickel acetate tetrahydrate as a source of nickel with temperatures varied from 225 to 350°C. The results displayed at temperature bellow ($T = 225^{\circ}\text{C}$) an amorphous structure of the films, however single phase with the cubic structure of NiO, were formed at higher $T \geq 275^{\circ}\text{C}$. The optical parameters such as refractive index and the extinction coefficient were calculated using corrected transmittance and reflectance measurements were the wavelength ranged in 250- 2400 nm.

In (2012), Reddy et al. [147] prepared Nickel Oxide (NiO) thin films on Corning 7059 glass substrates at different oxygen partial pressures in the range of 1×10^{-4} to 9×10^{-4} mbar by dc reactive method. Structural properties of samples demonstrate cubic structure with polycrystalline nature and orientation along (220) plane. With raising the oxygen pressure at 1×10^{-4} to 5×10^{-4} mbar the optical transmittance and gap energy values of the samples increased and decreased with increasing the oxygen pressure. Using (SEM) measurement, fine grains have been shown at a pressure of 5×10^{-4} mbar.

In (2013), Ismail et al. [148] prepared transparent (NiO) thin films using simple spray pyrolysis technique from hydrated nickel chloride salt solution ($\text{NiCl}_2 \cdot 6\text{H}_2\text{O}$) on silicon (n-type) and glass substrates with different temperatures (280, 320, 360, and 400°C) and with different solution concentrations (0.025, 0.05, 0.075, and 0.1M). The XRD results showed that the deposited films have an amorphous structure when deposited at temperature of $T=280^{\circ}\text{C}$ and concentration of 0.025 M. At higher temperatures ($T=320, 360, 400^{\circ}\text{C}$) and solution concentrations of (0.05, 0.075, 0.1 M), the deposited films had cubic polycrystalline structure formed and preferred orientation along (111) plane. The band energy of NiO film increased and ranged from 3.4 - 3.8 eV as the molarity decreased from 0.1 to 0.05 M.

In (2013), Verma et al. [149] have been elaborated NiO thin layers on Si substrates using (PLD) technique. Influence of different parameters, including substrate temperature, laser energy, and frequency, the number of pulses and oxygen pressure of NiO thin films were studied. They observed that the films prepared at high energy (3.5 mJ/ mm^2), high oxygen

pressure (100 Pa) with 10 Hz repetition laser frequency have resulted in (200) preferred orientation. They establish that (111) as preferred orientations having large crystallites size are free from cracks and display anti-ferromagnetic behavior of NiO structure.

In (2013), Dalavi et al. [150] were prepared the NiO films from nickel acetate precursor by sol-gel dip coating technique. From XPS measurement, they observed that the sample had a NiO phase. Their morphological measurement reported that the sample comprises of porous micro-granules which serve as conduits for effective electrolyte access into the film structure that can be helpful for the augmenting the optical modulation of 51% end CE of 49 cm²/C at 550 nm. They also found the chromaticity measurements of a luminous transmittance difference of about 49.45%.

In (2014), Tareq et al. [151] prepared NiO thin layers on quartz substrates using a pulsed 532 nm Q-Switched Nd: YAG laser. The X-ray diffraction (XRD) revealed that the samples are crystalline in nature. Furthermore, in the case of the thicker sample with great annealing temperature was observed, which was associated with an increased grain size. The morphology of elaborated samples was interpreted using (AFM) and (SEM) measurement, with annealing temperature and the grain size increase. The grain sizes value (10, 23 and 40 nm) for thin films annealing at 200, 300 and 400°C respectively. Optical measurement demonstrated high transparency (about 92 % ranged from 400 to 900 nm) of the NiO thin film and direct allowed band gap value ranged from 3.51 to 3.6 eV.

In (2015), Alamelu et al. [152] used gel combustion technique to elaborate NiO nanoparticles using various weight ratios of oxidizer (O), nickel nitrate hexahydrate and fuel (F) such as cassava starch respectively. Their result report that the photocatalytic degradation of MB dye achieved in sunlight and showed greater degradation efficiency (94%) when the oxidizer to fuel ratio is 1:1, with a comparison to UV light. The produced nanoparticles were tested for energy storage where electrochemical studies depicted a reversible capacity of 940 and 785 mA h/g when O: F ratio was taken as 1:0.5 and 1:1 respectively. Antibacterial activity was also performed against a fungal strain and two bacterial strains.

In (2016), Gomaa et al [153] were deposited thin films of NiO on a glass substrate using chemical bath deposition method. Nickel chloride and ammonia were used as precursor and a complexing agent, respectively. The optical analysis demonstrates that the gap energy is ranged in 2.1 - 3.9 eV with increasing of annealing temperature from 300 to 473 K. It proves that NiO films are broad gap energy semiconductor material. The obtained gap energy values are in excellent conformity with reported values for NiO films.

1.11.2 Doped NiO thin films

In (2010), Jang et al. [154] have fabricated the lithium-doped nickel oxide films using RF magnetron sputtering on glass substrates. The lithium concentration in the films was varied from 0-16 wt %. The influence of Li concentration on properties such as microstructure, resistivity, and electrical stability has investigated. They are reported that the doped Li ions contribute to occupy crystal defect sites such as vacancies or segregate on the film surface. It was illustrating that firstly; doped Li occupied the Ni vacancies in the film, thus, decreasing the electrical conductivity. However, some lithium was insulated on the surface of the film when the Li doping level was further increased and has formed bulges. As a result, the Li-doped NiO films showed a decrease in the electrical aging and leads in a relatively stable conductivity.

In (2011), Zhao et al. [155] deposited Cu-doped NiO thin films by electrochemical deposition (cathodic deposition) method on the fluorine-doped tin oxide (F: SnO₂; FTO) coated glass substrates from organic solutions. From XRD results, they confirmed that the films were amorphous or short-range ordered NiO grains and had a face-centered cubic Ni_xCu_{1-x}O. They observed that the Cu doped films show the formation of nanorods of Ni_xCu_{1-x}O, indicating that the Cu doping increases the crystallinity of the films, and the quantity of nanorods increases with the Cu amount in the films. They also found that film with the Cu/Ni molar ratio of 1:8 has better electrochromic (EC) properties compared to the undoped NiO films and the Cu doped films showed high-quality EC properties promote and which can promote the potential application of EC devices.

In (2012), Moghe et al. [156] were produced NiO thin layers using low-cost spray pyrolysis technique. The influence of copper (Cu) doping level on the variation of the optical properties behavior was reported. They found that at different concentrations of Cu, the films have excellent adherent and smooth films. Their XRD analysis explains that all the films had a cubic structure with (111) preferred orientation. They have found that the roughness varying from 6.5 to 15 nm with the variation of Cu concentration. The resistivity was observed to decrease with Cu concentration increase, also the activation energy was remarked to decrease and ranged from 0.307- 0.282 eV. It is observed that with an increase in Cu content, the value of band gap decrease from 3.20 to 2.96 eV.

In (2013), Chen et al. [157] were deposited NiO films with and without Cu adding using RF reactive sputtering on cleaned silicon and quartz glass substrates from Ni and Ni/Cu composite targets. They found that with the incorporation of Cu, XRD analyses indicated the existence of Cu₂O in NiO-Cu films. From Hall measurement, they observed that the hole mobility was decreased as the increasing doping level of Cu, likely due to the significant lattice scattering by high Cu incorporating concentration. They have reported that the decreased in optical gap energy of NiO films with the increasing Cu concentration.

In (2014), Ben Amor et al., [158] were prepared Magnesium-doped nickel oxide thin films (NiO:Mg) with ratio [Ni]/[Mg]=0%, 1%, 2% and 3% using the spray pyrolysis technique on glass substrates at 450°C using NiCl₂•4H₂O and MgCl₂•6H₂O as source of nickel and magnesium respectively. The XRD patterns displayed cubic structure of the films and (111) plane as a preferred orientation. The gap energies are found to be ranged from 3.56 - 3.62 eV with a magnesium content. The influence of the Mg content on the disorder was reported in terms of Urbach energy. The electric conductivity of the films was studied using the impedance spectroscopy in the frequency ranged from 5 Hz to 13 MHz with temperatures varied from 300 to 500°C. They have found an electrical performance with Mg-doped nickel oxide thin films.

In (2014), Sta et al., [159] were prepared un-doped and lithium (Li) doped NiO thin films on glass slides using the sol-gel spin coating method using nickel acetate and lithium chloride as the source of nickel and lithium respectively. The impact of layers number on the structural, optical and electrical characteristics of NiO thin films was investigated by atomic force microscopy and X-ray diffraction (XRD), respectively. They were described that the thickness of the film was increased as the number of layers increases. They were obtained that four is the better appropriate number of layers of un-doped NiO films with high optical transparency. By using this proposition, lithium doped NiO films were fabricated. They displayed that the films morphology changes with increasing the Li level in the solution. XRD reveals the polycrystalline of the films with preferred orientations were estimated. They were reported that the increase of Li content leads an increase in the optical transmittance of the films in the visible wavelength.

In (2014), Kerli et al., [160] were fabricated NiO thin films with airbrush spraying technique on glass slides at 400°C using a solution of nickel nitrate hexahydrate and Indium doped (3, 5,

8 and 10 at. %). The influence (In) doping level on the physical properties of NiO thin films was investigated using X-ray diffraction (XRD), scanning electron microscopy (SEM), optical transmittance and four-probe measurement. From The XRD pattern, they found that films prepared at 8 and 10 at% doped films have an amorphous structure. Whereas the sample elaborated at pure, 3% and 5 at% have a cubic structure. They have funded that the optical gaps energy varies with indium content. in addition, they have shown that electrical resistivity increases as (In) doping increases.

In (2015), Denny et al., [161] reported the optical and electrical characteristics as well as the electronic structure of sodium-doped (Na-doped) nickel oxide (NiO) thin films. The samples were examined using X-ray photoelectron spectroscopy (XPS), reflection electron energy loss spectroscopy (REELS) and X-ray absorption near edge structure. From XPS spectra, the identification of NiO phase for all films and Ni-O bonds through the Ni 2p spectra were proved. The REELS results affirmed that after doping with Na the gaps energy of NiO samples were decreased. They have reported that Na-doped NiO thin films achieved low resistivity comparatively with undoped NiO thin films. Furthermore, it is observed that Na-doped NiO films fabricated at room temperature show the high transparency of 80% in the visible wavelength and p-type conductivity with low electrical resistivity around $11.57 \Omega \text{ cm}$. They have obtained that Na content acting a crucial function in enhancing the optical and electrical characteristics of NiO thin films.

In (2016), Sharma et al., [162] were successfully fabricated thin films of $\text{Ni}_{1-x}\text{Zn}_x\text{O}$ using spray pyrolysis method with different composition ($x = 0, 0.01, 0.05$ and 0.10) on glass slides. They have examined the structural, morphological, electrical and optical characteristics with annealing temperature. They have funded that the annealing of the samples leads to enhanced surface morphology and better crystallinity. The elaborated films displayed an increase in conductivity accompanied by a decrease in gap energy as Zn doping concentration increases. However, they were observed that the effect is more important if the films are annealed, where the average transparency appears an increase of about 10% over the elaborated thin films. They interpreted that the red-shift of the optical gap energy is referred to the deep states in the band gap. They have reported that when Zn content increased the activation energy decreased.

In (2016), Mrabet et al., [163] deposited Lanthanum doped nickel oxide NiO: La thin films onto glass substrates at 450°C , by the spray pyrolysis technique using nickel and lanthanum

chlorides as precursors. Their XRD analysis reported that the films matched well to cubic structure and (111) plane as preferential orientation. The Raman spectra study showed the bands correlated to NiO structure. In addition, using SEM observations, they found that all films demonstrate porous microstructures with rough surfaces and spherical nanoparticles of about 40 nm in size. They reported that the Lanthanum doped NiO suggest gap energy value ranged from 3.63 to 3.84 eV. Some optical constants (refractive index, extinction coefficient, dielectric constants, and dispersion parameters) were also studied. However, the PL spectra confirmed the appearing of peaks associated to the electronic transition of the Ni²⁺ ions and others approving the existence of some defects linked to La content in the NiO matrix. They have also found that La doping allows the enhancement of the electrical conductivity as well as Haacke's figure of merit relatively minimum, three orders of magnitude.

In (2016), Wang et al., [164] were deposited in K-doped NiO films (Ni_{1-x}K_xO) on glass substrates using a rapid pyrolysis sol-gel technique. The structural, morphological, electrical and optical characteristics of the films were reviewed using X-ray diffraction, scanning electron microscopy and atomic force microscope, Hall Effect measurement, and UV-vis spectrophotometer, respectively. They reported that all of the elaborated films were cubic structure and the residual stress in the films varied as K doping concentration increases from residual compressive stress to residual tensile stress. The morphologies the films were greatly affected by the K doping concentration. They confirmed that the transmittance decreased on the whole with increasing K doping concentration, they have also examined that the optical band gaps energy of the films were approximately constant.

In (2017), Ben Amor et al., [165] Were successfully elaborated Cadmium doped NiO thin films using spray pyrolysis method at 460 °C with ratio [Cd]/[Ni] = 0%, 1%, 2%, 3% and 4% on glass substrates. The Cd doping concentration effects on structural, morphological and optical characteristics were investigated. The XRD analyses report the polycrystalline of all films with cubic structure and reveal (111) plane as preferential orientation. Raman spectra demonstrate the observation of bands matched well to NiO structure. They have reported that the Cd is well incorporated in the host lattice without destruction of the crystal structure. From all films, the transmittance spectra, a high transparency was observed (~80%) in the visible region. The calculated gap energy was in the range of 3.89-3.80 eV with the cadmium content.

References

- [1] K.L. Chopra, S. Major, D.K. Pandya, Transparent conductors: A status review, *Thin Solid Films*, 102 1 (1983) 1-46.
- [2] P.P. Edwards, A. Porch, M.O. Jones, D.V. Morgan, Basic materials physics of transparent conducting oxides, R.M. Perks, 19 (2004) 2995-3002.
- [3] G.J. Exarhos, X.D. Zhou, Discovery-based design of transparent conducting oxide films, *Thin Solid Films*, 515 18 (2007) 7025-7052.
- [4] D.S. Ginley, J. D. Perkins, *Handbook of transparent conductors*, Springer science, New York, 2010.
- [5] D.S Ginley, C. Bright, *Transparent Conducting Oxides*, *Mrs Bulletin*, 25 8 (2000) 15-18.
- [6] C.G. Granqvist, A. Hultaker, Transparent and conducting ITO films: new developments and applications, *Thin Solid Films*, 411 1 (2002) 1-5.
- [7] R.G. Gordon, Criteria for Choosing Transparent Conductors, *Mrs Bulletin*, 25 8 (2000) 52-57.
- [8] K.C. Sanal, Development of p-type transparent semiconducting oxides for thin film transistor applications, phd thesis, cochin university of science and technology, 2014.
- [9] K. Badeker, *Annalen der Physik* 327, 749-66.
- [10] L. Holland, *Vacuum deposition of thin films*. First Edition, Published 1956 by Wiley & Sons.
- [11] A.H. Rosenfeld, T. Kaarsberg, M. J. Romm, Technologies to Reduce Carbon Dioxide Emissions in the Next Decade, *Phys. Today*, 53 11 (2000) 29-34.
- [12] J. Bellingham, R. Phillips, W. A. Adkins, Electrical and optical properties of amorphous indium oxide, *J. Phys.: Condens. Matter.* , 2 28 (1990) 6207.
- [13] H. Hosono, M. Yasukawa, H. Kawazoe, Novel oxide amorphous semiconductor: Transparent conducting amorphous oxides, *J. Non-Cryst. Solids*, 203(1996) 334-44.
- [14] H. Sato, T. Minami, S. Takata, T. Yamada, Transparent conducting p-type NiO thin films prepared by magnetron sputtering, *Thin Solid Films*, 236 (1993) 27-31.
- [15] H. Kawazoe, M. Yasukawa, H. Hyodo, M. Kurita, H. Yanagi, H. Hosono, P-type electrical conduction in transparent thin films of CuAlO_2 , *Nature*, 939 42 (1997) 389.
- [16] Y. Kim, H. Sachse, C. Machala, M. L. May, C. Müller-Meskamp, Highly Conductive PEDOT:PSS Electrode with Optimized Solvent and Thermal Post-Treatment for ITO-Free Organic Solar Cells, *Adv. Funct. Mater.*, 216 (2011) 1076.
- [17] Y. M. Chien, F. Lefevre, I. Shih, R. Izquierdo, A solution processed top emission OLED with transparent carbon nanotube electrodes, *Nanotechnology*, 21 13 (2010) 134020.
- [18] K. S. Kim, Y. Zhao , H. Jang , S. Y. Lee , J. M. Kim, Large-scale pattern growth of graphene films for stretchable transparent electrodes, *Nature*, 457 (2009) 706.

- [19] N. M. Pinto Neves, Al-doped ZnO ceramic sputtering targets based on nanocrystalline powders produced by emulsion detonation synthesis – deposition and application as a transparent conductive oxide material , PhD thesis , university of Nova de Lisboa, 2015.
- [20] A. Martinson, D. Ginley, Synthesis of Single Phase SrCu_2O_2 from Liquid Precursors, *Journal of Young Investigators*, 3 (2004) 10.
- [21] D. S. Ginley, Photoelectrochemistry and Electrosynthesis on Semiconducting Materials, *Novel Materials for Photovoltaic Technologies*, 11 99 (1999) 103-110.
- [22] H. Kawazoe, H. Yanagi, K. Ueda, H. Hosono, Transparent p-Type Conducting Oxides: Design and Fabrication of p-n Hetero-junctions, *MRS Bulletin*, 25(2000) (8) 28-36.
- [23] G. Hautier, A. Miglio, G. Ceder, G.M. Rignanese, and X. Gonze, Identification and design principles of low hole effective mass p-type transparent conducting oxides, *Nature Communications*, 4 (2013)2292.
- [24] H. Yanagi, S. I. Inoue, K. Ueda, H. Kawazoe, H. Hosono, N. Hamada , Electronic structure and optoelectronic properties of transparent p-type conducting CuAlO_2 , *Journal of Applied Physics*, 8 87 (2000) 4159-4163.
- [25] P. Isherwood, development of transparent conducting oxides for photovoltaic applications, PhD Thesis, Loughborough University, 2015.
- [26] A.N. Banerjee, K.K. Chattopadhyay, Recent developments in the emerging field of crystalline p-type transparent conducting oxide thin films, *Progress in Crystal Growth and Characterization of Materials*, 50 (2005) 52–105.
- [27] H. Ohta, H. Hosono, Transparent oxide optoelectronics, *Materials Today*, 6 (2004) 42–51.
- [28] R Manoj, Characterisation of Transparent Conducting Thin Films Grown by Pulsed Laser Deposition and RF Magnetron Sputtering, PhD Thesis, cochin university of science and technology, 2006.
- [29] J.C.C. Fan, J.B. Goodenough, X-ray photoemission spectroscopy studies of Sn-doped indium-oxide films, *J. Appl. Phys.* 1977 (48) 3524.
- [30] I. Hamberg, C.G. Granqvist, K.F. Berggreen, B.E. Sernelius, L. Engstrom, Band-gap widening in heavily Sn-doped In_2O_3 , *Phys. Rev. B.*, 30 (1984) 3240.
- [31] O.N. Marysov, A.J. Freeman, Electronic band structure of indium tin oxide and criteria for transparent conducting behavior, *Phys. Rev .B.* 64 (2001) 233111-1.
- [32] P. Drude, Zur Elektronentheorie der Metalle, *Annalen der Physik*, 306 (1900) 566–613.
- [33] K. Sreenivas, T. S. Rao, A. Mansingh, S. Chandra, Preparation and characterization of RF sputtered indium tin oxide films, *J. Appl. Phys.*, 57 (1985) 384.
- [34] J. Bardeen, W.Shockley, Deformation Potentials and Mobilities in Non-Polar Crystals, *Phys.Rev.*, 80 (1950)72.
- [35] A .R. Huston, Piezoelectric Scattering and Phonon Drag in ZnO and CdS, *J. Appl. Phys.*, 32 (1961) 2287.

- [36] H. Ehrenreich, Band Structure and Transport Properties of Some 3–5 Compounds, *J. Appl. Phys.*, 32 (1961)2155.
- [37] M. Amini, First-principles study of defects in transparent conducting oxide materials, PhD thesis, University of Antwerp, 2014.
- [38] J. C. Manificier, Thin metallic oxides as transparent conductors, *Thin Solid Films*, 90 (1982) 297.
- [39] K.L. Chopra, S. Major, D.K. Pandya, Transparent conductors: A status review, *Thin Solid Films*, 102 (1983) 1-46.
- [40] A. L. Dawar, J. C. Joshi, Semiconducting transparent thin films: their properties and applications, *J. Mater. Sci.*, 19 (1984) 1.
- [41] I. Luciu, RF plasma synthesis and characterization of thin films for transparent conductors, PhD thesis, university of Trento, 2012.
- [42] J. matthijn dekkers, transparent conducting oxides on polymeric substrates by pulsed laser deposition, PhD thesis, University of Twente, 2007.
- [43] I. Saadeddin, preparation and characterization of new transparent conducting oxides based on SnO₂ and In₂O₃: ceramics and thin films, PhD thesi, university of bordeaux i, 2007.
- [44]. P.K. Biswas, A. De, N.C. Pramanik, P.K. Chakraborty, K. Ortner, V. Hock , S. Korder, Effects of tin on IR reflectivity, thermal emissivity, Hall mobility and plasma wavelength of sol–gel indium tin oxide films on glass, *Mater. Lett.*, 57 (2003), 2326.
- [45] H. Kim, J.S. Horwitz, A. Piqué, C.M. Gilmore , D.B. Chrisey, Electrical and optical properties of indium tin oxide thin films grown by pulsed laser deposition, *Appl. Phys.* A69 (1999) S447.
- [46] C. G. Van de Walle, J. Neugebauer, First-principles calculations for defects and impurities: Applications to III-nitrides, *Journal of Applied Physics*, 95 8 (2004), 3851–3879.
- [47] R. H. Jan Franken, Transparent conducting oxide contacts and textured metal back reflectors for thin film silicon solar cells, PhD thesis, University of Utrecht, 2006.
- [48] P.D.C. King, T.D. Veal, Conductivity in transparent oxide semiconductors, *J. Phys.: Condens. Matter*, 23 (2011) 334214.
- [49] A. Janotti, C.G. Van de Walle, Fundamentals of zinc oxide as a semiconductor, *Rep. Prog. Phys.*, 72 (2009)126501.
- [50]C. Kilic, A. Zunger, n-type doping of oxides by hydrogen, *Appl. Phys. Lett.*, 81 1 (2002), 73-75.
- [51] P. A. Iles, S. I. Soclof, Design factors for transparent conducting layers in solar cells, I. E. E. Photovoltaic Specialists Conference, (1976) 978.
- [52] M. Dressel, G. Gruener, *Electrodynamics of Solids: Optical Properties of Electrons in Matter - Appendix B.*: Cambridge University Press, 2002.
- [53] A.N. Banerjee, K.K. Chattopadhyay, Recent developments in the emerging field of crystalline p-type transparent conducting oxide thin films, *Progress in Crystal Growth and Characterization of Materials*, 2005(50) 52–105.

- [54] B.G. Lewis, D.C. Paine, Applications and Processing of Transparent Conducting Oxides, MRS Bull, 25 8 (2000) 22-27.
- [55] J. Lewis, S. Grego, E. Vick, B. Chalamala, D. Temple, Mechanical Performance of Thin Films in Flexible Displays Mat. Res. Soc. Symp. Proc., 814 (2004)1-10.
- [56] A. Khan, Synthèse de Cuprates de Strontium (SrCu_2O) par MOCVD comme couche mince d'oxyde transparent conducteur de type P, thèse de doctorat, Université de Grenoble, 2006.
- [57] M. Gratzel, Dye-sensitized solar cells, Journal of Photochemistry and Photobiology, 4 (2003) 145-153.
- [58] M. Gratzel, Solar Energy Conversion by Dye-Sensitized Photovoltaic Cells, Inorganic Chemistry, 44 20 (2005) 6841- 6851.
- [59] B. O'Regan, J. Durrant, Kinetic and energetic paradigms for dye-sensitized solar cells: moving from the ideal to the real, Accounts of Chemical Research, 42 (2009)1799-1808.
- [60] B O'Regan, M.Grätzel, A low-cost, high-efficiency solar cell based on dye-sensitized colloidal TiO_2 films, Nature, 353 6346 (1991) 737-740.
- [61] G. Smestad, Testing of dye sensitized TiO_2 solar cells II: Theoretical voltage output and photoluminescence efficiencies, Solar Energy Materials and Solar Cells, 32 3 (1994) 273-288.
- [62] D. S. Bhachu, the synthesis and characterization of metal oxide thin films, PhD thesis, UCL University, 2013.
- [63] C. G. Granqvist, Transparent conductors as solar energy materials: A panoramic review, Sol. Energ. Mat. and Sol. C, 91 (2007), 1529.
- [64] Y. Sawada, Y. Taga, TiO_2 /(indium tin oxide) multilayer film: a transparent IR reflector, Thin Solid Films, 116 (1984), L55.
- [65] J. Karlsson, A. Roos, Annual energy window performance vs. glazing thermal emittance - the relevance of very low emittance values, Thin Solid Films, 392 (2001), 345.
- [66] C. Granqvist, Handbook of Inorganic Electrochromic Materials Elsevier, Amsterdam.(2004).
- [67] C. Granqvist, A. Azens, P. Heszler, L. Kish, L. Österlund, Nanomaterials for benign indoor environments: Electrochromics for "smart windows", sensors for air quality, and photo-catalysts for air cleaning, Sol. Energ. Mat.and Sol. C., 91 (2007), 355.
- [68] C. G. Granqvist, Electrochromic tungsten oxide films: Review of progress 1993–1998, Sol. Energ. Mat. Sol. C., 60 (2000), 201.
- [69] S. Deb, S. Lee, C. Tracy, J. Pitts, B. Gregg, H. Branz, Stand-alone photovoltaic-powered electrochromic smart window Electrochim. Acta., 46 (2001), 2125.
- [70] P. Ágoston, point defect and surface properties of In_2O_3 and SnO_2 : a comparative study by first-principles methods, PhD thesis, Darmstadt University, 2011.
- [71] J. Alfonso, C. Frescas, Transparent Oxide Semiconductors for Emerging Electronics, PhD thesis, King Abdullah University of Science and Technology, 2013.
- [72] Display bank. Display Market Forecast. <http://www.displaybank.com> (2012).

- [73] Sharp Corporation. Sharp announces production of world's first IGZO LCD panels. <http://www.macdailynews.com> (2012).
- [74] E. Fortunato, P. Barquinha, R. Martins, Oxide Semiconductor Thin-Film Transistors: A Review of Recent Advances, *Adv. Mater.*, 24 (2012), 2945-2986.
- [75] [Phys.org/news](http://phys.org/news). Samsung shows transparent 46-inch LCD panel, (2012).
- [76] D. Chatterjee, S. Dasgupta, Visible light induced photocatalytic degradation of organic pollutants, *J. Photochem. Photobiol C*, 6 (2005), 186–205.
- [77] S.H.S. Chan, T.Y. Wu, J.C. Juan, C.Y. The, Recent developments of metal oxide semiconductors as photocatalysts in advanced oxidation processes (AOPs) for treatment of dye waste-water, *J. Chem. Technol. Biotechnol.*, 86 (2011) 1130–1158.
- [78] F. Han, V.S.R. Kambala, M. Srinivasan, D. Rajarathnam, R. Naidu, Tailored titanium dioxide photocatalysts for the degradation of organic dyes in wastewater treatment: A review, *Applied catalysis a general* 359 (2009) 25–40.
- [79] A.B. Djurusic, Y.H. Leung, A.M. Ching, Strategies for improving the efficiency of semiconductor metal oxide photocatalysis, *Mater Horizons* 1 (2014) 400-410.
- [80] A. Kumar, synthesis, characterization and application of bare and zinc doped nickel oxide nanoparticles, master of philosophy in chemistry, Shoolini University, 2013.
- [81] P.A. Cox, *Transition Metal Oxides: An introduction to their Electronic Structure and Properties*, Glarendon, Oxford (1992).
- [82] N. Erdman, K.R. Poeppelmeier, M. Asta, O. Werschkow, D.E. Ellis, L.D. Marks, The structure and chemistry of the TiO₂-rich surface of SrTiO₃ (001), *Nature*, 419 (2002) 55.
- [83] T. Mochida, K. Kikuchi, T. Konda, H. Veno, Y. Matura, Highly sensitive and selective H₂S gas sensor from R.F. sputtered SnO₂ thin film, *Sensors and Actuators B*, 24/25 (1995) 433.
- [84] J. Yang, H. Lim, S.D. Han, Influence of binders on the sensing and electrical characteristics of WO₃-based gas sensors, *Sensors and Actuators B*, 1999 (60) 71.
- [85] D. Mutschal, K. Halzner, E. Obermeier, Sputtered molybdenum oxide thin films for NH₃ detection, *Sensors and Actuators B*, 35 (1996) 320.
- [86] H.M. Lin, T.Y. Hsu, C.Y. Tung, C.M. Hsu, Hydrogen sulfide detection by nanocrystal PT doped TiO₂-based gas sensors, *Nanostructured Materials*, 6 (1995) 1001-1004.
- [87] S. Swapnasmitha, A studies in thin films investigations on pulsed laser deposited tungsten trioxide thin films for chromic and gas sensor applications, PhD thesis, Sri Venkateswara University, 2007.
- [88] Department of Health, Public Health Service.ATSDR. Toxicological Profile for Nickel. Atlanta, GA, USA: US (2005).
- [89] F. Ullmann Y. S. Yamamoto, F. T. Campbell, R. Pfefferkorn, J. F. Rounsaville, Ullmann's encyclopedia of industrial chemistry. VCH (1996).
- [90] P. Pradyot, *Handbook of Inorganic Chemicals*, McGraw-Hill, Publications, (2002).

- [91] N.A. Bakr, S.A. Salman, A.M. Shano, Effect of Aqueous Solution Molarity on Structural and Optical Properties of Nickel Oxide Thin Films Prepared by Chemical Spray Pyrolysis Technique, *International Journal of Current Research*, 41 (2014) 15-30.
- [92] B. Sasi, Preparation and characterization studies of nanostructured nickel oxide and lithium doped nickel oxide thin films, PhD thesis, University of Kerala, 2007.
- [93] Z. Zhiwei, Oxygen reduction on lithiated nickel oxide as a catalyst and catalyst support, PhD thesis, Case Western Reserve University, 1993.
- [94] A. M. Soleimanpour, Synthesis, fabrication and surface modification of nanocrystalline nickel oxide for electronic gas sensors, PhD thesis, University of Toledo, 2013.
- [95] H. A. Juybari, M.M. Bagheri-Mohagheghi, M. Shokooh-Saremi, Nickel–lithium oxide alloy transparent conducting films deposited by spray pyrolysis technique, *Journal of Alloys and Compounds*, 509 (2011) 2770-2775.
- [96] A. Citra, G. V. Chertihin, L. Andrews, M. Neurock, Reactions of Laser-Ablated Nickel Atoms with Dioxygen. Infrared Spectra and Density Functional Calculations of Nickel Oxides NiO, ONiO, Ni₂O₂, and Ni₂O₃, Superoxide NiOO, Peroxide Ni(O₂), and Higher Complexes in Solid Argon, *The Journal of Physical Chemistry A*, 101 (1997) 3109-3118.
- [97] W.D. Callister, *Fundamentals of materials science and engineering- An intergrated approach*. Second ed., USA: John Wiley & Sons, 2005.
- [98] Wu. Hongbin, L.S. Wang, A study of nickel monoxide (NiO), nickel dioxide (ONiO), and Ni(O₂) complex by anion photoelectron spectroscopy, *J. Chem. Phys.*, 1 (1997) 107.
- [99] A. J. Hassan, Study of Optical and Electrical Properties of Nickel Oxide (NiO) Thin Films Deposited by Using a Spray Pyrolysis Technique, *Journal of Modern Physics*, 5 18(2014) 52764.
- [100] N. Tsuda, K. Nasu, A. Fujimori, K. Siratori, *Electronic Conduction in Oxides*, second ed., Springer, Berlin, 2000.
- [101] P. Pramanik, S. Bhattachraya, A Chemical Method for the Deposition of Nickel Oxide Thin Films, *J. Electrochem. Soc.*, 137 (1990) 3869.
- [102] R.H. Misho, W.A. Murad, G. RFatahalah, I. M.Abdul-Aziz ,H. M.Al-doon, Preparation and optical properties of thin nickel oxide solid films, *Physica Status Solidi (a)* , 109 (1988) K 101.
- [103] D. Adler, J. Feinleib, Electrical and Optical Properties of Narrow-Band Materials, *Physical Review B-Solid State* 2, B2 (1970) 3112.
- [104] R.S. Conell, D.A. Corrigan, B.R. Powell, The electrochromic properties of sputtered nickel oxide films, *Solar Energy Mater Solar Cells*, 1992 (25) 301-313.
- [105] R. J. Powell, W. E. Spicer, Optical Properties of NiO and CoO, *Physical Review B (Solid State)*, 2 (1970) 2182.
- [106] H.A.E. Hagelin-Weaver, J.F. Weaver, G.B. Hoflund, G.N. Salaita, Electron energy loss spectroscopic investigation of Ni metal and NiO before and after surface reduction by Ar⁺ bombardment, *Journal of Electron Spectroscopy and Related Phenomena*, 134 (2004) 139.

- [107] K.S. Lee, H.J. Koo, K.H. Ham, W.S. Ahn, Crystal Molecular Orbital Calculation of the Lanthanum Nickel Oxide by Means of the Micro-Soft Fortran, *Bull. Korean. Chem. Soc.*, 16 (1995) 164.
- [108] S. Hüfner, T. riserer, Electronic structure of NiO, *Physical Review B*, 33 (1986) 7267.
- [109] A.R. Williams, J. Kübler, K. Terakura, *Phys. Rev. Lett.*, 54 (1985) 2728.
- [110] R. Merlin, Electronic Structure of NiO, *Phys Rev. Lett.*, 54 (1985) 2727.
- [111] J.G. Aiken, A.G. Jordan, Electrical transport properties of single crystal nickel oxide, *Journal of Physics and Chemistry of Solids*, 29 (1968) 2153.
- [112] H.J. Koo, K.S. Lee, W.S. Ahn, Crystal Molecular Orbital Calculation of the Lanthanum Nickel Oxide by Means of the Micro-Soft Fortran, *Bull.Korean.Chem.Soc.*, 16 (1995), 164.
- [113] H.W. Ryu, G.P. Choi, G.J. Hong, J.S. Park, Growth and Surface Morphology of Textured NiO Thin Films Deposited by Off-Axis RF Magnetron Sputtering, *Jpn. J. Appl.Phys.*, 43 (2004) 5524.
- [114] Z. Zhiwie, Oxygen reduction lithiated nickel oxide as catalyst and catalyst support, PhD thesis case Western Reserve university, 1993.
- [115] M. Doudi, N. Talebian, The study of antibacterial properties of NiO thin film using Sol-gel Synthesis, *Biological Forum – An International Journal*, 8 1 (2016) 127-131.
- [116] Y. Y. Xi, B. Q. Huang, A. B. Djurišić, C.M.N. Chan, F.C.C. Leung, W. K. Chan, D.T.W. Au, Electrodeposition for antibacterial nickel-oxide-based coatings, *Thin Solid Films*, 517 (2009) 6527-6530.
- [117] Y.W. Baek, Y.J. An, Microbial toxicity of metal oxide nanoparticles (CuO, NiO, ZnO, and Sb₂O₃) to Escherichia coli, Bacillus subtilis, and Streptococcus aureus, *Science of the Total Environment*, 409 (2011) 1603–1608.
- [118] I.S. Lee, N. Lee, J. Park, B.H. Kim, Y.W. Yi, T. Kim, T.K. Kim, I.H. Lee, S.R. Paik, T. Hyeon, Ni/NiO Core/Shell Nanoparticles for Selective Binding and Magnetic Separation of Histidine-Tagged Proteins, *J. Am. Chem. Soc.*, 2006 (128), 10658.
- [119] J. Kim, Y. Piao, N. Lee, Y. Park, I.H. Lee, J.H. Lee, S.R. Paik, T. Hyeon, Magnetic Nanocomposite Spheres Decorated with NiO Nanoparticles for a Magnetically Recyclable Protein Separation System, *Adv. Mater.*, 22 (2010), 57.
- [120] S. Mohan, P. Srivastav, S. N. Maheshwari, S. Sundarb, R.Prakash, Nano-structured nickel oxide based DNA biosensor for detection of visceral leishmaniasis (Kala-azar), *Analyst.*, 136 (2011), 2845.
- [121] P. S. Patil, L.D. Kadam, Preparation and characterization of spray pyrolyzed nickel oxide (NiO) thin films, *Appl. Surf. Sci.*, 199 (2002) 211.
- [122] Y.M. Lu, W.S. Hwang, J. S. Yang, Effects of substrate temperature on the resistivity of non-stoichiometric sputtered NiO_x films, *Surf. Coat. Technol.*, 155 (2002) 231.
- [123] H. Kamal, E.K. Elmaghraby, S.A. Ali, K. Abdel-Hady, Characterization of nickel oxide films deposited at different substrate temperatures using spray pyrolysis, *J. Crystal Growth*, 262 (2004) 424-434.
- [124] P. Mohanty, P. Chandanarath, R. Mallick, N.C. Biswal, UV–visible studies of nickel oxide thin film grown by thermal oxidation of nickel, *Physica B*, 405 (2010) 2711-2714.

- [125] S. Nandy, U. N. Maiti, C. K. Ghosh, K. K. Chattopadhyay, Enhanced p-type conductivity and band gap narrowing in heavily Al doped NiO thin films deposited by RF magnetron sputtering, *J. Phys: Condens. Matter*, 219 (200) 115804.
- [126] B.A. Reguig, A. Khelil, L. Cattin, M. Morsli, J.C. Bernede, Properties of NiO thin films deposited by intermittent spray pyrolysis process, *Appl. Sur. Science*, 253 (2007) 4330-4334.
- [127] Q. Pan, J. Liu, Facile fabrication of porous NiO films for lithium-ion batteries with high reversibility and rate capability, *J. Sol. St. Electrochem.*, 13 10 (2009) 1591-1597.
- [128] H. Soonmin, Preparation and Characterization of Nickel Oxide Thin Films: A review, *International Journal of Applied Chemistry*, 2016(12)2, 87-93.
- [129] A. M. Shano Al-Askari, Effect of Aqueous Solution Molarity on Structural and Optical Properties of Nickel- Cobalt Oxide Thin Films Prepared by Chemical Spray Pyrolysis Method, Master of Science, University of Diyala, 2014.
- [130] I. Hotovy, V. Rehacek, P. Siciliano, S. Hascik, S. Capone, L. Spiess, Sensing characteristics of NiO thin films as NO₂ gas sensor, *Thin Solid Films*, 2002 (418) 9-15.
- [131] O. Sakata, M.S. Yi, A. Matsuda, J. Liu, S. Sato, S. Akiba, A. Sasaki, M. Yoshimoto, Structural analysis of NiO ultra-thin films epitaxially grown on ultra-smooth sapphire substrates by synchrotron X-ray diffraction measurements, *Appl. Surf. Sci.*, 2004 (221) 450.
- [132] H.L. Chen, Y.M. Lu, W.S. Hwang, Effect of Film Thickness on Structural and Electrical Properties of Sputter-Deposited Nickel Oxide Films, *Materials Transactions*, 46 4 (2005) 872-879.
- [133] D. Franta, B. Negulescu, L. Thomas, P.R. Dahoo, M. Guyot, L. Ohlidal, J. Mistrik, T. Yamaguchi, Optical properties of NiO thin films prepared by pulsed laser deposition technique, *Appl. Surf. Sci.*, 244 (2005) 426-430.
- [134] B.A. Reguig, M. Regraguib, M. Morsli, A. Khelil, M. Addou and J.C. Bernede, Effect of the precursor solution concentration on the NiO thin film properties deposited by spray pyrolysis, *Sol. Energy Mater. Sol. Cells*, 90 (2006) 1381-1392.
- [135] F. E. Ghodsi, S. A. Khayatiyan, Preparation and determination of optical properties of NiO thin films deposited by dip coating technique, *Surface Review Letters (SRL)*, 14 2 (2007) 219-224.
- [136] F. I. Ezema, A.B.C Ekwealor, R.U. Osuji, Optical properties of chemical bath deposited nickel oxide (NiO_x) thin films, *Sociedad Mexicana de Ciencia y Tecnología de Superficies y Materiales*, 21 1 (2008) 6-10.
- [137] X. Song, L. Gao, Facile synthesis of polycrystalline NiO nanorods assisted by microwave heating, *Journal of the American Ceramic Society*, 91 (2008) 3465-3468.
- [138] H.U. Igwe, O.E. Ekpe, and E.I. Ugwu, Effects of Thermal Annealing on the Optical Properties of Nickel Oxide Thin Films Prepared by Chemical Bath Deposition Technique, *Journal of Science and Technology*, 10 2 (2009) 806-811.
- [139] V. R. R. Pulimi, P. Jeevanandam, The effect of anion on the magnetic properties of nanocrystalline NiO synthesized by homogeneous precipitation, *Journal of Magnetism and Magnetic Materials*, 321(2009) 2556-2562.

- [140] F. Saadati, A. R. Grayeli, H. Savaloni, Dependence of the optical properties of NiO thin films on film thickness and nanostructure, *Journal of Theoretical and Applied Physics*, 4 1(2010) 22-26.
- [141] Nibras F. Al-Shammary, Optical characteristics of NiO thin film on glass formed by Chemical spray pyrolysis, *Journal of kufa- Physics*, 2 1 (2010) 20.
- [142] V. Patil, S. Pawar, M. Chougule, P. Godse, R. Sakhare, S. Sen, P. Joshi, Effect of Annealing on Structural, Morphological, Electrical and Optical Studies of Nickel Oxide Thin Films, *Journal of Surface Engineered Materials and Advanced Technology*, 1 (2011) 35-41.
- [143] M. Guziewicz, J. Grochowski, M. Borysiewicz, E. Kaminska, Z. Domagal, W. Rzdokiewicz, B.S. Witkowski, K. Golaszewka, R. Kruszka, M. Ekielski, Electrical and optical properties of NiO films deposited by magnetron sputtering, *Optica Applicata*, XLI 2 (2011) 431- 440.
- [144] A. Venter, J. R. Botha, Optical and electrical properties of NiO for possible dielectric applications, *S Afr J Sci.*, 107(1/2) (2011) 268.
- [145] S. Sriram, A. R. Balu, A. Thayumanavan, Design and Development of Automated Liquid Flow Deposition method for thin film formation, *Archives of Applied Science Research*, 3 2 (2011) 438-447.
- [146] A. M. Safwat, S. Alshomer, M. A. Tarawnh, Structural and Optical Dispersion Characterization of Sprayed Nickel Oxide Thin Films, *Journal of Modern Physics*, 2 (2011)1178-1186.
- [147] Y. A. K. Reddy, A. M. Reddy, A. S. Reddy, P. S. Reddy, Preparation and Characterization of NiO Thin Films by DC Reactive Magnetron Sputtering, *Journal of nano-and Electronic Physics*, 4 4 (2012)1-4.
- [148] R. A. Ismail, S. Ghafari, G. A. Kadhim, Preparation and characterization of nanostructured nickel oxide thin films by spray pyrolysis, *Appl Nanosci*, 3(2013) 509-514.
- [149] V. Verma, M. Katiyar, Effect of the deposition parameters on the structural and magnetic properties of pulsed laser ablated NiO thin films, *Thin Solid Films*, 527 (2013) 369-376.
- [150] D.S. Dalavi, R. Devan, R.S. Patil. Y.R. Ma, P.S. Patil, Electrochromic performance of sol–gel deposited NiO thin film, *Mater. Lett.*, 90 (2013) 60-63.
- [151] H.S. Tareq, Study the Effect of Rapid Thermal Annealing on Thin Films Prepared By Pulse Laser Deposition Method, *Eng. &Tech. Journal*, 32 3 (2014) 444-452.
- [152] K.A. Ramasami, M.V. Reddy, G.R. Balakrishna, Combustion synthesis and characterization of NiO nanoparticles, *Materials Science in Semiconductor Processing* 40 (2015) 194–202.
- [153] M.M. Gomaa, M. Boshta, B.S. Farag, M.B.S. Osman, Structural and optical properties of nickel oxide thin films prepared by chemical bath deposition and by spray pyrolysis techniques, *J. Mater. Sci.: Mater. Electron*, 27 (2016) 711-717.
- [154] W.L. Jang, Y.M. Lu, W.S. Hwang, W.C. Chen, Electrical properties of Li-doped NiO films, *Journal of the European Ceramic Society*, 30 (2010) 503-508.
- [155] L. Zhao, G. Su, W. Liu, L. Cao, J. Wan, Z. Dang, M. Song, Optical and electrochemical properties of Cu-doped NiO films prepared by electrochemical deposition, *Appl. Surf. Sci.*, 257 (2011) 3974-3979.

- [156] S. Moghe, A.D. Acharya, R. Panda, S.B. Shrivastava, M. Gangrade, T. Shripathi, V.Ganesan, Effect of copper doping on the change in the optical absorption behaviour in NiO thin films, *Renewable Energy*, 46 (2012) 43-48.
- [157] W. Y. Chen, J.S. Jeng, K.L. Huang, Modulation of Ni valence in p-type NiO films via substitution of Ni by Cu, *J.S. Chen, J. Vac. Sci. Technol. A*, 31(2013) 021501.
- [158] M. Ben Amor, A. Boukhachem, K. Boubaker, M. Amlouk, Structural, optical and electrical studies on Mg-doped NiO thin films for sensitivity applications, *Materials Science in Semiconductor Processing*, 27(2014) 994-1006.
- [159] I. Sta, M. Jlassi, M. Hajji, H. Ezzaouia, Structural, optical and electrical properties of undoped and Li-doped NiO thin films prepared by sol-gel spin coating method, *Thin Solid Films*, 555(2014) 131-137.
- [160] S. Kerli, U. Alver, H. Yaykaşlı, Investigation of the properties of In doped NiO films, *Applied Surface Science*, 318 (2014) 164-167.
- [161] Y.R. Denny , K. Lee , C. Park , S. K. Oh , H. J. Kang , D.S. Yang , S. Seo, Electronic, electrical and optical properties of undoped and Na-doped NiO thin films, *Thin Solid Films Part B*, 591(2015) 255-260.
- [162] R. Sharma, A. D. Acharya, S. B. Shrivastava, M. M. Patidar, V. Ganesan, Studies on the structure optical and electrical properties of Zn-doped NiO thin films grown by spray pyrolysis, *Optik*, 127 11(2016) 4661-4668.
- [163] C. Mrabet, M. Ben Amor, A. Boukhachem, M. Amlouk, T. Manoubi, Physical properties of La-doped NiO sprayed thin films for optoelectronic and sensor applications, *Ceramics International*, 42 5 (2016) 5963-5978.
- [164] N. Wang, C.Q. Liu, C.Q. Liu B. Wen, H.L. Wang, W.P. Chai, Structural, electrical and optical properties of K-doped NiO films prepared by rapid pyrolysis sol-gel technique, *Thin Solid Films*, 616 (2016) 587-593.
- [165] M. Ben Amor, A. Boukhachem, A. Labidi, K. Boubaker, M. Amlouk, Physical investigations on Cd doped NiO thin films along with ethanol sensing at relatively low temperature, *Journal of Alloys and Compounds*, 693 (2017) 490-499.

Chapter II

*Synthesis, methods and
materials
characterization*

2.1 Introduction

Nowadays, there has been growing demand for production of thin films for their wide range of potential applicability in the various fields of science and technological development in modern society. A lot of efforts have been taken to obtain thin films of required properties such as thickness, texture, uniformity, adhesivity, orientation etc. for particular applications. Thin film properties such as structural, morphological, electrical, optical, electrochemical etc. for the determined material are effectively correlated on the method of deposition, the substrate material, the substrate temperature, rate of deposition, and background pressure. Modern technology requires thin films for a diversity of applications [1].

In view of this, the chapter is broadly classified in two parts; the first part deals with the various synthesis techniques employed to prepare the material, while in the following part different characterization methods applied to study and characterize the various properties of the grown thin films are discussed along with their principles and instrumentation.

2.2 Mechanism of thin films formation

The deposition process of a thin film can be classified into three basic phases:

- Preparation of the film forming particles (atoms, molecules, cluster).
- The particles transport from the source to the substrate.
- The particles adsorption on the surface of substrate and finally growth of thin film.

These phases can be associated to the specific deposition process and/or on the choice of the deposition parameters, be considered as either independent or as influencing one another. The thin film is prepared by deposition of the film materials (metals, semiconductors, insulators, dielectric etc.) atom by atom on a substrate through a phase transformation. An adequate time interval between the two successive depositions of atoms and also layers are required. In thermodynamically stable films, all atoms (or molecules) will take up positions and orientations energetically are similar with the neighboring atoms of the substrate or to the earlier deposited layers, and then the effect substrate or the first layers will diminish gradually [2].

2.3 Thin Film Growth Process

Major steps that constitute a typical thin film deposition process are [2]:

1. Thermal accommodation;
2. Adsorption (physisorption) of atoms/molecules;
3. Diffusion in the Surface;
4. Formation of atoms- atoms and substrate- atoms bondings (chemisorption);

5. Nucleation: aggregation of single molecules /atoms;
6. Formation of structure and microstructure (single crystalline, polycrystalline, amorphous, roughness and defects, etc.);
7. Modification within the bulk of the film, e.g. diffusion, grain growth etc.

In thin film formation there exist three mechanisms of thin film condensations which can be distinguished, depending on the strength of interaction between the growing atoms and the deposited atoms of the film in the substrate. These are:

- a) The layer by layer growth;
- b) A three-dimensional nucleation, forming, growth and coalescence of islands;
- c) Absorption of monolayer and subsequent nucleation on the top of this layer.

In most cases, the mechanism (b) takes place and we shall focus our interest on this mechanism in brief.

2.3.1 Condensation

The structural behavior and properties of films are associated with the growth process. A thin film is most commonly prepared by the condensation of atoms from the vapor phase of a material means, the transformation of a gas into a liquid or solid. The condensation of vapor atom is dedicated to its interaction with the impinged surface in the following manner. The impinging atom is attracted to the surface by the instantaneous dipole and quadrupole moments of the surface atoms. As a result, the atoms losses its velocity component normal to the surface in a short time provided the incident kinetic energy is not too high. The vapor atoms are then physically absorbed (called adatom), but it may or may not be completely thermally equilibrium. It may move over the surface and its own kinetic energy parallel to the surface. The adatom has a finite stay or residence time on the surface during which it may interact with other adatoms to make a stable cluster and be chemically absorbed, with the liberation of the heat of condensation. If not absorbed, the adatom evaporates or desorbs into the vapor phase [3].

2.3.2 Nucleation

The stable clusters are called nuclei and the mechanism of formation nuclei is named nucleation i.e. nucleation is the birth stage of a film. Condensation is started by the production of the small cluster through the combination of numerous absorbed atoms. There are two kinds of nucleation occur during the production of a film [3];

- Homogeneous nucleation: The total free energy is used in the formation of a cluster of adatoms.

- Heterogeneous nucleation: Particular shapes of clusters are formed by collisions of atoms on the surface of the substrate, and in the vapor phase its supersaturation is adequately high.

2.3.3 Growth

The process of enlargement of the nuclei to final form a coherent is termed as growth. Different stages of film growth are presented in Figure II.1. There are four stages of the growth process based on the electron microscope observations are [3]:

1. The island stage;
2. The coalescence stage;
3. The channel stage;
4. The continuous film stage.

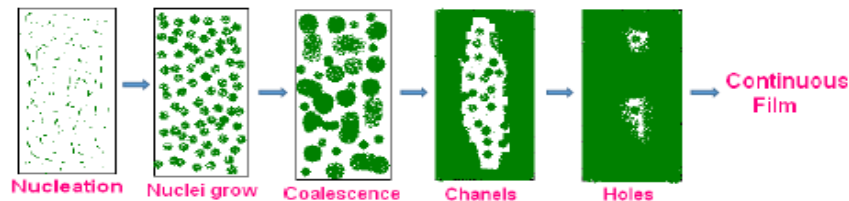


Figure II.1: Different stages of thin film growth [2]

2.3.3.1 The Island Stage

When a substrate under impingement of condenses monomers is observed in the electron microscope, the first evidence of condensation is a sudden burst of nuclei of fairly uniform size. The smallest nuclei detected have a size around 2.0-3.0 nm. The growth of nuclei is three dimensional, but the growth of nuclei is parallel to the substrate and is better than that normal to it. This is probably because growth occurs largely by the surface diffusion of monomers on the substrate, rather by direct impingement from the vapor phase. The tendency to produce a structure island is increased by [2]:

- At high substrate temperature.
- At a low boiling point of film material.
- At low deposition rate.
- At weak binding energy between film material and substrate.
- At a high surface energy of the film material.
- At a low surface energy of the substrate.

2.3.3.2 The Coalescence Stage

As island increases their size by further deposition and comes closer to each other, the larger ones appear to grow by coalescence of the smaller ones. The coalescence occurs in less

than 0.1s for the small nuclei. After coalescence has taken place, the island assumes a more hexagonal profile is often faulted. A sequence of micrographs illustrating the effects as shown in Figure II.1 where Island which eventually becomes crystallographically shaped [2].

2.3.3.3 The Channel Stage

When larger islands grow together they have channels of interconnected holes of exposed substrate in the form of a grid structure on the substrate. As deposition continues, secondary nucleation appears in these channels and forms the last stage of nucleation [2].

2.3.3.4 Continuous Film Stage

This is the final phase of the film growth. This process is slow and stuffing the empty channels which requires a considerable amount of deposits. These empty channels are filled by secondary nucleation, growth and coalescence and in this way a continuous film are formed [2].

2.4 Thin Film Deposition Techniques

After choosing material for the present work, the following step was to select an appropriate deposition technique. Thin film deposition can be generally grouped into physical and chemical methods. Physical methods include sputtering and vacuum evaporation... etc. by evaporation; the material meaning deposited has been converted to a gaseous state either and then deposited on the substrate .

Under chemical processes, we have the gas phase and chemical methods contain; chemical vapor deposition (CVD), Photo CVD Laser CVD, plasma enhanced CVD... etc. however the liquid phase chemical processes include; electrodeposition; chemical bath deposition, spray pyrolysis and liquid phase epitaxy... etc. The broad classification of deposition techniques is outlined in the Figure II.2 . An enormous number of deposition processes that exist and just only some methods are detailed in the next parts with special emphasis on the spray pyrolysis method [4].

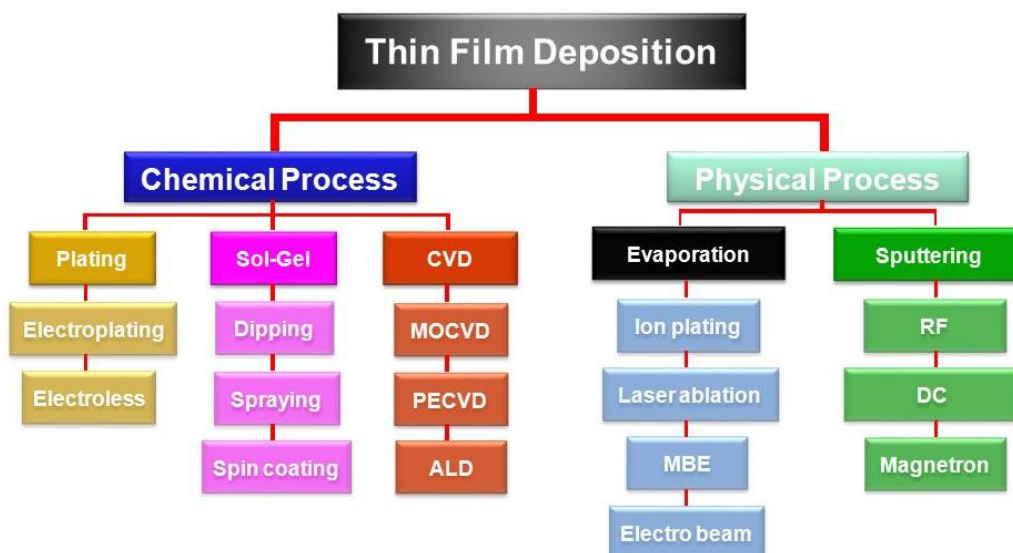


Figure II.2: Schematic diagram of classifications of thin films deposition techniques [4]

2.5 Criteria for selection of a deposition technique

In order to optimize the desired film characteristics, a good comprehension of the advantages and restrictions applicable to each technique is necessary [5]. The choice of a specific deposition technique related to some factors, they are:

- The material to be deposited;
- The rate of deposition;
- Limitations imposed by the substrate, e.g, maximum deposition temperature;
- Adhesion of the deposits to a substrate;
- Throwing power;
- The purity of target material;
- Availability of the required equipment;
- Cost;
- Ecological considerations;
- The abundance of the material (to be deposited).

2.6 Physical methods of deposition

Physical deposition uses thermodynamic or mechanical means to fabricate required thin films. These techniques are costly but offer relatively more reliable and further reproducible results. Furthermore, the physical methods need high energies, and chemical reactions are not used to store these energies. Commercial physical deposition systems favor requiring a low-pressure vapor medium to function properly [5].

2.6.1 RF Sputtering

The RF sputter derives its name from using energy in the radio wave spectrum range. This technique is widely applied by the industry to coat materials that are used in different technological applications. In this technique, an RF potential is excited to the metal electrode placed behind the dielectric plate target, as illustrated in Figure II.3. Typical RF frequencies employed are ranged from 5 to 40 MHz. At RF potentials, the electrons oscillating in the alternating field have sufficient energies to induce ionizing collisions, and discharge will be self-sustained. Since the electrons have much higher mobilities than ions, many more electrons will reach the dielectric target surface during the positive half cycle than ions during a negative half cycle, and the target will become self-biased negatively. The negative dc potential on the insulator target surface repulses electrons from the vicinity of this surface, creating a sheath enriched in ions in front of the target. The target was bombarded by ions and sputtering is reached. Quartz, aluminum oxide, boron nitride thin films and various glasses have been successfully prepared using RF sputtering technique. For deposition of thin films, the use of RF sputtering is great importance because it enables more economical deposition on to the substrates of large areas [6].

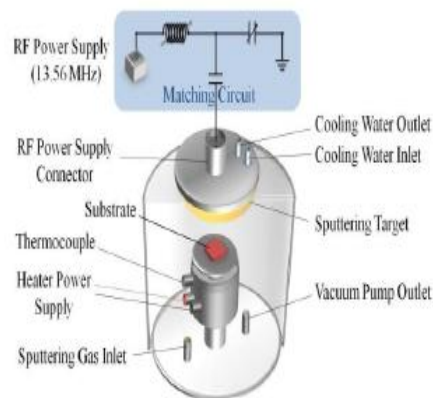


Figure II.3: Schematic diagram of RF sputtering system [7]

2.6.2 Pulsed Laser Deposition

Pulsed laser deposition (PLD) is an adaptable deposition technique for thin films growth and can be applied to deposit very large of materials. A pulsed laser, usually in the ultra-violet (UV) wavelength, is periodically used to ablate the material of the target in a high vacuum. As a result, the solid material was transformed into plasma and generated a plume from the direction of the substrates. This plume condensed as it reaches the substrate to form nanostructured films. A schematic diagram of the PLD system is illustrated in Figure II.4 [7].

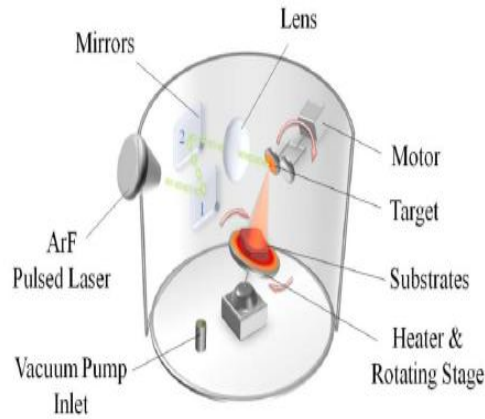


Figure II.4: Schematic diagram of PLD system [7]

2.6.3 Thermal evaporation

The thermal evaporation process contains evaporating source materials in a vacuum chamber below 10^{-6} Torr and condensing the evaporated particles on a substrate. In this process, thermal energy is provided to a source from which atoms are evaporated for deposition in the substrate. Heating of the source material can be finished by any of which the material to be evaporated is attached. Larger volumes of source material can be heated in crucibles of refractory metals, oxides or carbon by resistance heating, high-frequency induction heating, or electron beam evaporation. The evaporated atoms travel through reduced background pressure in the evaporation chamber and condense on the growth surface. The deposition rate or flux is a function of the travel distance from the source to the substrate, the angle of impingement onto the substrate surface, the substrate temperature T_s , and the base pressure. The conventional thermal evaporation system is mentioned in Figure II.5 [8, 9].

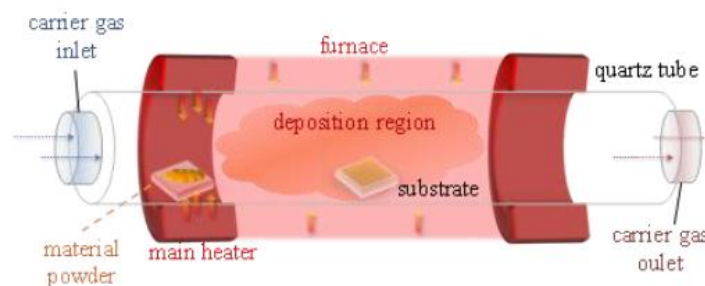


Figure II.5: Schematic diagram of Thermal evaporation system [7]

2.7 Chemical method of deposition

Chemical deposition processes are the most significant techniques for the growth of films owing to their versatility for depositing a very large number of elements and

compounds at relatively low temperatures. The processes are very economical and have been industrially exploited to a large scale.

2.7.1 Chemical Vapor Deposition

Chemical vapor deposition (CVD) is the condensation of chemical compounds from the gas phase onto a substrate where the reaction occurs to produce a solid deposit. The gaseous compound, bearing the deposited material, if not already the vapor state is formed by volatilization from either a liquid or a solid feed and is caused either to flow by a differential of pressure or by the achievement of gas transported into the substrate.

The chemical reaction is started approximately to the surface of the substrate which produces the desired material. In some processes, the chemical reaction may be activated through an external agency such as an application of heat, RF field, light or X-rays, an electric arc or glow discharge, electron bombardment etc. The microstructure, morphology, and adhesion of the deposit are greatly related to the activation process and the nature of the chemical reaction [7].

2.7.2 Chemical bath deposition

The chemical bath deposition (CBD) is also recognized as controlled precipitation; it has been applied since to deposit films of many different semiconductors. It is currently attracting great attention as it does not necessitate sophisticated instrumentation like vacuum system and other expensive equipment. All that is required is a vessel to include the solution (an aqueous solution made up of a few usually common, chemicals) and a substrate on which deposition is required. It offers a bottom-up approach to prepare nanocrystalline materials in thin film form with better particle size controlled, particle shape, size distribution, particle composition, the degree of particle agglomeration, the conventional thermal evaporation system is presented in Figure II.6 [10].

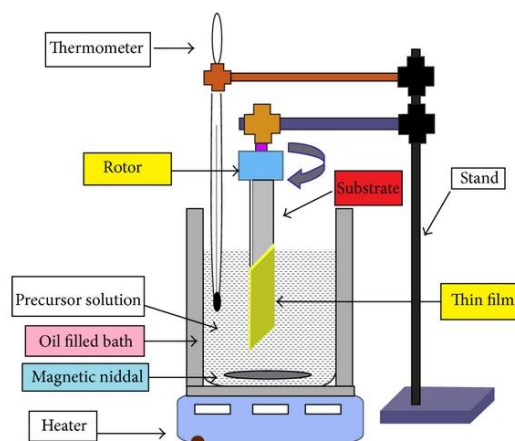


Figure II.6: Schematic diagram of Chemical bath deposition system [10]

2.7.3 Electrodeposition

The appearance of chemical changes due to the transition of electric current via an electrolyte is named electrolysis and the deposition of any substance on an electrode as a consequence of electrolysis is called electrodeposition as mentioned in Figure II.7. This phenomenon is dominated by the two following laws, first enunciated by Faraday in 1833: (i) the magnitude of chemical change occurring is relative to the electric current passed and (ii) the masses of different kinds deposited at or dissolved from electrodes in the similar quantity of electricity are in direct proportion to equivalent weights. The two laws can be united and expressed mathematically as:

$$W = \frac{IEt}{F} \quad (\text{II. 1})$$

Where W is the mass (in g) of the deposited material, I is the current (in A), E is the chemical equivalent weight (in g), and t is the reaction time (in s). F constant called the Faraday, equivalent to 96500 C and is defined as the quantity of charge necessary to deposit one equivalent of any ion from a solution [11].

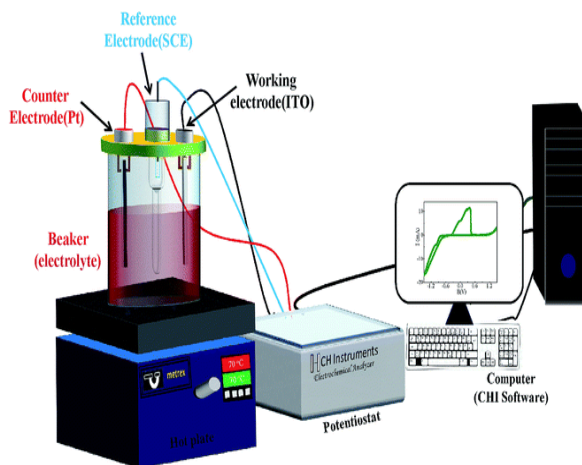


Figure II.7: Schematic diagram of Electrodeposition system [12]

2.7.4 Sol-gel technique

The sol-gel process is one of the mainly useful solution deposition methods of thin films. 'Sol' includes metal salts or metal alkoxides as precursors (starting material) and their appropriate solvents. Moreover, the sol may contain some functional additives like stabilizers that chemically improve the sol homogeneity. The liquid-filled solid network called 'gel' is originated by the linking of colloidal particles with one another in 3D structure. The transformation from sol to gel is most commonly provoked by changing the pH value of the sol via catalysts such as acids and bases. The catalysts initiate the sol to gel transformation by affecting the overall hydrolysis and condensation rates.

As a result, characteristic of gel, such as the structure of the chains or groups, appropriate time for gelation. Sol-gel offers a low-temperature route for the production of complex/functional oxide structures and deposition of sol onto complex-shaped or large surfaces. It has several chemical and physical steps which are hydrolysis, condensation, drying, and densification. It is possible to fabricate high purity products such as micro and nanoparticles in different size/shape, fibers, membranes, powders and coatings by a sol-gel process. The schematic summary of this technique is given in Figure II.8. This technique is promising with its low cost, simple equipment requirement and scalability [13].

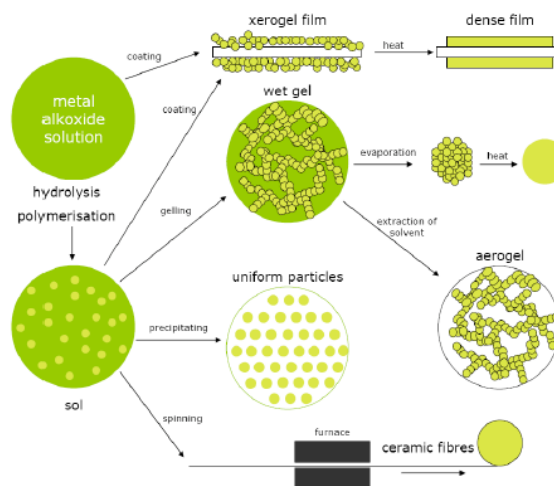


Figure II.8: Schematic summary of the sol-gel process [14]

2.8 Spray pyrolysis technique (SPT)

2.8.1 Introduction

In 1966, Chamberlin and Skarman for the first time used spray pyrolysis technique (SPT) for the preparation of CdS thin layers and application in a solar cell. SPT is a process to elaborate dense and porous oxide films, ceramic coatings, and powders. Compared with

other film deposition techniques, SPT represents a very simple and relatively cost-effective method, especially regarding equipment cost. SPT does not necessitate high-quality substrates or chemicals. This method has been used for the deposition of dense films, porous films, and for powder production. Even multilayer films can easily be elaborated using this versatile technique. SPT has been used for several decades in the glass industry and in solar cell production to deposit electrically conducting electrodes [15].

2.8.2 Principle

The deposition of film from the spray pyrolysis method requires heated substrate in order to spray the metal salt from the aqueous solution. Droplets were scattered and formed disk-shaped structure into the surface of the substrate and undergo thermal decomposition. The size and shape of the disk correlated with substrate temperature, the volume, and momentum of the droplet. Consequently, this film was produced and included overlapping disks of metal salt being changed to metal oxide. Some types of spray pyrolysis devices are developed to exploit the capability of the technique coupled with the properties of the solution precursors. The change in atomization method resulted in different spray pyrolysis techniques. They are [15]:

- Pressurized air blast (liquid is exposed to a stream of air).
- Ultrasonic wavelengths were produced and are required for fine atomization.
- Electrostatic (liquid interacts with the existence of high electric field).

Out of all these, pressurized air blast spray deposition is the most simple and cost-effective. The spray parameters can be very well controlled. The fundamental of spray pyrolysis components is spray nozzle, a rotor for a spray nozzle, liquid level monitor, hot plate, gas regulator valve and air compressor as it mentioned in (Figure II.9).

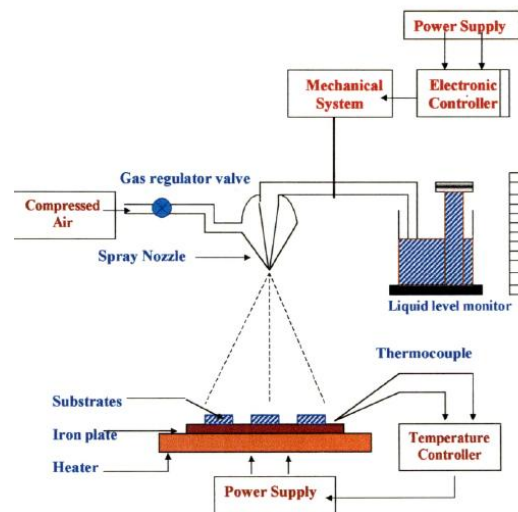


Figure II.9: Schematic diagram of Spray pyrolysis system [16]

2.8.3 Scheme of pyrolysis and formation of thin films

In spray pyrolysis, the experimental parameters such as precursor solution, decomposition of the precursor, atomization, and aerosol transport are very significant in order to examine the structural, compositional, surface topology, electrical and optical properties of the thin films. Several of these parameters are investigated in the following section.

2.8.3.1 Precursor solution

Precursor solution shows as the main important parameter in the production of thin films from different compounds. Aqueous solutions are typically used due to low cost, the simplicity of handling and existence in the wide range of water-soluble metal salts. The solute must have high solubility, for maximum yield. Alcoholic and organic solutions have been applied to synthesize the organic materials of non-oxide ceramic solutions [1].

2.8.3.2 Atomization of precursor solution

The critical operation of the spray pyrolysis method is to produce homogeneous surface and silky droplets by thermal decomposition. A different atomization methods such as; pneumatic, ultrasonic and electrostatic have been applied for solution aerosol formation. Some of spray atomization methods like electrostatic spray pyrolysis, microprocessor-based spray pyrolysis, radiance spray pyrolysis, ultrasonic nebulized atomization technique etc are also being used. These previous atomizers types vary in velocity of a droplet, size of droplet and rate of atomization. The size of the droplets was produced with pneumatic or pressure nozzles decrease when a difference of the pressure across the nuclei is increased [1].

2.8.3.3 Decomposition of precursor

When a droplet strikes on the surface of the substrate the processes like evaporation of the residual solvent, spreading of the droplets and salt decomposition takes place. Many models exist for demonstrating the decomposition of a precursor. Various steps during pyrolysis of aerosols are as explained below (Figure II.10) [1].

- In the primary step, an aqueous precursor solution is converted into aerosols (droplets) by spray nozzle and the solvent evaporation takes place.
- In this step, the solvent is vaporized which induce the formation of precipitate as the droplets approach the substrate.
- When the precipitate arrives at the substrate, nucleation and the growth of thin films on the substrate take place.

- The final step, the growth of the nuclei which accompanied to the production of the continuous thin film layer.

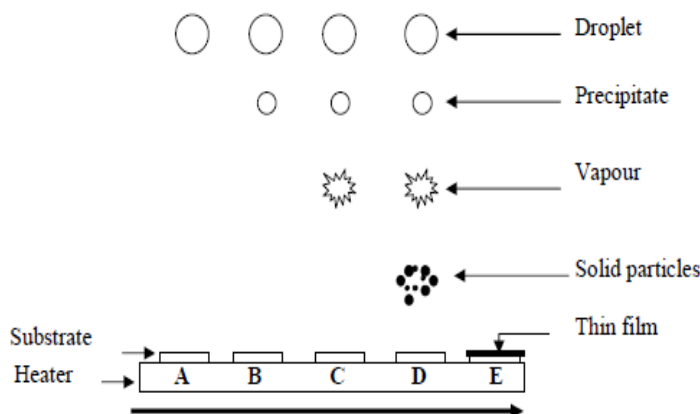


Figure II.10: Mechanism of thin films formation by Spray pyrolysis method [16]

2.9 Factors governing the formation of thin film using spray pyrolysis technique

They exist several factors acting to the film formation mechanism which depends on;

- The automation of the spray solution into a spray of fine droplets, which respect to the spraying nozzle geometry and pressure of a carrier gas.
- The properties of deposited films are greatly related to the substrate temperature, solvent evaporation, droplet size, carrier gas, ambient atmosphere, spray rate, and also on the cooling time after deposition .
- However, the film thickness which is associated with solution concentration, the distance separated the substrate and nozzle, and substrate temperature [17] .

2.10 Merit of spray pyrolysis technique

- It offers a simple way to deposit films with just about any component in any proportion by simply adding it in some type to the spray resolution.
- Compared to closed CVD method, spray pyrolysis method doesn't need prime quality targets and/or substrates nor will it need a vacuum at any stage, that feasible a good benefit if the technique is to be scooped up for industrial applications.
- From the spray parameters, the thickness of the films and the deposition rate is easily controlled, therefore eliminating the main drawback of chemical ways like sol-gel that produces films of restricted thickness.
- This method operates at averaged temperatures ranged in 200-600 degree Celsius.

- It doesn't cause native heating that may be damaging the materials to be deposited. Practically there are no limitations on the substrate material, dimension or its surface profile [17].

2.11 Thin Film Characterization Techniques

2.11.1 Thickness measurement

2.11.1.1 Weight difference method

The most common and important factor is the film thickness in the investigation of the sample properties. Different techniques were used for estimating the film thickness, the weight difference method is simple and convenient and thickness t is measured using the relation (II. 2):

$$t = \frac{\Delta m}{\rho \cdot A} \quad [\text{nm}] \quad (\text{II. 2})$$

where Δm is the mass difference between previous and next deposition on area A of the substrate and ρ is the density of the material in the bulk form. The mass m of the film was measured using microbalance [18].

2.11.1.2 Interference method

The optical interferometric technique was applied to measure the thickness of the as-deposited thin films. The transmittance spectrum shows maximum and minimum for the continuous scan of all the samples as shown in Figure II.11, suitable for optical interference inter film layer and surface f the substrate. The thickness t of the films can be determined from any two maxima (or two minima) using the relation:

$$t = \frac{M\lambda_1\lambda_2}{2(n_f(\lambda_1)\lambda_2 - n_f(\lambda_2)\lambda_1)} \quad (\text{II. 3})$$

where, M is the number of oscillations between two extrema occurring for λ_1 and λ_2 , $n_f(\lambda_1)$ and $n_f(\lambda_2)$ is corresponding refractive indices [18].

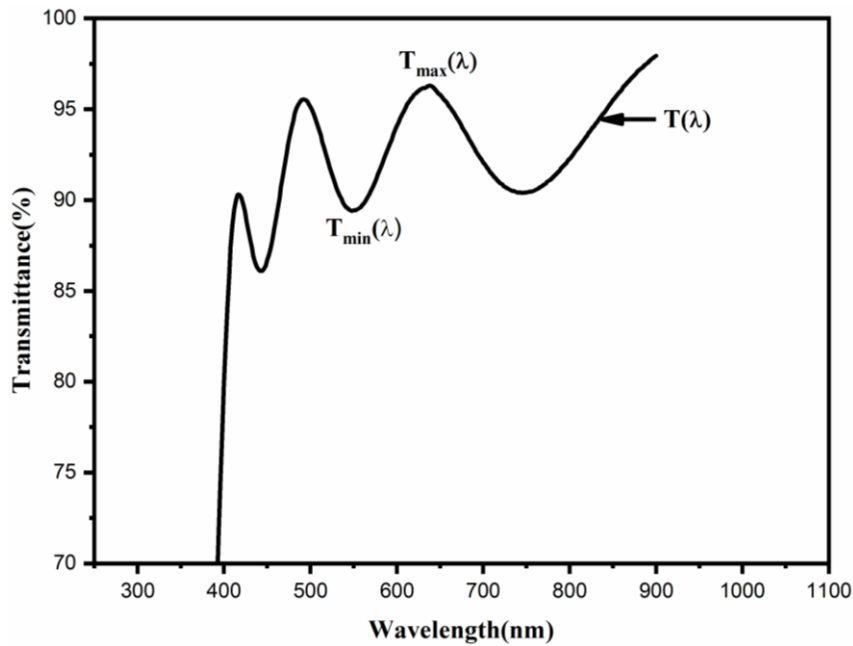


Figure II.11: Interference method for thickness measurement [18]

2.11.2 Structural characterization

2.11.2.1 X-ray diffraction (XRD)

X-ray diffractometer is a powerful system for the study of nanostructured films since it gives a more information such as crystal structure, composition, and defects in the films. It is a nondestructive technique and does not need any specific sample preparation methods; the schematic diagram of the device is represented in the Figure II.12. X-Ray diffraction is founded on the constructive interference of monochromatic X-rays caused by crystalline materials. The cathode ray tube is responsible to produce X-Rays and by a filtered to produce monochromatic radiation collimated to focus and directed across the sample. Crystals which can consider as the uniform arrangement of atoms; however X-rays can be treated as electromagnetic waves radiation. Atoms disperse X-ray waves, firstly through their electrons. X-ray striking an electron produces secondary spherical waves emanating from the electron. This physical phenomenon is well-known as elastic scattering, and the electron is known as the scatterer[19].

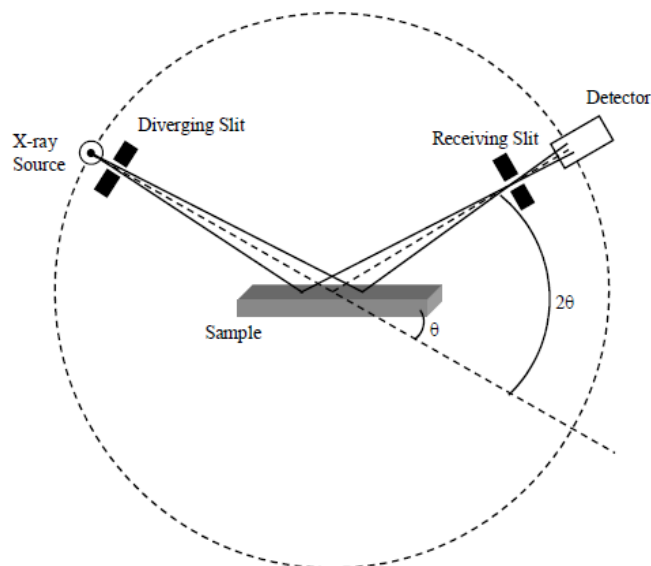


Figure II.12: Schematic diagram of X-ray diffractometer [19]

Over the destructive interference, X-ray waves eliminate one another out in most directions, in a few particular directions constructive wave was added, determined by Bragg's law :

$$2d\sin\theta = n\lambda \quad (\text{II. 4})$$

where θ is the angle incidence, λ is the wavelength of the beam, d is the spacing between diffracting planes and n is the order of diffraction. As seen in the Figure II.13, the beam of incidence causes each scatterer to re-radiate a small portion of its intensity as a spherical wave. In the case of scatterers are arranged uniformly with a d spacing, X-ray waves will superimpose constructively only in this directions. X-ray diffraction measurements of the films synthesized in this work are done using Bruker AXS-8 advance with Cu-K α radiation of wavelength 1.5406 Å adapted at 40 kV and 35 mA [19].

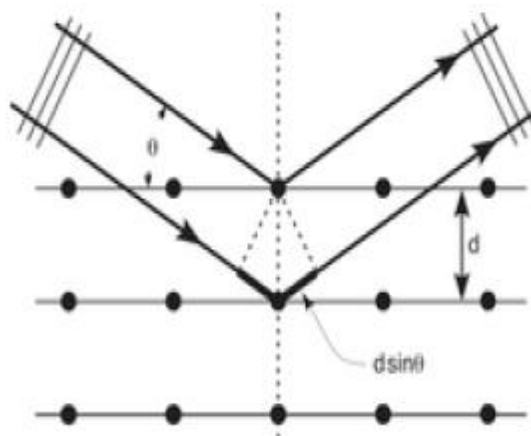


Figure II.13: Diffraction in crystals [19]

2.11.2.2 Identification of phases

Identification of phases can be obtained in the following way: The comparison of observed d -values with standard d -values from international American Standard for Testing of Materials (*ASTM*) standard data file or Joint Committee for Powder Diffraction Standards (*JCPDS*) data file, for the same material synthesized by the standard chemical method. This analysis reveals the different phases appear in the film and Miller indices of the atomic planes. The lattice parameters for the unit cell of the phase present are calculated using equations given by Bragg's law. The absence of reflection peaks indicates amorphous nature of the film [20].

2.11.2.3 Structural Parameters

2.11.2.3.1 Interplanar spacing

Interplanar spacing d was calculated from X-ray diffraction profiles using the formula:

$$2d \sin \theta = n\lambda \quad (\text{II. 5})$$

Using d values, the series of lattice planes ($h k l$) were identified from standard data. Strong peaks are expected when the condition of Bragg is satisfied. The lattice parameter values for different crystallographic systems can be determined from the following equations [21].

- For the cubic systems,

$$\frac{1}{d^2} = \frac{h^2 + k^2 + l^2}{a^2} \quad (\text{II. 6})$$

- For the tetragonal systems,

$$\frac{1}{d^2} = \frac{h^2 + k^2}{a^2} + \frac{l^2}{c^2} \quad (\text{II. 7})$$

- For the hexagonal systems,

$$\frac{1}{d^2} = \frac{4(h^2 + hk + k^2)}{3a^2} + \frac{l^2}{c^2} \quad (\text{II. 8})$$

- For the orthorhombic systems,

$$\frac{1}{d^2} = \frac{h^2}{a^2} + \frac{k^2}{b^2} + \frac{l^2}{c^2} \quad (\text{II. 9})$$

2.11.2.3.2 Crystallite size (Grain size)

The crystallite or grain size of samples can be established by the Scherrer formula;

$$D = \frac{0.9\lambda}{\beta \cos \theta} \quad [\text{nm}] \quad (\text{II. 10})$$

where D is the mean crystallite size, which supposedly equal or smaller to the grain size, Bragg angle θ in radians, β is the line broadening at half maximum intensity ($FWHM$) in radians and λ is the wavelength applied for X-ray of ($\lambda = 1.5406\text{\AA}$). [21].

2.11.2.3.3 The texture coefficient

The texture coefficient (TC) illustrates the texture (the distribution of crystallographic orientations of a polycrystalline sample) of the specific plane, deviation of which from unity reveals the preferred growth. About the preferential orientation quantitative information was effectuated from the different texture coefficient $TC(hkl)$ defined as [21]:

$$TC(hkl) = \frac{\frac{I(hkl)}{I_0(hkl)}}{\frac{1}{N} \sum \frac{I(hkl)}{I_0(hkl)}} \quad (\text{II. 11})$$

where $I(hkl)$ is the relative experimental intensity from (hkl) plane, $I_0(hkl)$ is the intensity of standard pattern from the JCPDS information and N is the reflection number.

2.11.2.3.4 Microstrain

The line varying experimental XRD patterns from that of the standard patterns indicate the strain developed throughout the synthesis of the films. Microstrain was computed by using equation (II. 12) [21]:

$$\varepsilon = \left(\frac{a - a_0}{a_0} \right) \times 100 \quad (\text{II. 12})$$

where ε is the mean strain, a is the calculated lattice constant thin films and a_0 the standard lattice constant of bulk material according to standard card (JCPDS).

2.11.2.3.5 Dislocation density

The defects quantity in the material was determined by calculating the dislocation density δ from the following formula [21]:

$$\delta = \frac{1}{D^2} \quad [\text{line/m}^2] \quad (\text{II. 13})$$

Where D is the crystallite size.

2.11.3 Surface characterization

2.11.3.1 Scanning electron microscopy (SEM)

SEM is a kind of microscope that form imagery the sample surface by scanning it with a high-energy beam of electrons in a raster scan pattern, the schematic diagram of SEM is presented from Figure II.14. It is a powerful microscope that uses electrons rather than light to form an image of objects such as fractured metal components, foreign particles and residues, polymers, thin films electronic components, biological samples, and countless others. The shorter wavelength of electrons permits image magnifications of up to 100,000X, as compared to about 2,000X for conventional light microscopy. An SEM also provides a greater profundity of field than a light microscope, allowing complex, three-dimensional objects to remain sharp and in focus [11].

In a typical SEM, an electron beam is thermionically emitted from an electron gun fitted with a tungsten filament cathode. The electron beam, which in general has an energy limited from an only some hundred electron volts to 40 keV, is concentrated using one or two condenser lenses to a spot about 0.4 nm to 5 nm in diameter. The beam proceeds through pairs of scanning coils or pairs of deviator plates in the electron column, typically in the final lens, which deviates the beam in the x and y-axes so that it scans in a raster mode through a rectangular region of the sample.

The size of the interaction volume relies on the electron's decline in energy, the atomic number of the sample and the sample's density. The energy swap between the sample and the electron beam outcome in the reflection of high-energy electrons by elastic scattering, emission of secondary electrons by inelastic scattering and the electromagnetic emission of, each of which can be checked using specific detectors.

The beam current absorbed through the sample can be captured and applied to generate imagery of the distribution from sample current. In order to increase the signals, electronic amplifiers are utilized which are exhibited as a change in brightness on a cathode ray tube. The raster scanning of the CRT display is coordinated with that of the beam on the sample in the microscope, and the resulting image is, therefore, a distribution plan of the signal intensity being emitted from the scanned surface of the sample. The image possibly catches by photography from a high-resolution cathode ray tube, but in modern machines is digitally captured and represented on a computer monitor [11].

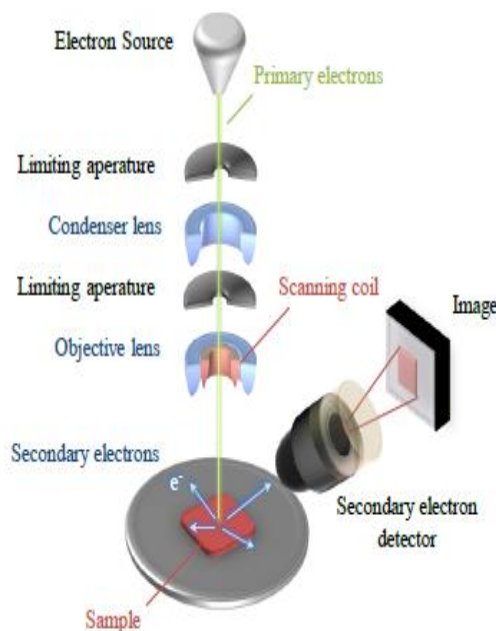


Figure II.14: Schematic diagram of SEM [7]

2.11.3.2 Energy dispersion X-Ray (EDX)

Energy Dispersive X-ray Spectroscopy (EDS or EDAX) is a technique for chemical microanalysis. The EDAX technique detects the emission of X-rays from the sample for the period of the bombardment by an electron beam to describe the chemical elemental composition of the film as it shown from Figure II.15. When the sample is bombarded with the electron, the electron ejected from the atoms comprising the sample's surface. The consequence, electron vacancies are filled by the electron from the higher state and an X-ray is emitted to balance these two energy states. That characteristics X-ray represents a particular elemental composition. The detector calculates the relative abundance of emitted X-rays as a function of energy. When an incident X-ray strikes the detector, a charge pulse was produced which is correlated to the X-ray energy. This charge pulse is transformed to a voltage pulse (which remains corresponding to the X-ray energy) by a charge sensitive preamplifier. The signal is then transferred to a multichannel analyzer where the pulses are sorted by voltage. The determination of the energy was performed from the voltage measurement, for each incident X-ray is expedited to a computer for display and further data evaluation. From the X-ray energy spectrum versus counts is estimated to recognize the chemical elemental of the sample [22].

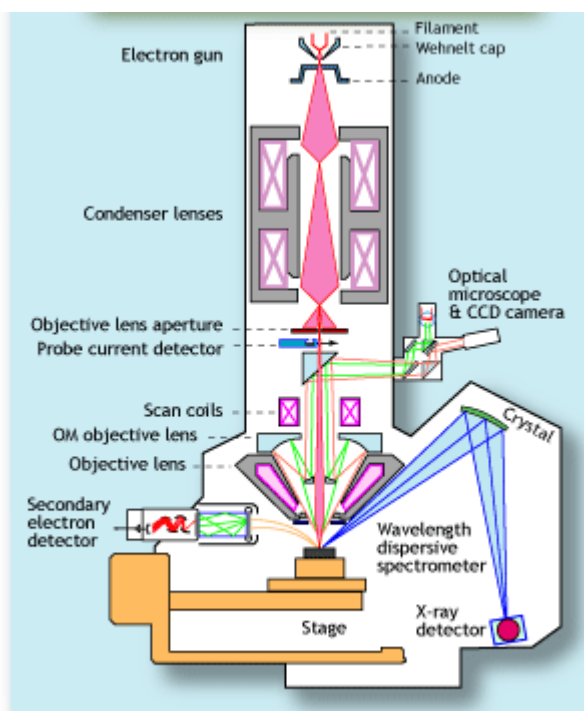


Figure II.15: Schematic diagram of Energy dispersion X-Ray (EDX) [23]

2.11.4 Optical characterization

2.11.4.1 UV-Vis-NIR Spectrophotometer

Spectrophotometers are optical devices that determine the light intensity of reflected or transmitted using objects with a variation of wavelength. Light throughout the lamp enters the monochromator, which makes the light dispersion and selects the particular wavelength chosen by the operator for the measurement. After that, the chosen wavelength is moved alternately throughout the sample and along the reference path. The reference and sample light beams pass via the cell compartment, consisting of a reference space and a sample space. The two light beams converge on the detector. Transmittance or absorbance of solid or liquid and total diffuse reflectance/transmittance of solids like large disks, silicon wafers, plastics, glass etc. can be measured. Band gap determination, electron transition and enzyme activity studies can also be made [24].

A diagram of the typical constituent of the spectrophotometer is represented from the Figure II.16. By using diffraction grating or prism the beam of light (visible or/and UV light source) is divided, into its component wavelengths. By a half-mirrored device, every monochromatic beam is dividing into two equal intensity beams. One beam, the sample beam (colored magenta), proceed through a small transparent container (cuvette) comprise a transparent solvent or solid like thin films being studied. The further beam, the reference

(colored blue), carry on through the same cuvette including just the solvent. The intensities of these beams of light are then examined using electronic detectors and comparator.

The beam intensity (reference beam) defined as I_0 , which becomes small or no light absorption. However the beam intensity of the sample defined as I . Over a short period of time, automatically the spectrometer sweeps all the component wavelengths from the previous description. The ultraviolet (UV) portion is studied from 200 to 400 nm, and the visible section is ranged in 400-800 nm. If the sample does not absorb light of a given wavelength, $I=I_0$. Furthermore, if the sample absorbs light then I is less than I_0 , and this variation may be plotted on a graph versus wavelength. Absorption was displayed as transmittance ($T = I/I_0$) or absorbance ($A = \log I_0/I$). If no existence of absorption so $T = 1.0$ and $A = 0$ [24].

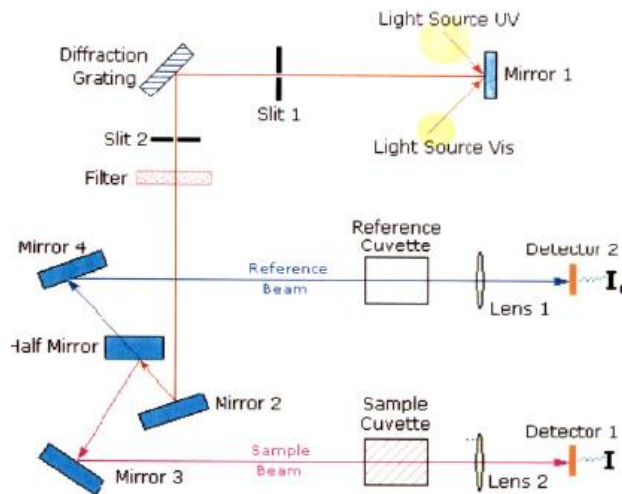


Figure II.16: Schematic diagram of UV-Vis-NIR Spectrophotometer [24]

2.11.4 .2 Absorption coefficient

An electronic transition between the conduction and valence bands in the crystal starts at absorption edge which equals to the least energy variation between the highest maximum of the valence band and the lowest minimum of the conduction band. If these extrema lie at the similar point of the k-space then the transition is called direct. If this is not, then only phonon assisted transitions called indirect transitions are possible as depicted in Figure II.17. Optical absorption of materials is directly allied with the coefficient of absorption α . It is crucial to determine the absorption characteristics of glasses and thin films, especially when comes to optical materials is subject to exploit their applications possibilities. When light is incident on thin films some of its energy is reflected, some is absorbed and rest is transmitted.

The optical absorption in thin films depends on thickness and wavelength and is a function of its structural properties. From the transmission spectra, the coefficient of absorption values was established by the Beer-Lambert Law [25]:

$$\alpha = \frac{1}{t} \ln\left(\frac{1}{T}\right) \quad (\text{II. 14})$$

where T is the transmittance and t is the sample thickness. The reliance of absorption coefficient on photon energy in the high absorption regions is achieved to get more information concerning gap energy.

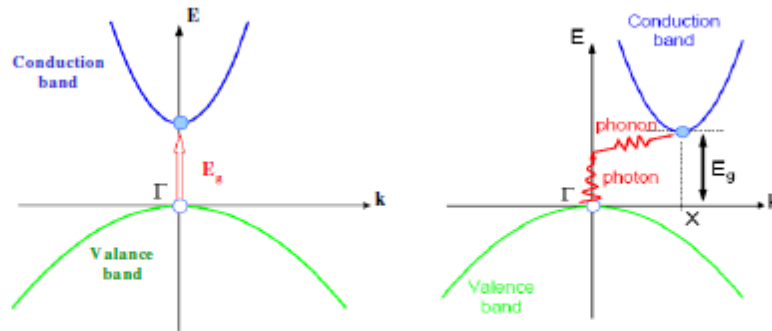


Figure II.17: E-K diagram showing (a) direct band and (b) indirect band transition [26]

2.11.4 .3 Optical band gap energy

The optical gap energy is one of the fundamental characteristics of optical materials. The measurement of gap energy relies not only on the material but also on its characteristics and stoichiometry. The energy limited to the highest maximum of the band of valence the and lowest minimum of the band of conduction is known as band gap energy (E_g). By determination of the absorption coefficient values, E_g value can be evaluated by the Tauc's formula [25]:

$$(\alpha h\nu) = B(h\nu - E_g)^n \quad (\text{II. 15})$$

where B is a constant which does not correlate to the photon energy, α is the absorption coefficient, $(h\nu)$ is the photon energy and n is an index that indicates the optical absorption mechanism and it is equivalent to 3, 2, 3/2, and 1/2 when the transition is indirect forbidden, indirect allowed, direct forbidden and direct allowed, respectively.

Direct band gap was evaluated using extrapolating the straight-line portion $(\alpha h\nu)^2$ vs $(h\nu)$ to the energy axis at zero absorption coefficient ($\alpha=0$) as observed from Figure II.18 [25].

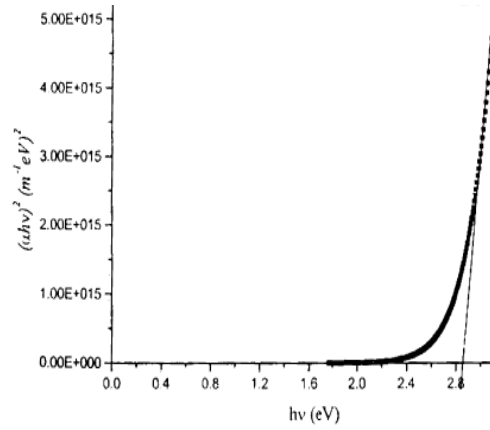


Figure II.18: $(\alpha hv)^2$ vs (hv) plot for determining direct energy band gap

2.11.4 .4 Urbach Energy

Generally, in optical absorption, close band edges, an electron from the top of the valence band get excited into the bottom of the conduction band across the energy band gap. During this transition process, if these electrons happen disorder, it causes the density of their states $\rho(h\nu)$, where $h\nu$ is the photon energy, tailing into the energy gap. This tail of $\rho(h\nu)$ extending into the gap energy is termed as Urbach tail as shown in Figure II.19. Consequently, absorption coefficient $\alpha(h\nu)$ also tails off in an exponential mode and the energy-related with this tail is referred to as Urbach energy and can be calculated by the following equation [27]:

$$\alpha(h\nu) = \alpha_0 \exp\left(\frac{h\nu}{E_u}\right) \quad (\text{II. 16})$$

where α_0 is a constant, $h\nu$ is the photon energy and E_u is the Urbach energy. The E_u energy is determined using the plotting $\ln(\alpha)$ vs. $h\nu$ and fitting the linear part of the curve with a straight line. From the linear region of reciprocal of the slope give up the E_u value. The E_u values of the samples, which decreases in the case of crystallization at higher temperatures. Because Urbach energy of glassy semiconductors fundamentally defines the disorder level, crystallization and resulted order of this process decrease the E_u in value [27].

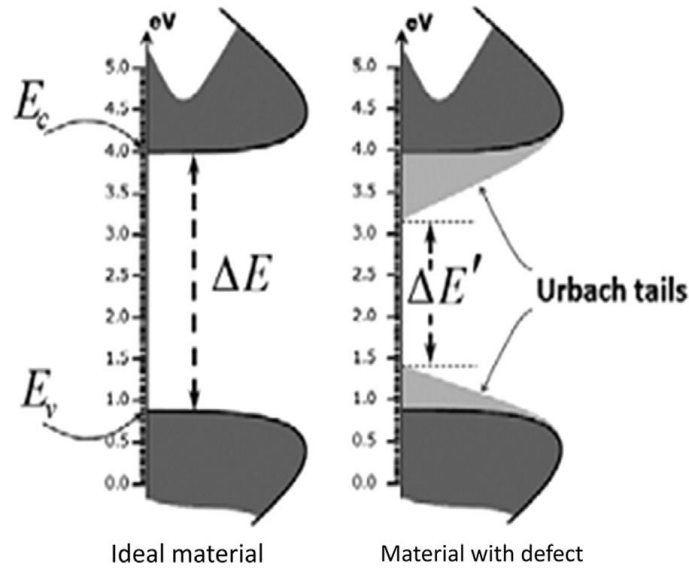


Figure II.19: Basic schematic of the spread of density of states in the band gap energy [28]

2.11.4 .5 Optical Constants

Optical constants of a material are one of powerful important its included refractive index and extinction coefficient, which generally correlated to the wavelength of the electromagnetic wave, through a relationship called dispersion. In materials where an electromagnetic wave, can lose its energy during its propagation, the index refraction becomes complex [29]. If a sample has a thickness t , an absorption coefficient α and reflectance R , the boundary between vacuum (or air) and an absorbing layer specified by refractive index (n), the extinction coefficient (k) and thickness (t) at normal incidence, yields the reflectance in terms of the optical constants of layer as [30]:

$$R = \frac{(n-1)^2 + k^2}{(n+1)^2 + k^2} \quad (\text{II. 17})$$

In the case of semiconductors and insulators, or materials in the range of frequencies in which absorption is weak, $k^2 \ll (n-1)^2$ so that equation (II.17) reduces to:

$$R = \frac{(n-1)^2}{(n+1)^2} \quad (\text{II. 18})$$

Hence

$$n = \frac{1 + \sqrt{R}}{1 - \sqrt{R}} \quad (\text{II. 19})$$

Therefore, to estimate n for any particular wavelength, the reflectance at that wavelength is determined for normal incidence only and n can be evaluated. The absorption coefficient α can be defined with reference to extinction coefficient k as [32]:

$$\alpha = \frac{4\pi k}{\lambda} \Rightarrow k = \frac{\alpha \lambda}{4\pi} \quad (\text{II. 20})$$

where k is known as the extinction coefficient (k) or attenuation constant and it can be estimated.

2.11.5 Fourier transforms infrared spectroscopy (FTIR)

Electromagnetic radiations in which wavelength extend in the range of 1micron to 1 mm are termed as infrared, which lie between the visible and microwave region. Usually, the wavelength used in IR spectroscopy ranged in 2.5-25 micron or 4000 to 400 wave number (waves per cm). FTIR is one of the most powerful analytical techniques, which offers to die prediction of chemical identification. It provides helpful information concerning the molecule structure. The technique is founded upon the simple fact that a chemical material shows famous selective absorption in the IR region, a diagram of the components of a typical spectrophotometer as shown in Figure II.20.

After absorption of IR radiations, the molecule of a chemical substance vibrates at many vibration modes, offering rise to close-packed absorption bands, named an IR absorption spectrum. Band intensities in the IR spectrum may be mentioned either as transmittance (T) or absorption (A). Various bands will appear in IR spectrum, which will correspond to the characteristic functional groups and bonds present in a chemical substance is a fingerprint for its identification. A molecule absorbs radiation when the fundamental frequency of vibration (stretching or bending) of some part of a molecule (i.e. atoms or a group of atoms composing it) is the same as the frequency of the incident radiation. Studies of the relation between structure and electromagnetic response of material are useful in understanding their properties. The bands in the region $300\text{-}700\text{ cm}^{-1}$ are matching to the fundamental vibration of the ions of the crystal lattice [31].

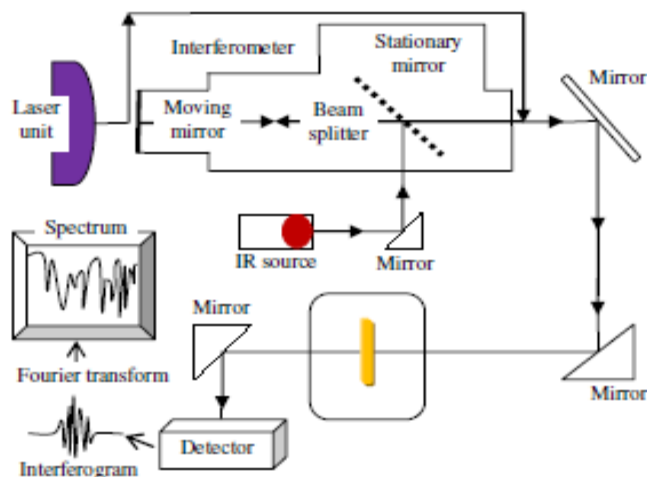


Figure II.20: Schematic diagram of FTIR Spectrophotometer [32]

2.11.6 Photoluminescence (PL) Spectroscopy

If a light particle (photon) has energy superior to the gap energy, then it can be absorbed so that raising an electron from the valence band (VB) jump to the conduction band (CB) across the band gap energy as shown from Figure II.21. In this mechanism of photoexcitation, the electron normally has excess energy, which it loses before coming to rest at the minimum energy in the (CB). In this case, the electrons eventually plunge down to the (VB). The energy it loses is converted back into a luminescent photon, which is emitted from the material. Thus the energy of the emitted photon is precisely equivalent to the gap energy, E_g . The mechanism of photon excitation continued by the emission of a photon is known as photoluminescence. Photo-excitation causes electrons inside the material to move into allowed excited states. When these electrons return to their equilibrium state, the excess energy is released; this may comprise the emission of light (a radiative process) or may not (a nonradiative process) [33].

Photoluminescence process correlated to the difference in energy levels between the two electron states included in the transition between the excited state and the equilibrium state. Radiative transitions in material also comprise localized defect levels. The photoluminescence energy affiliated with these levels can be exploited to know detail about the defects and the amount of photoluminescence can be performed to estimate their concentration. [33].

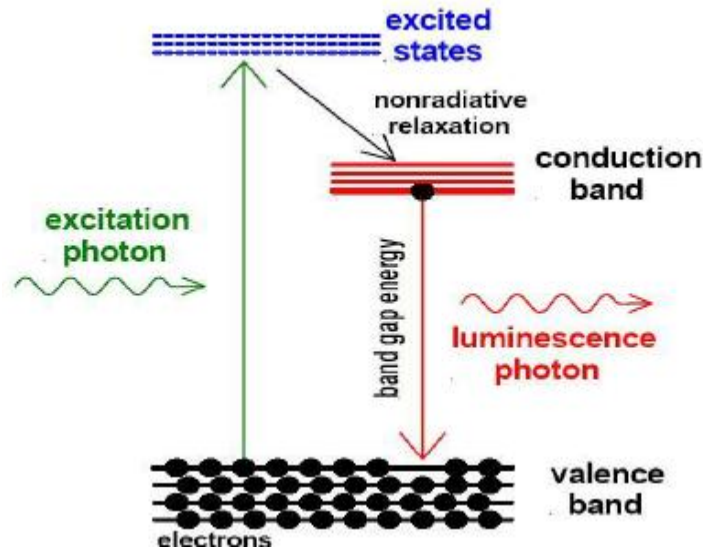


Figure II.21: Energy level diagram [33]

2.11.7 Electrical Characterization

Electrical characterizations are the greatest powerful techniques existing for materials characterization. Basic electrical characterization of a semiconducting thin film includes determining the conduction nature, conductivity and the mobility and carrier concentration of the films. The natures of conduction of the samples were examined using the hot probe method. The conductivity (or resistivity) of the films were investigated using four-probe technique however the mobility and the carrier concentration were evaluated by the Hall measurements.

2.11.7.1 Conduction nature of Films (Seebeck Measurement)

Seebeck measurement, also recognized as thermoelectric probe method, is used to confirm the conductivity type of materials by generating a gradient of temperature over a sample surface from the hot to the cold probes. Thermal gradients produce currents in a semiconductor; the majority carrier currents for n- or p-type semiconductor are given by equation (II.21) [34]:

$$J_n = -qn\mu_n P_n \frac{dT}{dx}, J_p = -qp\mu_p P_p \frac{dT}{dx} \quad (\text{II.21})$$

where μ_n and μ_p are the charge carrier mobility n- and p-type materials respectively, $P_n < 0$ and $P_p > 0$ are the differential thermoelectric power.

The extrinsic semiconductors are n-type or p-type materials mainly differ in nature by their majority carriers, for the former it is holes and for the later it is electrons. For n-type semiconductors, the current flows opposite to the drift direction of the electrons. But for the

p-type materials, the current goes from the path of the holes. It is facile to prove the nature of conduction of the films if the electrons path flow is measured. Hot probe technique is method utilized to find the path of electrons flow which is often recognized as the thermoelectric probe method. The hot probe arrangement for *n*-type semiconductors is depicted in Figure II.22. The semiconductor is located on a metal plate (also films deposited on either conducting substrates or non-conducting substrates) and a heated metal is attached to the metal base through a multimeter. The other end of the metal base, which is linked to the multimeter, is named the cold junction and the hot tip is the hot junction. When the semiconductor is briefly touched with the hot probe, the current flows from the cold junction to the hot junction for *n*-type semiconductor and for the *p*-type, current flows from the hot to the cold junction. *N*-type conductivity is invariably observed [35, 36].



Figure II.22. Hot probe technique for measuring Conduction nature of thin Film

2.11.7.2 Linear four probe technique

A materials conductivity σ , (or the inverse property, resistivity ρ , where $\rho=1/\sigma$) correspondent to its capability to conduct electricity. In case of semiconductor materials, the conductivity is insured with the carrier mobilities and the number of available charge carriers (electrons or holes). Different mechanisms for conductivity existed and its reliance on temperature also differs. In the semiconductors, it is reported that with increasing temperature the conductivity increases (more carriers are generated); however in the metals the conductivity decreases as increasing the temperature (more scattering by the lattice). Furthermore, the conductivity is also linked with a crystalline structure. The crystal type and orientation affect conductivity because the electronic structure is typically attached to the crystal structure. In polycrystalline materials, the crystallites size (grains) is also essential parameter as it affects the scattering of carriers and, at very small sizes may also affect the electronic structure. The method used to determine conductivity depends on whether the material is a bulk sample or a thin film [37].

Four point probe measurements are used to characterize the resistivity of a bulk or thin film sample. By utilizing a four probe set-up the resistivity measured belongs to the film only and not being affected by the contact point which would have been the case for a setup with just two electrodes. Figure II.23 shows the set-up for a four-point probe measurement. A current, I , is sent through the sample and the voltage V , is measured as shown Figure II.23. The specific resistivity for the sample can then be calculated. For the calculations, some assumptions have to be made. The metal tip is infinitesimal and samples are semi-infinite in the lateral dimension. For bulk samples where the sample thickness $t \gg s$, the probe spacing,

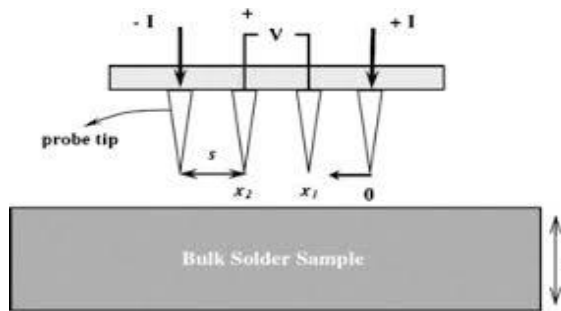


Figure II.23: Schematic of four point probe configuration [37]

It is considerate that a spherical protrusion of current emanates from the outer probe tips. The differential resistance R is presented using equation (II.22):

$$\Delta R = \rho \frac{dx}{A} \quad (\text{II. 22})$$

where ρ is the specific resistivity, A indicates a general area. In the case of a thin film where t is much smaller than s , the current through the sample can be viewed as rings. The area can be expressed as equation (II.23) [37]:

$$A = 2\pi xt \quad (\text{II. 23})$$

The resistivity of the sample is then calculated from equation (II.22), which gives the equation (II.24):

$$R = \int_{x_1}^{x_2} \rho \frac{dx}{2\pi xt} = \int_s^{2s} \frac{\rho}{2\pi t} \frac{dx}{x} = \left[\frac{\rho}{2\pi t} \ln(x) \right]_s^{2s} = \frac{\rho}{2\pi t} \ln 2 \quad (\text{II. 24})$$

by using Ohm's law, $R=V/I$, expression (II.24) can be generalized to equation (II.25) giving the specific resistivity (in $\Omega \cdot \text{cm}$) of the film.

$$\rho = \frac{t\pi}{\ln 2} \left(\frac{V}{I} \right) = R_{sh} \cdot t \quad (\text{II. 25})$$

$$R_{sh} = \frac{\pi}{\ln 2} \left(\frac{V}{I} \right) = \frac{\pi}{\ln 2} \cdot R = 4.532 \cdot R$$

where R_{sh} is the sheet resistance of film is independent of the film dimensions.

2.11.7.3 Hall Effect measurements

When a material is located in a magnetic field and his direction vertical to the current flow, a field or voltage is created across the specimen in the direction vertical together with the magnetic and electric field, a field is termed the Hall field or Hall voltage was produced. This field increase under the effect of the force of Lorentz which deviate holes and electrons in the normal direction to both the magnetic and electric fields and his direction are being opposite. Thus the magnitude and sign of Hall voltage facilitate the determination of the nature and density of the majority carrier dominant in the films respectively. The schematic representation of the Hall-Effect measurement is shown in the Figure II.24 [38].

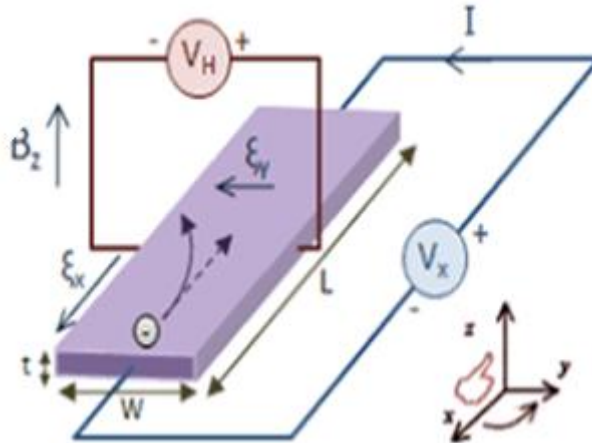


Figure II.24: Schematic diagram of Hall Effect measurements [39]

If the sample with resistivity ρ , width w , and thickness t are positioned in the magnetic field B then the Hall voltage V_H is created vertical to both the current and magnetic field, the Hall coefficient R_H can be defined using:

$$R_H = \left(\frac{V_H}{I} \right) \times \frac{t}{B} \quad (\text{II. 26})$$

The mobility μ (cm^2/Vs), a measure of how easily a carrier moves in material, is given by:

$$\mu = \frac{R_H}{\rho} \quad (\text{II. 27})$$

where, R_H is the hall coefficient. The carrier concentration n (cm^{-3}) as a function of the mobility and resistivity can be derived using:

$$n = \frac{1}{q \cdot \rho \cdot \mu} \quad (\text{II. 28})$$

where q is the charge in coulomb.

References

- [1] A. K. Bhosale, spray deposition and characterization of cerium oxide, cerium oxide-silica and cerium oxide-zirconia thin films for optically passive counter electrodes in electrochromic device, PhD thesis, Shivaji University, Kolhapur, 2009.
- [2] S. Senroy, characterization of copper oxide, titanium oxide and copper doped titanium oxide thin films prepared by spray pyrolysis technique, PhD thesis, Bangladesh University, 2016.
- [3] M. Nesa, characterization of zinc doped copper oxide thin films synthesized by spray pyrolysis technique, master memoir, Bangladesh University, 2016.
- [4] <https://slideplayer.com/slide/10325361/>.
- [5] A. Khan, Synthèse de Cuprates de Strontium (SrCu_2O) par MOCVD comme couche mince d'oxyde transparent conducteur de type P, PhD thesis, Grenoble University, 2006.
- [6] D. K. Avasthi, Electronic sputtering of thin films, PhD thesis, Jawaharlal Nehru University, 2001.
- [7] M. Hanif Yaacob, Investigation of Metal Oxide Nanostructured Thin Films Based Optical Hydrogen Sensors, PhD thesis, RMIT University, 2012.
- [8] A. Sakthi velu, preparation and characterization of SILAR deposited ZnO thin films for gas sensor applications, PhD thesis, Bharathidasan University, 2009.
- [9] B. Purusottam reddy, investigations on RF sputter deposited copper oxide thin films for supercapacitor and sensor applications, PhD thesis, Venkateswara University, 2015.
- [10] S. M. Pawar, B. S. Pawar, J. H. Kim, O.S. Joo, C.D. Lokhande, Recent status of chemical bath deposited metal chalcogenide and metal oxide thin films, *Current Applied Physics*, 11(2) (2011) 117–161.
- [11] M. Sharmin, characterization of boron doped zinc oxide thin films prepared by spray pyrolysis deposition technique, Master of philosophy in physics, Bangladesh University, 2015.
- [12] Suchitra Yadav, B.S. Yadav, S. Chaudhary, D.K. Pandya, Deposition potential controlled structural and thermoelectric behavior of electrodeposited CoSb_3 thin films, *RSC Adv.*, 7 (2017) 20336-20344.
- [13] B. E. Saraç, structural and optoelectronic properties of sol-gel derived nickel oxide thin films, PhD thesis, Middle East technical University, 2017.
- [14] <http://www.chemat.com/chematechnology/SolGel.html> (2009).
- [15] S. Pawar, synthesis and characterization of $\text{Sm}_{0.5}\text{Sr}_{0.5}\text{CoO}_3$ films for solid oxide fuel cell application, PhD thesis, Shivaji University Kolhapur, 2011.
- [16] M. A. Mahadik, , Degradation of organic impurities in water using nanocrystalline ferric oxide semiconductor thin films, PhD thesis, Shivaji University, 2014.
- [17] K. M. Jadhav, Structural electrical optical and magnetic properties of some ferrite thin film prepared by spray pyrolysis technique, PhD thesis, Babasaheb Ambedkar Marathwada University, 2017.

- [18] S. Chigare, preparation of tin oxide thin films by spray pyrolysis technique and their electrochromic properties, PhD thesis, Shivaji university, Kolhapur, 2003.
- [19] L. Chinnappa, investigation of the effects of certain crucial process parameters on the solar cell related optical and electrical properties of doped tin oxide films fabricated using a low cost spray technique, PhD thesis, Bharathidasan University, 2012.
- [20] N. M. Pinto Neves, Al-doped ZnO ceramic sputtering targets based on nanocrystalline powders produced by emulsion detonation synthesis – deposition and application as a transparent conductive oxide material, PhD thesis, Nova Liboa University, 2015.
- [21] A J. Ragina, Preparation and characterization of tin based semiconducting thin films, PhD thesis, Kannur University, 2012.
- [22] A. Ghosh, growth and effect of Shi irradiation on structural and opto-electrical properties of nanocrystalline pure and doped zinc oxide semiconductor thin film for gas sensor application, PhD thesis, Babasaheb ambedkar Marathwada University, 2010.
- [23] <http://www.mcswiggen.com/TechNotes/WDSvsEDS.htm>
- [24] S A. Vanalakar, chemical synthesis of cds, ZnO and CdS sensitized ZnO thin films and their characterization for photo-electrochemical solar cells, PhD thesis, Shivaji University, Kolhapur, 2010.
- [25] P. Sharma, an optical study of chalcogenide glasses using Uv-Visible-Nir spectroscopy, PhD thesis, Jaypee University, 20.15.
- [26] H. Pisal Sunanda, Studies on chemical routes for functionalization of carbon nanotubes and their physico chemical characterization, PhD thesis, Bharati Vidyapeeth Deemed University, 2015.
- [27] M. Rezvani, L. Farahinia, tructure and optical band gap study of transparent oxyfluoride glass-ceramics containing CaF₂ nanocrystals Materials & Design, 88 (2015) 252-257.
- [28] A. Loukil, A. Boukhachem, M. Ben Amor, M. Ghamnia, K. Raouadi, Effects of potassium incorporation on the structural, optical, vibrational and electrical properties of NiO sprayed thin films for p-type optical windows, Ceramics International, 42 (2016) 8274-8289.
- [29] Tanvir Ahmmed, Investigation of Structural, Optical and Electrical Properties of Zinc Selenide Thin Films Prepared by Chemical Bath Deposition Technique, Master of Science, Bangladesh University, 2014.
- [30] J.R. Rathod, Investigations on the growth and characterization of ZnTe thin films deposited by SILAR method for possible window applications, PhD thesis, Sardar Patel University, 2014.
- [31] S.L. D. Kadam, studies on spray pyrolyzed cobalt oxide and nickel oxide thin films and their electrochromic properties, PhD thesis, Shivaji University, kolhapur, 2000.
- [32] Suresh Kumar, Structural, Morphological, Optical and Magnetic Properties of Pure and Transition Metal Doped Cadmium Sulphide Nanofilms at Room Temperature, PhD thesis, Jaypee University of Information Technology, Solan, 2014.
- [33] M. Hemalatha, synthesis, characterization and electrochemical applications of nickel, nickel oxide and fe-doped nickel oxide nanoparticles, PhD thesis, Anna University Chennai, 2014.
- [34] A. Kitai, Luminescent Materials and Applications, John Wiley & Sons, 2008.

[35] D. K. Schroder, Semiconductor Material and Device Characterization, 2nd edition (John Wiley & Sons, New York, 1998).

[36] K. jeyadheepan, preparation and characterization of Rf sputtered oxide thin films for devices, PhD thesis, Alagappa University, 2010.

[37] M. E. Alnes, Transparent Conducting Oxides by Atomic Layer Deposition, PhD thesis, University of Oslo, 2014.

[38] P.K. Jaysukhal, studies on electrochromic thin films devices and sensors, PhD thesis, Mahraja sayajerao University, 2012.

[39] https://en.wikipedia.org/wiki/File:Hall_Effect_Measurement_Setup_for_Electrons.png (2012).

Chapter III

Elaboration And Characterizations Of Undoped NiO Thin Films

3.1 Introduction

Spray pyrolysis technique (SPT) is simple, cheap and accessible for nano-material production. Furthermore, the SPT includes high deposition rates and makes it possible to coat large areas with non-planer geometries, which are desirable for industrial applications. The SPT will be chosen to elaborate the NiO thin films. The enhancement of the film properties prepared with SPT is largely correlated with the deposition conditions parameters, which affect the physical properties. Recently, numerous researchers were described to the influences of precursors, solution concentration, temperature, solvent nature, annealing treatment and film thickness on NiO films properties [1-6]. The effect of initial parameters such as solvents nature, precursor concentration and volume of the sprayed solution on structural, optical and electrical properties will be achieved out in this chapter.

3.2 Effect of solvents nature

Effects solvent nature is one of the important parameters for spray pyrolysis coating and has an effect on the properties of the deposited films. From literature, not many published work has been attracted on the effect of different solvents on NiO thin films properties. In this section, the impact of both the solvents on the structural, optical and electrical properties of NiO thin films is studied that were elaborated using low-cost spray pyrolysis method.

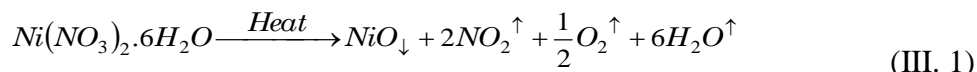
3.2.1 Experimental procedure

3.2.2 Films preparation

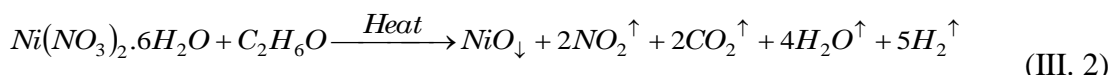
Nickel oxide thin films were prepared by spray pyrolysis method. Nickel nitrate [Ni(NO₃)₂.6H₂O] was used as the source of Ni. The starting solution was prepared by dissolving in 30 ml into three different solvents: methanol (CH₃OH), ethanol (C₂H₆O) and de-ionized water (H₂O). The concentration of nickel nitrate was 0.05M. The solution mixtures were stirred thoroughly by a magnetic stirrer for half an hour, leading to the formation of a clear green and homogeneous solution, and then it was sprayed on 500°C heated glass substrate. The distance between spray nozzle and substrate was fixed at 40 cm. The spray rate of 2 ml/min was maintained, each spray time took 10s and time interval between successive sprays was 10s. The substrates were (R217102) microscopic glass slide in size of (75 × 25 × 1.1 mm³). Before the deposition process, the glass substrates were cleaned with acetone, rinsed with de-ionized water and dried in air. After deposition, the films were allowed to cool slowly at room temperature.

The reaction mechanism can be checked as heat decomposition of nickel nitrates to nickel oxide with the company of water, temperature, and air. With different solvents used in this study (methanol, ethanol and de-ionized water) sprayed solution leading to NiO formation the following:

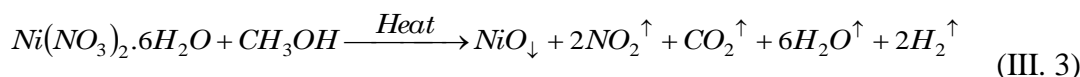
- Reaction of nickel nitrate with de-ionized water,



- Reaction of nickel nitrate with Ethanol,



- Reaction of nickel nitrate with Methanol,



3.2.3 Films characterization

The structural properties of prepared thin films were investigated using X-ray diffraction (BRUKER - AXS type D8) equipped with X'Pert High Score under Cu K α ($\lambda = 1.5406\text{\AA}$) radiation. The scanning range of (2θ) was taken between 20° and 70° . The optical transmission spectra were obtained using an UV-visible spectrophotometer (Shimadzu, Model 1800); the scanning measurements were ranged in 300-900nm. To affirm the nature of conductivity Seebeck effect were carried out. The electrical conductivity of the films was performed with Keithley Model 2400 low voltage source meter instrument. Film thickness was measured by using weight difference method considering the density of the bulk nickel oxide. All measurements were carried out at room temperature.

3.2.4 Result and discussions

3.2.4.1 Structural properties

Figure III.1 shows the XRD patterns of NiO thin films elaborated on a glass substrate at 500°C with different solvents. Three diffraction peaks were observed at $2\theta = 37.2^\circ$, 43.3° and 62.8° which can be attributed respectively to (111), (200) and (220) planes of NiO phase. This result approves that the NiO films are polycrystalline in nature and matched well to the face-centered cubic (FCC) crystalline structure of NiO. From the XRD analysis, no other phase or impurities were observed, which imply that the diffraction pattern affirms that the all samples are single phase. The obtained XRD spectra matched well with the joint committee

powder diffraction system (JCPDS, No.47-1049) under the space group $Fm3m$ (225) [7]. Furthermore, it can be observed that by varying solvent adapted in this work the intensity of NiO peaks reduces, indicating an improved crystalline character of the deposited films. It was also found from all the three solvents that the (111) peak has the highest intensity indicating the preferred orientation.

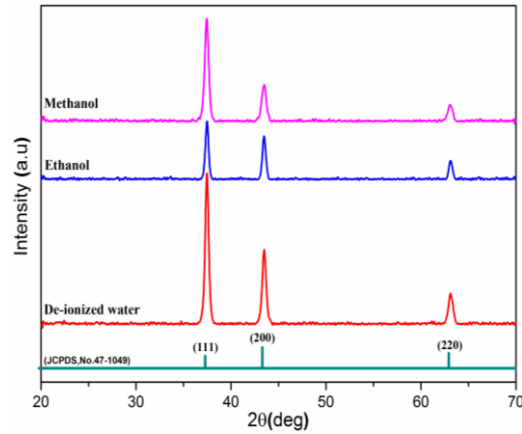


Figure III.1: XRD patterns of NiO films using different solvents.

Diverse structural parameters such as lattice constants, mean strain, and crystallite size of NiO films coated with a various solvents solution are summarized in Table III.1. It can be shown that the lattice parameter values from all obtained films are observed higher than to the bulk standard a_0 of NiO, this variation in lattice parameter corresponds to the existence of internal strain, defects and impurities in the films, similar results are also reported by other researchers [8]. From Table III.1, the crystallite size values were about 39, 22 and 29 nm for samples deposited by de-ionized water, ethanol and methanol solvent respectively. Talebian et al. reported that the variation in crystallite size values correlated directly to the polarities and viscosities of solvents used in this study [8].

Solvent	2θ (deg)	Lattice constant (\AA)		Crystallite size D (nm)	Mean strain ϵ (%)
		a	$\Delta a = a - a_0$		
De-ionized water	37.267	4.2629	0.0860	39	2.060
Ethanol	37.347	4.2717	0.0948	22	2.271
Methanol	37.314	4.2681	0.0912	29	2.185

Table III.1: Values of Bragg angle (2θ), lattice constants (a), crystallite size (D) and mean strain (ϵ) for the (111) plane of NiO thin films using different solvents.

Furthermore, it is seen from Figure III.2 that the crystallite size contrary proportional to mean strain, this may be attributed to the increment of the defects and empty spaces in the crystalline structure as crystallite size decreases. The film grown with de-ionized solvent is found to have a good value of crystallite size and a minimum value of compared to the other

solvents, as shown in Figure III.2. It can be noticed that the film with the best structural properties has smallest mean strain value, which effects in the crystallization level [9].

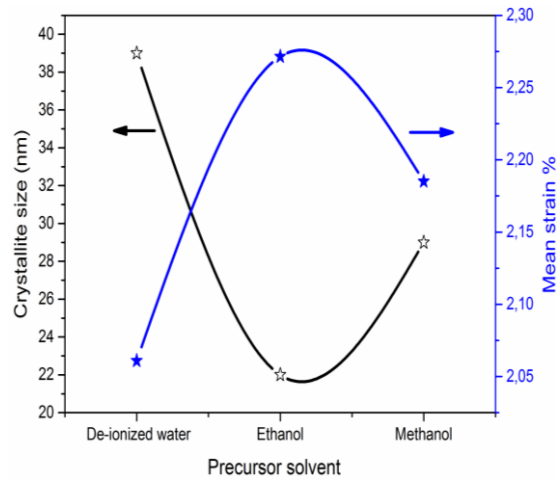


Figure III.2: Variation of crystallite size and mean strain of NiO thin films using different solvents.

3.2.4.2 Optical properties

Figure III.3 shows the transmittance spectra of the sprayed NiO thin films prepared at 500°C with various solvents recorded in the wavelength ranged from 300 to 900 nm. All the obtained films illustrate good transparency in the visible region. The average transmission value is over than 84 % for the film elaborated with de-ionized water solvent and then decrease to reach the value of 82 % for the film prepared with ethanol solvent; however, the film deposited with methanol exhibit an average optical transparency about 71%. This decreasing in the optical transmittance may be referred to the increase in the film thickness given by Lambert's law and photon scattering in the layers. Strong absorption has been observed between 300-370nm, corresponding to the onset fundamental absorption edge of NiO due to the transition between the valence band and the conduction band, as shown in Figure III.3. These results show that the produced NiO thin films could be used in transparent electronics due to the low absorbance in the visible region [10, 11].

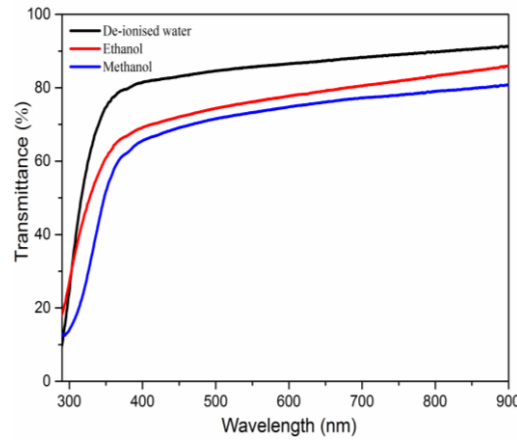


Figure III.3: Transmittance spectra of NiO thin films using different solvents.

The absorption coefficient α can be calculated from the transmittance T values and thickness t at the absorption edge of Lambert's law [12]:

$$\alpha = \frac{1}{t} \ln \left(\frac{1}{T} \right) \quad (\text{III. 4})$$

The optical band gap energy E_g of the films can be estimated from the transmission spectra using the following relation, known as the Tauc's relation [13]:

$$\alpha h\nu = A(h\nu - E_g)^{\frac{1}{2}} \quad (\text{III. 5})$$

where A is a constant, α is the absorption coefficient, $h\nu$ is the photon energy and E_g is the band gap energy. For directly allowed transitions the optical band gap can be obtained from the plot of $(\alpha h\nu)^2$ versus $h\nu$. Extrapolating the linear portion of the graph with energy axis gives the band gap, as shown in Figure III.4. The obtained values are listed in Table III. 2.

Solvent	Thickness t (nm)	Optical gap energy E_g (eV)	Urbach energy E_u (meV)	Conductivity σ ($\Omega^{-1}\cdot\text{cm}^{-1}$) $\times 10^{-2}$
De-ionized water	116	3.58	384.02	39.5
Ethanol	204	3.61	343.52	20.8
Methanol	253	3.65	324.44	13.4

Table III.2: Values of thickness (t), optical band gap energy (E_g), Urbach energy (E_u) and conductivity (σ) of NiO thin films using different solvents.

As can be seen that E_g values are in the range 3.58 - 3.65eV obtained by; de-ionized water, ethanol, and methanol solution respectively. These results are very close to the E_g of intrinsic NiO and are in good agreement with the literature reports [14, 15]. Variation in the E_g values may be related to existence of defects or vacancies in the NiO material and can also affect by variation of solvents solution.

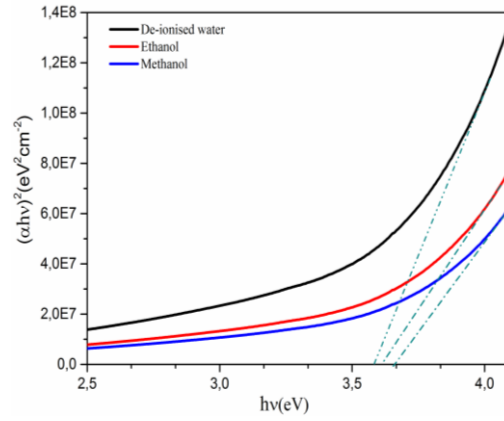


Figure III.4: Estimation of band gap energy (E_g) from Tauc's relation of NiO thin films using different solvents.

The Urbach tail of the films can be determined by the following relation [16]:

$$\alpha = \alpha_0 \exp\left(\frac{h\nu}{E_u}\right) \quad (\text{III. 6})$$

where α_0 is a constant, $h\nu$ is the photon energy and E_u is the Urbach energy which refers to the width of the exponential absorption edge. E_u values can be determined from the plot of $\ln(\alpha)$ versus ($h\nu$) and its straight line slopes, as shown in the Figure III.5.

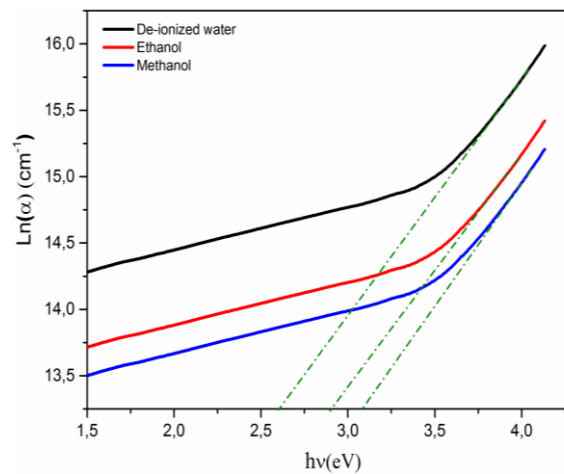


Figure III.5: Estimation of urbach energy (E_u) of NiO thin films using different solvents.

The evaluated E_u values are given in Table III.2. As can be seen, the E_u values decreases from 384.02 to 324.44 meV with a variation of solvents nature. This decreasing is attributed to the decrease of defects, which is related to the disorder in the film due to the creation of new localized energy states near the band edges [17, 18]. Furthermore, the E_u values change inversely with the optical band gap of NiO films, as observed in the Figure III.6.

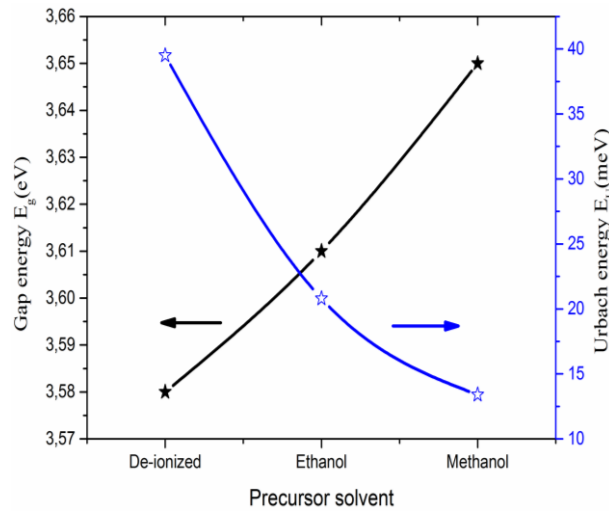


Figure III.6: Variation of band gap energy (E_g) and Urbach energy (E_u) of NiO thin films using different solvents.

3.2.4.3 Electrical properties

To find out the conductivity nature of the NiO films, hot probe method (Seebeck effect) was examined. A positive sign confirms the p-type conductivity of the deposited samples was observed. The electrical property of deposited films was achieved by the four probe measurement. The conductivity values obtained for NiO films at different solvents and are represented in Table III.2. As can be seen, the conductivity of the film is found to be in the range $13.4\text{-}39.5 \times 10^{-2} \Omega^{-1}\text{cm}^{-1}$. We can observe the highest value of the conductivity from the film prepared using de-ionized water solvent; however, the conductivity decreases for the NiO films deposited using ethanol and methanol solvent. This could be attributed to the microstructural defects and impurities existing in the NiO structure, such as nickel vacancies and oxygen interstitial defects [18, 19]. Non-stoichiometric of NiO material recognized as a p-type semiconductor. Holes conductivity caused by Ni^{2+} ion vacancies through replacement with Ni^{3+} ions which act as electron acceptors [20]. Figure III.7 shows the electrical conductivity σ and film thickness t with different precursor solvents. The electrical conductivity is seen to decrease as the film thickness is increased from 116 to 253 nm. According to the previous studies, the electrical properties of NiO films also have a strong dependence with the film thickness [21-24].

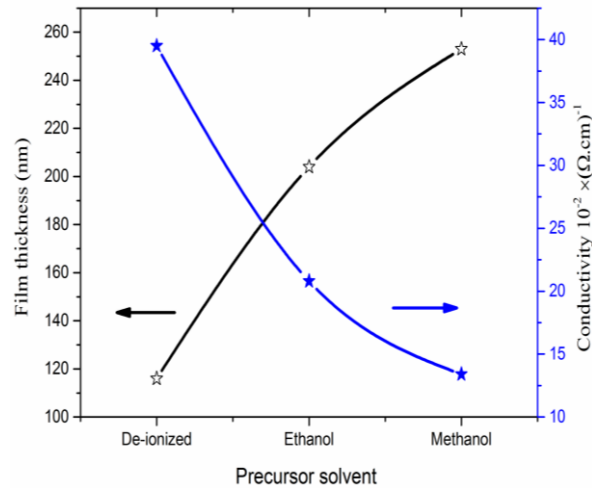


Figure III.7: Variation of Conductivity (σ) and film thickness (t) of NiO thin films using different solvents.

3.3 Effect of Precursor Concentration

In order to get better physical properties of NiO thin films elaborated with (SP) method. Precursor concentration has an essential parameter to get films with good quality. In this section, undoped nickel oxide (NiO) thin films were elaborated using (SP) method. Effects of precursor concentration on the structural and optical and electrical properties of NiO thin films are reported. It is noticed that this study is a collective work done from the members of the VTRS laboratory of El Oued University.

3.3.1 Experimental procedure

3.3.2 Films preparation

NiO thin films were prepared from solution of nickel nitrate hexahydrate $[\text{Ni}(\text{NO}_3)_2 \cdot 6\text{H}_2\text{O}]$. The precursor was dissolved in double distilled water with adding few drops of nitric acid (HNO_3) as a stabilizer. The precursor concentration, which served as a starting solution, was varied from 0.015 to 0.1M. The resulting solution was stirred at room temperature using a magnetic stirrer for half an hour to yield a clear and transparent solution. The obtained blend was used as a stock solution for spray pyrolysis. Microscopic glass slides (Ref 217102 with dimensions of $75 \times 25 \times 1.1 \text{mm}^3$) were used as substrates. The later were cleaned with alcohol in an ultrasonic bath and distilled water then blow dried with dry air. The heating temperature of the substrates was fixed at 500°C , the nozzle-substrate distance was kept 45 cm, the spray rate was 2ml/min, and each spray takes one second, whereas the time interval between two successive sprays was 10 second to avoid the substrate temperature fall. Different concentrated solutions of fixed volume (40 ml) were sprayed separately on

heated glass substrates leading to undoped NiO thin films. After deposition, the films were allowed to cool till room temperature.

3.3.3 Films characterization

Structural characterizations are carried out using X-ray diffraction (XRD) with an X-ray diffractometer (BRUKER-AXS type D8) equipped with X'Pert High Score under Cu $K\alpha$ ($\lambda = 1.5406\text{\AA}$) radiation whereas the scanning range of (2θ) was between 30° and 55° . Bonding information was obtained by Fourier transformed infrared (FT-IR) spectroscopy apparatus (Shimadzu IR-Infinity1); the scan of the measurements ranged from 400 to 4000 cm^{-1} . Optical transmittance of the deposited thin films was measured in the range of 300–900 nm by using an UV-visible spectrophotometer (SHUMATZU 1800). To affirm the p-type conductivity and its variation with precursor concentration, Seebeck effect, and four-point probe were processed on sheets having $2\times 1\text{cm}^2$ for all the samples. The measurement of the thickness t was done by gravimetric weight difference method, by assuming a constant density of NiO as 6.7 gm/cm^3 . All measurements were carried out at room temperature.

3.3.4 Result and discussions

3.3.4.1 Structural properties

X-ray diffraction (XRD) patterns of NiO thin films elaborated by the spray pyrolysis were recorded for different precursor concentration as 0.015, 0.03, 0.04, 0.05, and 0.1M and shown in Figure III.8. The as-deposited thin film at 0.015M shows an amorphous structure in nature; it indicates the poor crystallinity of the film. This may be due to the incomplete formation of the NiO film at this concentration. With increasing of precursor concentration from 0.03 to 0.05 M, the commencement of crystallization was observed. It is seen from XRD patterns that only single peak appears at $2\theta = 37.24^\circ$, which is attributed to the (111) diffraction peak and clearly indicated that the NiO phase exists under its face-centered cubic (FCC) structure, which is in good agreement with Joint Committee on Powder Diffraction Standards (JCPDS card number 47-1049) [25]. From XRD patterns, with respect to limit detection, no other impurity peaks were detected. The thin film that can be seen, deposited at 0.1M, has higher and sharper (111) diffraction peak indicating an improvement in crystallization of this film compared to other ones deposited at lower concentrations. It is worth noting that other peaks at (200) appeared in films when the concentration of solution exceeds 0.03 M.

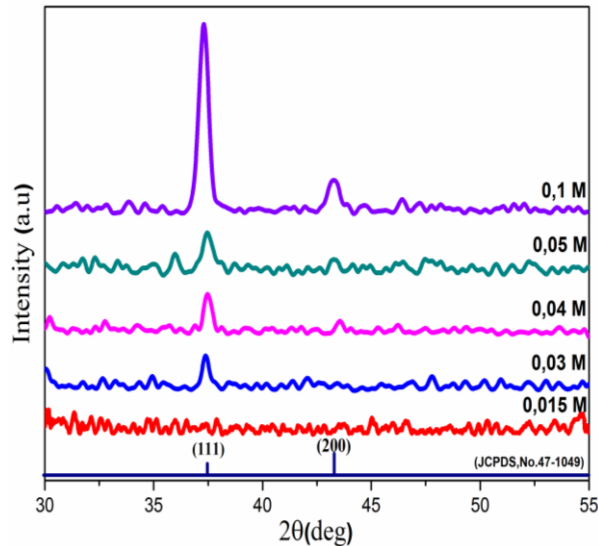


Figure III.8: X-ray patterns of NiO thin films prepared at 500°C with different of precursor concentration.

In order to obtain more structural information, different structural parameters such as lattice constants a , interplanar spacing d_{hkl} , grain size D , mean strain ε , and dislocation density δ of NiO thin films coated on various precursor concentration are calculated using the previous equations (Table III.3 summarizes variations of different structural parameters of elaborated NiO thin films with various precursor concentrations).

Precursor concentration (M)	2θ (deg)	Lattice constants (\AA)	β (deg)	D (nm)	ε (%)	$\delta \times 10^{15}$ (lines /m ²)
0.015	-	-	-	-	-	-
0.03	37.396	4.160	0.576	15.207	-0.397	4.323
0.04	37.377	4.163	0.432	20.275	-0.313	2.432
0.05	37.496	4.153	0.472	18.552	-0.562	2.905
0.1	37,392	4,165	0,236	37,085	-0,284	2.471

Table III.3: Values of Bragg angle 2θ , lattice constants a , full width at half maximum β , grain size G , mean strain ε and dislocation density δ for the (111) plane of NiO thin films prepared at 500°C with different of precursor concentration.

Variation of grain size along the (111) plan as a function of precursor concentration is reported in Figure III.9. As can be seen from this figure when precursor concentration covers the average 0.03 - 0.1 M, the grain sizes of the thin films were about 15.20, 20.27, 18.55, and 37.08 nm for samples deposited using 0.03 M, 0.04 M, 0.05, and 0.1 M, respectively. The film prepared at 0.1M concentration presents the high value of grain size (37.08 nm) revealing the nanostructure of the product. The increase in the grain size indicates a decrease

in the lattice defects, which in turn reduces internal strain and dislocation density [26] as it was seen in Table III.3.

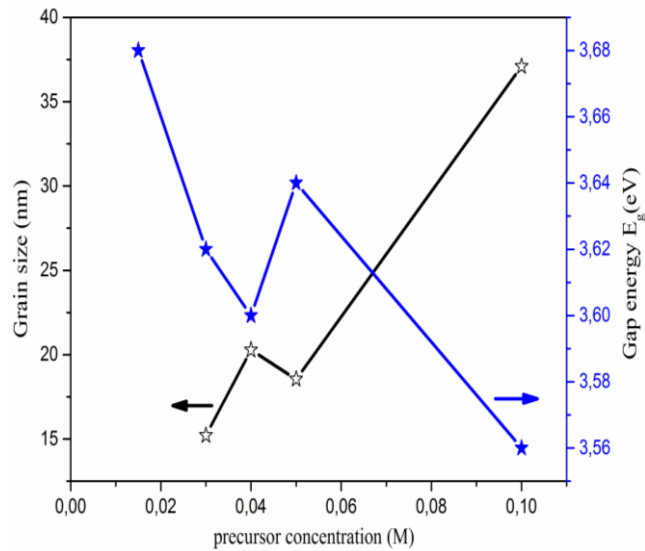


Figure III.9: Variations of grain size and band gap (E_g) of NiO thin films as function of precursor concentration prepared at 500°C.

3.3.4.2 Fourier Transform Infrared (FT-IR) Analysis

To further support the XRD results, the quality and composition of elaborated NiO thin films were investigated by FT-IR spectroscopy. Analysis through FT-IR spectroscopy was done because its spectra are a powerful tool to provide information on the nature of obtained metal oxides. In general oxides and hydroxides of metal, nanoparticles give absorptions peaks in wave number region below 1000 cm^{-1} that arise from inter-atomic vibrations [27-29]. Figures III.10 (a)-4(e) show the FT-IR spectrum of NiO thin films with varying precursor concentration from 0.015 to 0.1 M, respectively. As indicated in the spectra, for all samples characteristics peaks at 407,437, 475, 500, 520, 560, 607, 668, and 820 cm^{-1} correspond to Ni-O stretching vibration bonds as reported in the literature [30- 32] but with use of others deposition methods. Table III.4 summarizes obtained results in this study in agreement with other results carried out in the literature [25, 27, 31–51]. To give confirmation to the observed 820 cm^{-1} absorption strength vibration, in the case of 0.05 and 0.1M sprayed sample (Figures III.10 (d) and 4(e)), calculated wave number (in cm^{-1} as units) using Hook's law in simple harmonic oscillator model was done. As well known, Hook's law is illustrated by the following formula [52]:

$$\nu = \frac{1}{2\pi c} \sqrt{\frac{k}{\mu}} \quad (\text{III. 7})$$

where c is the speed of sound, k is the bond force constant, and μ is the reduced mass. Thus the position of specific band absorption of nickel oxide powders is determined on the basis of

the bond force constant k ($= 5 \times 10^5$ dyne \cdot cm $^{-1}$) and the reduced mass μ ($\mu = 1/m_{Ni} + 1/m_O$). This formula yields to theoretical NiO stretching vibration equal to 821 cm $^{-1}$ which is closely equal to the observed 0.05 and 0.1M sprayed samples, as seen in Figures III.10(d) and 4(e), and corresponds to the bulk Ni-O vibration mode.

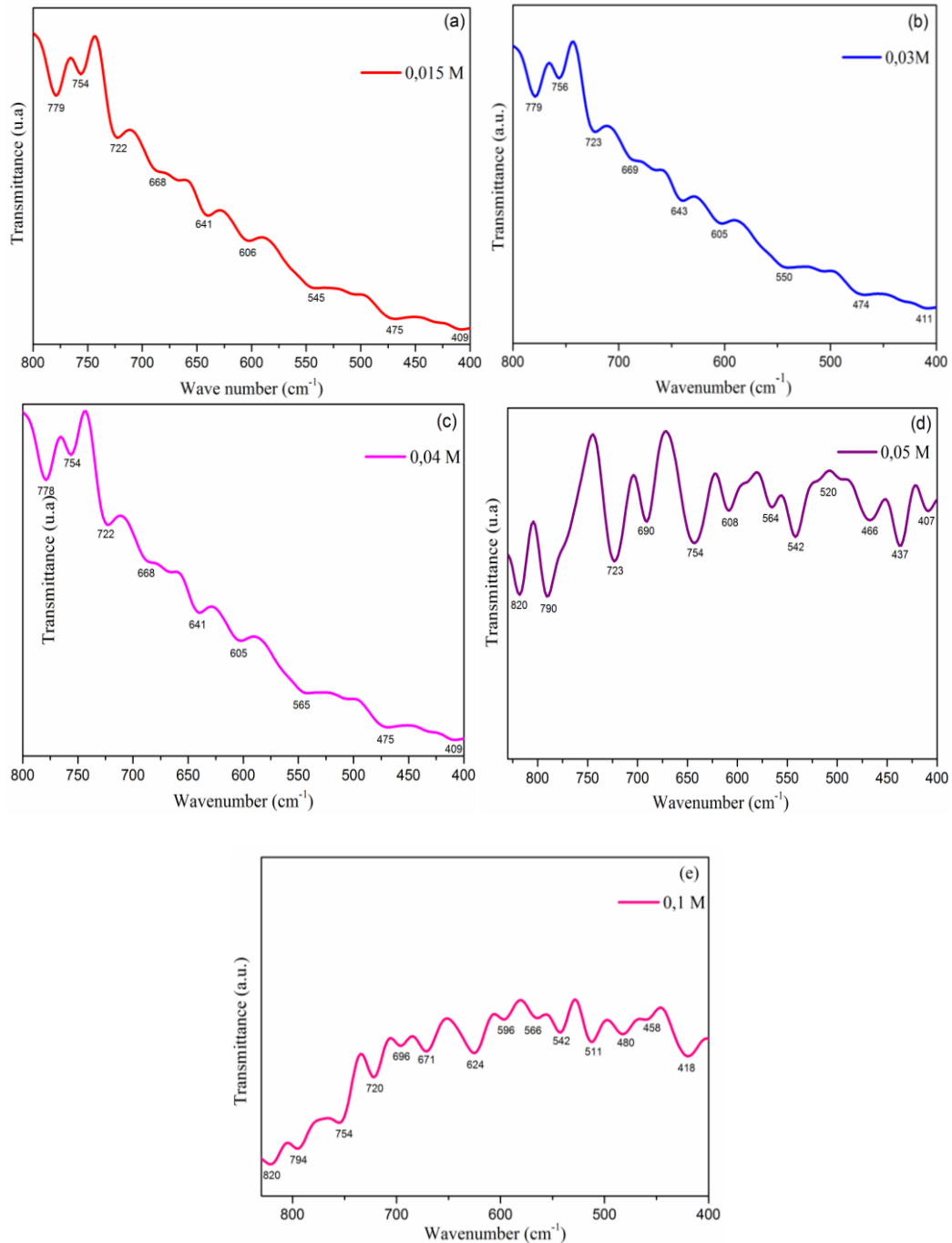


Figure III.10: FT-IR spectra of NiO thin films prepared at 500°C with different precursor concentration, (d, e) samples prepared with 0.05 and 0.1 M, (a, b, c) with 0.015, 0.03, and 0.04M.

Samples	Positions (cm ⁻¹) in this work in respect to the concentration	Assignments	Positions (cm ⁻¹) in other works
0.015, 0.03 and 0.04M	(409),(411), (412)	Nickel-oxygen interaction	410 [33, 34]
	(575), (474)	Ni-O stretching vibration	474.5-475 [30-36]
	(545), (550), (556)	bands metal- oxygen vibrations-stretching	450-550 [27], 450-560 [37], 552 [31]
	(6050), (606)	Ni-O-H stretching band	607-619 [32,38]
	(643-669),(641-668),(641)	Ni-O stretching vibration	600-700 [39], 660 [40], 663 [41]
	(779-756-726), (778-754-722),	Mode bending modes O-M-O	400-820 [31], 400-850 [42]
0.05 and 0.1M	(407), (418)	Nickel-oxygen interaction	410, 413 [33, 34,43]
	(437), (437)	Ni-O Absorption band	435.93 - 437 [30-44]
	(466-542-564), (558-480)	Bond stretching vibration Ni-O	450-560 [37], 460 [45], 445-490 [46], 470[33, 47]
	(511),(-)	Bending modes O-M-O	400-500 [48]
	(520), (520)	Nickel-oxygen stretch	520-520-524 [49-51]
	(-), (566-596)	vibrations Ni-O bond	660 [39], 663 [40]
	(608-690),(624-696-671)	band Ni-O-H stretching Bending between Ni and O	607 [32], 600-700 [39], 624[31]
(723-790-820), (720-754-794-820)	Mode bending modes O-M-O	400-820 [31], 400-850 [42]	

Table III. 4: The assignments of the most important bands in the FT-IR spectra of NiO thin films sprayed at 500°C with different of precursor concentration.

3.3.4.3 Optical properties

Figure III.11 shows the optical transmittance spectra recorded in the wavelength range 300-900 nm. For all thin films prepared at various precursor concentrations, spectra show two regions: the first one at wavelength higher than 400 nm showing practically an average transmission between 57% and 88% and revealing a decrease by increasing the precursor concentrations and, based on calculated film thickness (t), transparency was found to be depending on thickness of samples revealing Beer-Lambert law as it was shown in Table III.5. The second region is at the wavelength lower than 400nm for which transparency decreases rapidly for all samples exhibiting the onset fundamental absorption due to the transition between the valence band and the conduction band [53].

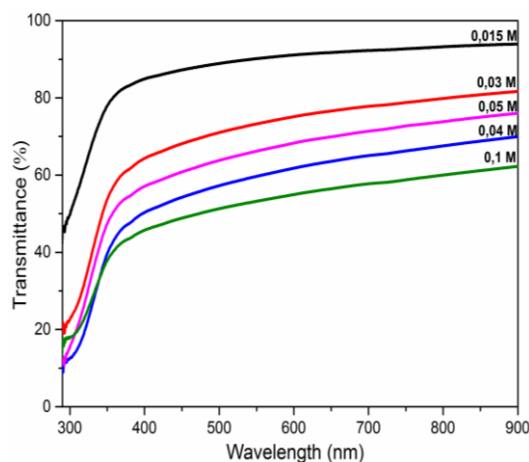


Figure III.11: Spectral transmittance plots of NiO thin films prepared at at 500°C with different of precursor concentration.

The calculated band gap values are listed in Table III.5. Obtained band gap values are in good agreement with results carried out in the literature [54, 55]. Also, the Urbach tails, which is related to the width of the localized states available in the optical band gap of the NiO thin films and affected its structure, was done for further investigation are calculated using the precedent equation.

Precursor concentration (M)	Thickness t(nm)	Average transmittance (%)	Gap energy E_g (eV)	Urbach energy E_u (meV)
0.015	181.57	88.30	3.68	309.40
0.03	191.66	71.01	3.62	365.76
0.04	170.36	57.56	3.60	394.36
0.05	190.34	64.28	3.64	400.16
0.1	200.00	51.66	3.56	453.72

Table III. 5: Values of thickness t, average transmittance, optical band gap energy E_g , and Urbach energy E_u of NiO thin films prepared at 500°C with different of precursor concentration.

Figure III.12 shows the variation of $\ln(\alpha)$ versus photon energy ($h\nu$) for the films. E_u values were calculated and illustrated in Table III.5. As can be seen from Table III.5, the energy band gap is averaged in 3.68-3.60 eV. The decrease in the optical band gap with precursor concentration may be attributed to the increase in grain size and a decrease in structural disorder in the films as observed from Urbach energy analysis.

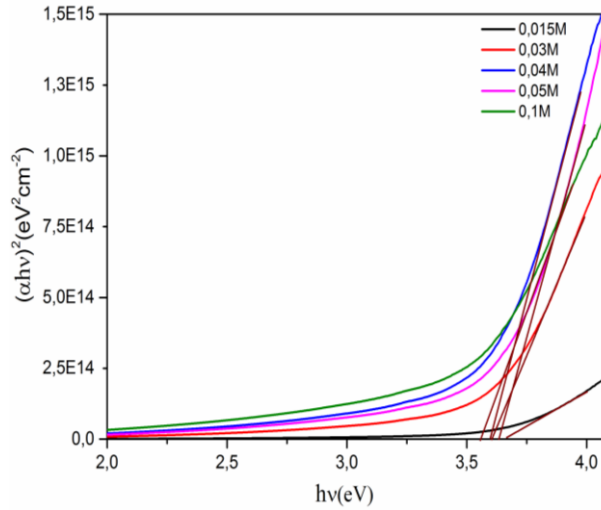


Figure III.12: Band gap (E_g) estimation from Tauc's relation of NiO thin films prepared at 500°C with different of precursor concentration.

In general it was shown that the band gap of all samples is inverted to Urbach energy and the grain size is in respect to equation [56]:

$$\Delta E = E_{gn} - E_{gb} = \frac{\hbar^2 \pi^2}{m^*} \frac{1}{R^2} \quad (\text{III. 8})$$

Driven from the well known formula given by the following relation [57]:

$$\Delta E = \left(E_{gb}^2 + \frac{2\hbar^2 \pi^2}{m^* R^2} \right)^{1/2} \quad (\text{III. 9})$$

This relation can be rewritten as follows:

$$E_{gn} = E_{gb} \left(1 + \frac{2\hbar^2 \pi^2 / m^*}{E_{gb} R^2} \right)^{1/2} \quad (\text{III. 10})$$

Where, E_{gn} is the band gap of the film, E_{gb} is the band gap of bulk form of the material, and m^* and R are the electron effective mass and the radius of the nanocrystallites (or grains). Also this relation can be expanded as a series by neglecting the higher order of terms (since $2\hbar^2 \pi^2 / m^* / E_{gb} R^2 \ll 1$) yielding to the final expression, cited above, giving the variation of E_g as function of radius of crystallite size and confirms what is found in this study and observed from Figure III.9.

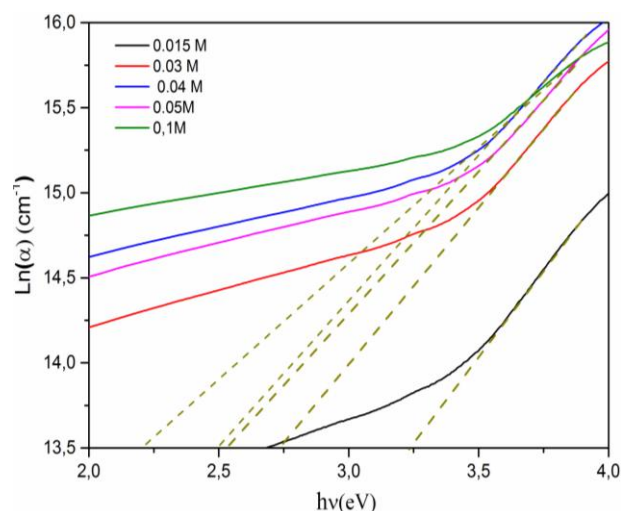


Figure III. 13. Urbach energy (E_u) estimation of NiO thin films prepared at 500°C with different of precursor concentration

3.3.4.4 Electrical properties

It is worth noting that NiO is known as a p-type semiconductor due to the Ni^{+2} vacancies which are the considered defect for its p-type conductivity [58, 59]. Seebeck effect was processed on all the samples and confirmed their p-type conductivity. The room temperature electrical conductivity (σ) was calculated using the four-point probe. Figure III.14 represents the electrical conductivity and the film thicknesses plotted as function of the precursor concentration; as can be seen from this plot the conductivity of the NiO thin films decreases 2^{-1} for thin film deposited with 0.015M to a feeble value ($0.11\Omega^{-1}\text{cm}^{-1}$) at 0.04M then increases to reach $0.53\Omega^{-1}\text{cm}^{-1}$ at 0.1M. The electrical conductivity (σ) was correlated to the film thicknesses revealing the same behavior upon the precursor concentration.

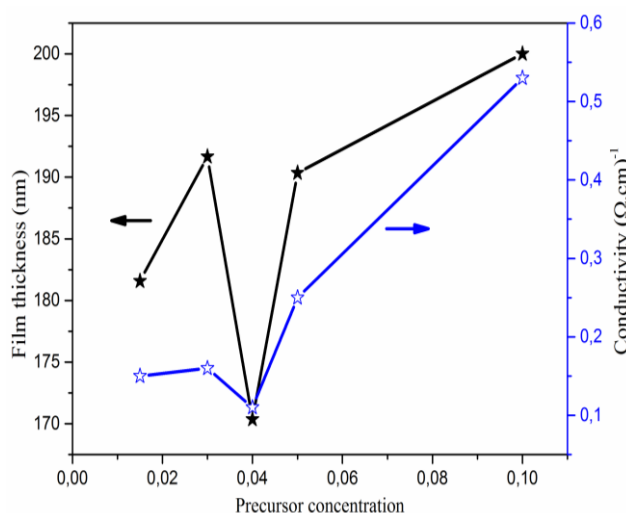


Figure III.14: Variations of conductivity and thickness (t) of NiO thin films as function of precursor concentration prepared at 500°C.

3.4 Effect of sprayed solution volume

The growth and quality of deposited films can easily be adapted by one or more deposition parameters such as spray rate, substrate temperature, doping concentration, nozzle-substrate distance. We focused in this section study of the impact of sprayed solution volume on structural, optical and electrical properties of NiO thin films elaborated by the predicted method with a fixed temperature.

3.4.1 Experimental procedure

3.4.2 Films preparation

NiO films were prepared by spray pyrolysis process with different amount of volume. The range of spraying solution volume was varied from 5ml to 30 ml with the step of 5ml. As a source of nickel, a starting solution was prepared by dissolving 0.5 M (Ni (NO₃)₂.6H₂O) in 40 ml double distilled water. The solution was stirred thoroughly using a magnetic stirrer at 50°C for half an hour to yield a clear and transparent solution; then it was sprayed on 500°C heated glass substrate. Other deposition conditions such as distance nozzle-substrate were fixed at 45 cm, whereas sprayed flow rate of the solution was taken 2ml/min, each spray time took 10s and time interval between successive sprays was 10s to maintain constant the heat of substrate. The later was (R217102) microscopic glass slide in size of (75×25×1.1 mm³). Before deposition process, glass substrates were treated in standard cleaning procedure as follow: rinsing in acetone and distilled water respectively for 10min, and then blowing dry with a compressed air.

3.4.3 Films characterization

The structural properties of prepared thin films were investigated using X-ray diffraction (BRUKER - AXS type D8) equipped with X'Pert High Score under Cu K α ($\lambda = 1.5406\text{\AA}$) radiation. The scanning range of (2θ) was taken between 20° and 90°. Survey of NiO bonding formation was obtained by Fourier transformed infrared spectroscopy (Shimadzu IR-Infinity1); for all prepared samples the scan of the FT-IR measurements was performed in (400-4000cm⁻¹) range. The optical transmission spectra were obtained using an UV-visible spectrophotometer (Shimadzu, Model 1800); the scanning measurements were ranged in 300-900nm. Film thickness (t) was measured by the well-known weight difference method considering the density of the bulk nickel oxide taken in this work (6.67 g/cm³). To confirm the nature of conductivity Seebeck effect were carried out. The electrical conductivity of the films was measured in a coplanar structure obtained with the evaporation of four golden stripes on the deposited film surface; the measurements were performed with

Keithley Model 2400 low voltage source meter instrument. All measurements were carried out at room temperature.

3.4.4 Result and discussions

3.4.4.1 Structural properties

At various sprayed solution volume, X-ray diffraction patterns of the sprayed NiO thin films, on 500°C heated substrates, were scanned in 20°- 90° range and shown in Figure III.15. It has been observed from this figure that the film prepared with 5ml spraying solution volume is amorphous in nature, indicating a poor crystallinity of the film. This may be due to the dispersed starting nucleation of NiO formation. With increasing the volume to 10ml, only one peak at (111) was observed whereas for the others (15, 20, 25 and 30ml) sprayed solution volume, one can observe that tow peaks are present at $2\theta = 37.2^\circ$ and 43.3° as-signed to the (111) and (200) crystal planes respectively, these diffraction peaks were indexed to the face-centered cubic (FCC) crystalline structure of NiO and matched well with the standard spectrum (JCPDS, No. 47-1049) under the space group $Fm\bar{3}m$ (225). The presence of such peaks indicates that the films are polycrystalline in nature. From the XRD analysis, it was found that the (111) peak has the highest intensity indicating the preferred orientation. It can also be seen from Figure III.15 that the intensity of the peaks gradually increases with spraying solution volume. The increase in the intensity of the peaks may be attributed to the increase in the degree of crystallinity caused by increasing of the sprayed quantity in conjunction with heat stay at 500°C of samples due to time deposition of the solution. Similar results are also reported in the literature [60, 61].

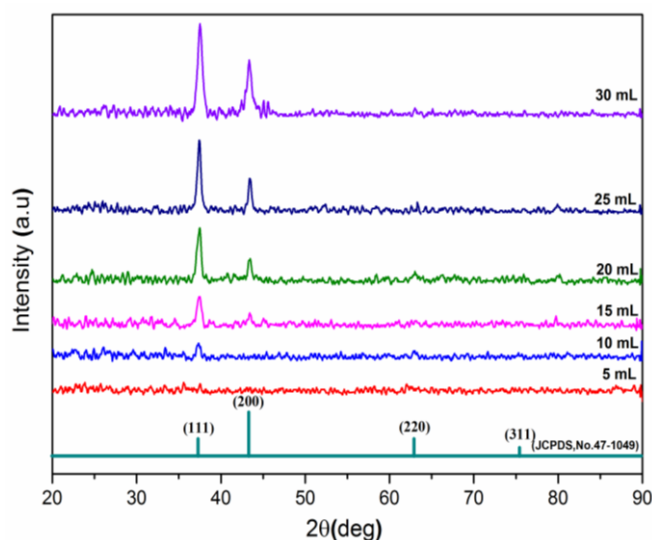


Figure III.15: X-ray patterns of NiO thin films prepared at 500°C with different sprayed volume

The lattice parameters such as lattice constant a , the average grain size G , the dislocation density δ , and the mean strain ε , of the NiO thin films has been calculated using precedent equations and presented in Table III.6.

Sprayed solution Volume (ml)	2θ (deg)	Lattice constants (\AA)		Grain size (nm)	ε (%)	$\delta \times 10^{15}$ (lines/m ²)
		a	$\Delta a = a - a_0$			
5	-	-	-	-	-	-
10	37.292	4.1728	-0.0040	10.0	-0.096	9.734
15	37.431	4.1610	-0.0158	16.0	-0.378	3.679
20	37.438	4.1614	-0.0154	18.5	-0.370	2.906
25	37.457	4.1586	-0.0182	21.0	-0.436	2.225
30	37.318	4.1735	-0.0033	27.8	-0.080	1.292

Table III. 6: Values of Bragg angle 2θ , lattice constants a , grain size G , mean strain ε and dislocation density δ for the (111) plane of NiO thin films prepared at 500°C with different sprayed volume

As can be seen, the calculated lattice parameter values are lower than standard a_0 given by the cards (*JCPDS, No. 47- 1049*). The deviation in the values of the lattice constant of the as-prepared NiO films from the bulk value indicates the presence of strain in the films. The origin of internal strain is related to the grain size of the film, which depends upon to deposition condition of the films [62]. Figure III.16 shows the variation of grain size, calculated using Scherrer's formula of the NiO samples versus sprayed solution volume. As can be seen, the value of grain size was found to increase from 10.0 to 27.8 nm with increasing of sprayed solution volume from 10ml to 30ml respectively. These results confirm the enhancement in the crystallinity of the films. Furthermore, the increase in the grain size indicates a decrease in the lattice defects, which in turn reduces dislocation density as seen in Table III. 6.

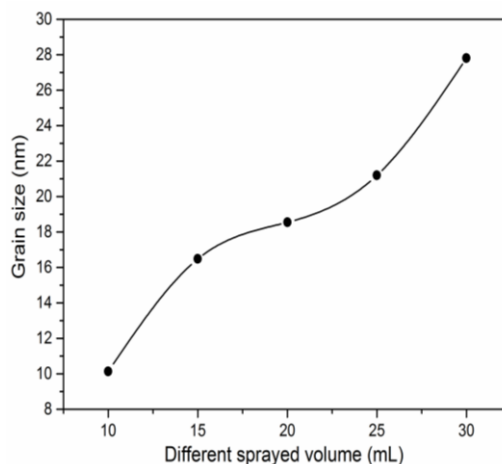


Figure III.16: Variation of grain size of NiO thin films prepared at 500°C with different sprayed volume

3.4.4.2 Fourier Transform Infrared (FT-IR) analysis

To further support the XRD results, the quality and composition of NiO thin films were investigated by FT-IR spectroscopy. FT-IR is known as one of the very useful methods to find out information about chemical bonding and identification of material elemental constituents. Metal oxides generally give absorption bands below 1000 cm^{-1} arising from inter-atomic vibrations [63]. FT-IR spectra in of the NiO thin films prepared with spraying solution volume ranged in 5-30 ml are represented in Figure III.17. From 5 to 15ml sprayed solution volume, as seen in Figure III.17 (a) which shows absorption wave number bands located at 420, 423, 447, 476, 515, 570, 620, 674, 723, 750 and 820 cm^{-1} which were assigned to Ni-O stretching vibrations modes [30-32,40, 64-68]. Figure III.17 (b) represents the FT-IR spectra obtained from the NiO films prepared at sprayed solution volume varied from 20 to 30ml, one can observe that absorption bands at 420, 430, 440, 466, 580, 612, 640, 678, 713, 790 and 820 cm^{-1} corresponding to a stretching vibration of the Ni-O bond and also authenticates the presence of NiO material [31, 32,40,64, 66-68], whereas bond at around 466 cm^{-1} is resulting from the NiO lattice vibration [68].

It worth noting that absorption band at 820 cm^{-1} appears in all spectra; this bond is evaluated using Hook's law giving by the precedent equation, thus the position of specific band absorption of nickel oxide powders is determined on the basis of the bond force constant k ($=5.105\text{ dyne/cm}$) and the reduced mass μ ($=1/m_{\text{Ni}}+1/m_{\text{O}}$) which leads to an absorption band at 821 cm^{-1} closely to the observed one in all spectra of Figure III.17 (a-b).

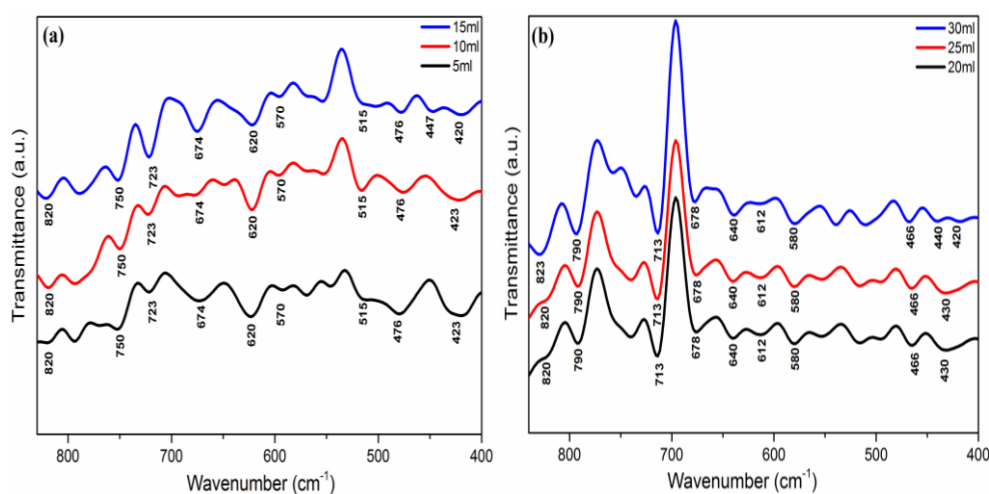


Figure III. 17: FT-IR spectra of NiO thin films prepared at 500°C with sprayed volume (a) from 5ml to 15ml, (b) from 20ml to 30ml

3.4.4.3 Optical properties

Figure III.18 shows the optical transmission as a function of the wavelength in a 300-900nm range of undoped NiO thin films for different sprayed solution volume. It is clear that the obtained films exhibit high transparency in the visible region. The average transmission value is over than 80% for the 5 ml deposited sample and decreases to reach the value of 50% for the 30 ml deposited one revealing the effect of the thickness given by Lambert's law. A drastic decrease in transmission is located between 300-360 nm revealing the region of the absorption edge in the layers due to the transition between valence and conduction bands due to onset fundamental absorption.

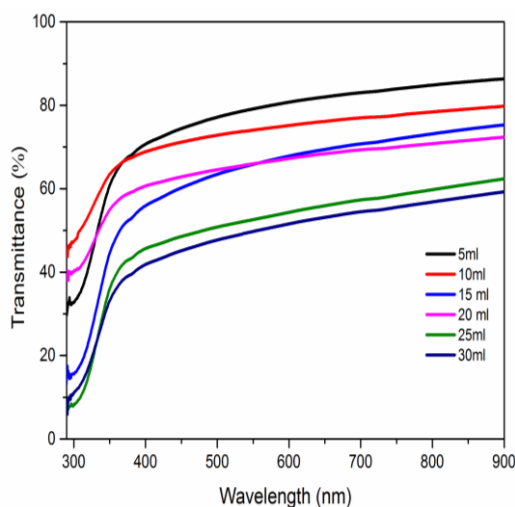


Figure III.18: Spectral transmittance plots of NiO thin films prepared at 500°C with different sprayed volume

The thickness (t) of the films was calculated by using weight difference method. Thickness values are reported in Table III.7. As can be seen from Figure III.19, film thickness increases from 168 to 223 nm when sprayed volume solution increases from 5 to 30ml. This reveals the amount of sprayed quantities of material hence precursor concentration was kept constant during the deposition process.

Sprayed solution volume (ml)	Thickness t (nm)	Band gap energy E_g (eV)	Urbach energy E_u (meV)	Resistivity ρ (Ω .cm)
5	168	3.59	342.465	52,208
10	203	3.44	370.370	40,742
15	213	3.62	355.871	27,580
20	216	3.38	413.223	20,976
25	218	3.56	363.636	14,113
30	223	3.55	401.606	8,662

Table III. 7: Values of thickness t , band gap energy E_g and Urbach energy E_u of NiO thin films prepared at 500°C with different sprayed volume

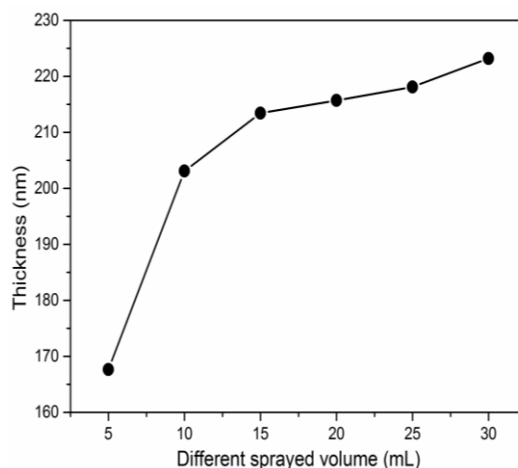


Figure III.19: Variation of NiO thin films thickness prepared at 500°C with different sprayed volume

Direct band gap was determined using well known Tauc's relation as shown in Figure III.20. The obtained E_g values are given in Table III.7. As clearly seen from this table, optical band gap variation of NiO thin films is ranged in 3.59-3.55 eV when solution volume changed from 5 to 30ml. Those obtained E_g values are in good agreement with earlier reports [43]. Fluctuation in optical gap energy which is directly related to the presence of energy levels in the gap of material. This suggests modifications in its electronic structure.

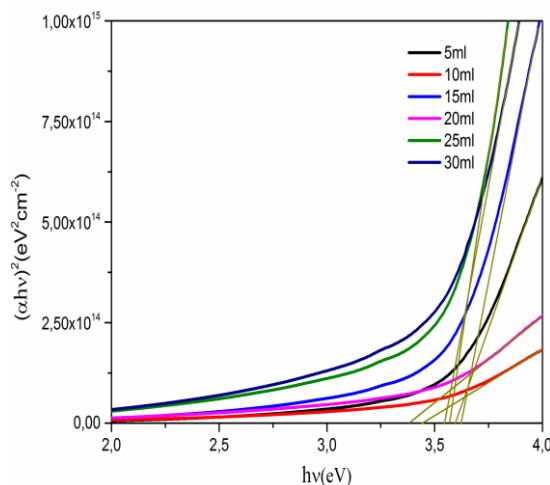


Figure III.20: Estimation of band gap energy (E_g) from Tauc's relation of NiO thin films prepared at 500°C with different sprayed volume

The width of the localized states is available in the optical band gap of the NiO films and affects both optical band gap structure and transitions. The Urbach tail is related directly to a similar exponential tail for the density of states near band edges as defined from the previous formula. E_u values were calculated and summarized in Table III.6. As it was seen in Figure III.21, The estimated E_u values are found to be averaged between lowest value 342.46 meV (for 5ml sprayed solution) and highest value 413.22 meV (for 20ml sprayed

solution) for the undoped NiO thin films. Also, we found that the E_u values change inversely with the optical band gap of the films, as discussed earlier and expressed in the literature [69].

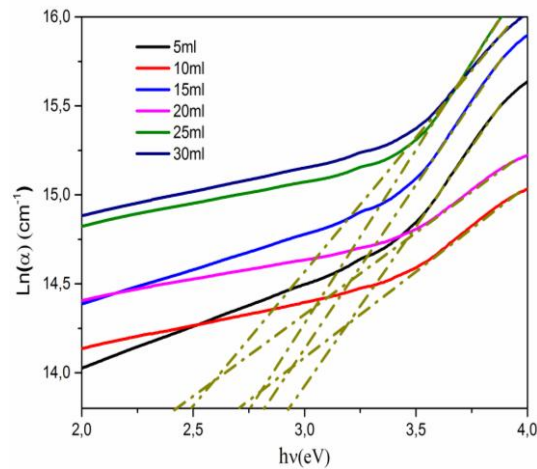


Figure III.21: Estimation of Urbach energy (E_u) of NiO thin films prepared at 500°C with different sprayed volume.

We can easily observe from Table III.7 and Figure III.22 that Urbach energy is inverted to gap energy. Such decrease in the optical band gap with increasing Urbach energy can be attributed to the presence of unstructured defects that increase the density of localized states in the band gap and consequently decrease the energy gap and vis-versa [70].

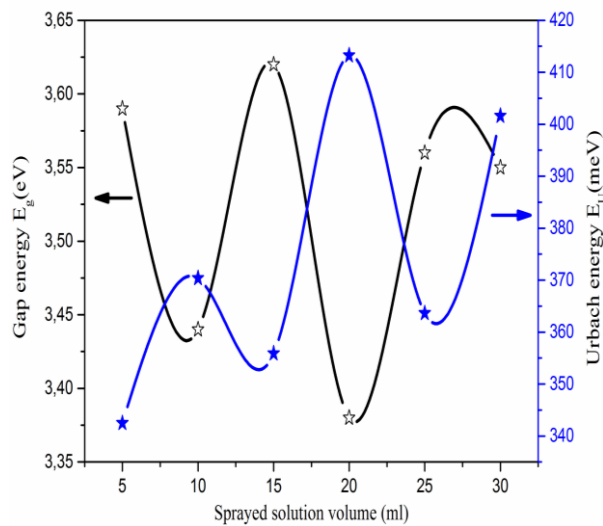


Figure III.22: Variation of band gap energy (E_g) and Urbach energy (E_u) of NiO thin films prepared at 500°C with different sprayed volume.

3.4.4.4 Electrical properties

The hot probe test results showed that the conduction natures are p-type semiconductor for all films. Figure III.23 shows the variation in the resistivity and grain sizes of undoped NiO thin films with the variation of precursor solution volumes. The resistivity of these films decreases from 52.208 to 8.662 ($\Omega\cdot\text{cm}$) with an increase in precursor solution

volume from 5 to 30 ml. In addition it is observed from Figure III.23 that as the volume of the spray solution increases, the crystallite size also increases, as consequent more continuously coated film, which has an effect to improving the electron mobility and its conductivity can be enhanced by an increase of Ni vacancies and/or interstitial oxygen in NiO crystallites leading to the formation of Ni^{3+} [71]. The decrease in resistivity may be related to the increase in crystallite size and this leads to a decrement in the trapping states at the grain boundary. The grain boundary has main responsibility in the carrier transport as it reported by Prathap et al. [72]. Therefore the electrical properties of films depend strongly on surface effects, the grain size and the boundaries between them [73, 74].

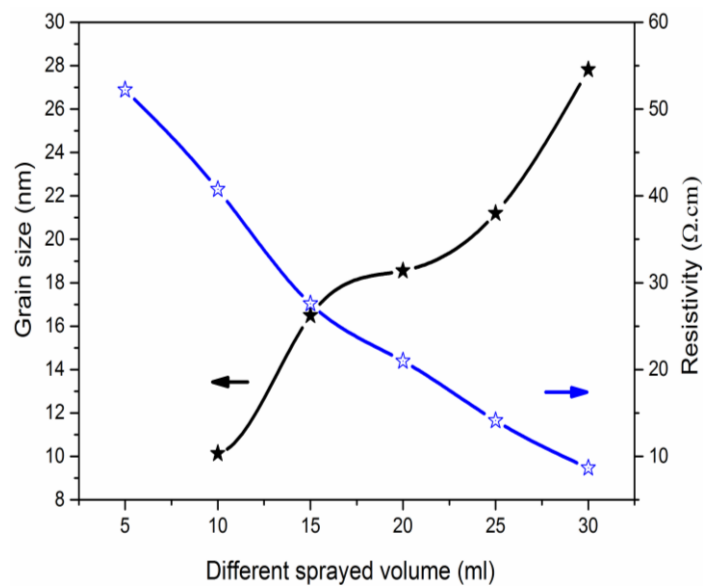


Figure III.23: Variations of resistivity and grain size (G) of NiO thin films as prepared at 500°C with different sprayed volume.

References

- [1] L. Cattin, B.A Reguig, A. Khelil, Properties of NiO thin films deposited by chemical spray pyrolysis using different precursor solutions, *Appl Surf Sci*, 254 (2008) 5814-5821.
- [2] H. Kamal, E.K. Elmaghraly, S.A. Ali, The electrochromic behavior of nickel oxide films sprayed at different preparative conditions, *Thin Solid Films*, 483(2005) 330-339.
- [3] A. Boukhachem, R. Boughalmi, M. Karyaoui, Study of substrate temperature effects on structural, optical, mechanical and opto-thermal properties of NiO sprayed semiconductor thin films, *Materials science and engineering: B*, 188 (2014) 72-77.
- [4] S. Kasuma, W. Ningsih, Effect of various solvent on the synthesis of NiO nanopowders by simple sol-gel methods and its characterization, *Indones. J. Chem*, 15 (2015) 50-55.
- [5] D. Nikolić, M. Panjan, G.R. Blake, Annealing-dependent structural and magnetic properties of nickel oxide (NiO) nanoparticles in a silica matrix, *journal of the European ceramic society*, 35(2015) 3843-3852.
- [6] P. Ravikumar, B. Kisan, A. Perumal, Thickness dependent ferromagnetism in thermally decomposed NiO thin films, *journal of magnetism and magnetic materials*, 418(2016) 86-91.
- [7] K. Martin, G.McCarthy: North Dakota State Univ, Fargo, ND, USA, ICCD Great-in-Aid, 1991.
- [8] N. Talebian, M. Kheiri, Sol-gel derived nanostructured nickel oxide films: Effect of solvent on crystallographic orientations, *Solid State Sciences*, 27 (2014) 79-83.
- [9] N. Khedmi, M. Ben Rabeh, M. Kanzari, Structural Morphological and Optical Properties of SnSb₂S₄ Thin Films Grown by Vacuum Evaporation Method, *J. Mater.Sci.Technol*, 30 (2014) 1006-1011.
- [10] Z. H. Liu, W. H. Li, S. Topa, Fine Tuning of Fluorene-Based Dye Structures for High-Efficiency p-Type Dye-Sensitized Solar Cells, *ACS Appl. Mater. Interfaces*, 2014, 6 (13):10614-10622.
- [11] F.R. Lamastra, F. Nanni, F. Menchini, Transparent nanostructured electrodes: Electrospun NiO nanofibers/NiO films, *Thin Solid Films*, 601(2016) 54-58.
- [12] M. Thirumoorthi, J.T.J. Prakash, Effect of F doping on physical properties of (211) oriented SnO₂ thin films prepared by jet nebulizer spray pyrolysis technique, *Superlattices and Microstructures*, 89 (2016) 378-389.
- [13] J. Tauc, R. Grigorovici, A. Vancu, Optical Properties and Electronic Structure of Amorphous Germanium, *phys.status solidi*, B15 (1966) 627.
- [14] B. Sasi, KG. Gopchandran, Nanostructured mesoporous nickel oxide thin films, *Nanotechnology*, 18(2007) 115613.
- [15] S.A. Mahmoud, A.A. Akl, S.M. Al-Shomar, Effect of some preparative parameters on optical properties of spray deposited iridium oxide thin films, *Phys. B*, 2009, 404: 2151-2158.
- [16] F. Urbach, The Long-Wavelength Edge of Photographic Sensitivity and of the Electronic Absorption of Solids, *Phys. Rev.*, 1953, 92: 1324.
- [17] S. Benramache, F. Chabane, B. Benhaoua, Fatima Z. Lemmadi, nfluence of growth time on crystalline structure, conductivity and optical properties of ZnO thin films, *Journal of semiconductors*, 2013, 34: 023001.

- [18] J. Melsheimer, D. Ziegler, Band gap energy and Urbach tail studies of amorphous, partially crystalline and polycrystalline tin dioxide, *Thin Solid Films*, 129(1985) 35-47.
- [19] Y.M Lu, W.S Hwang, J.S Yang, Effects of substrate temperature on the resistivity of non-stoichiometric sputtered NiO_x films *Surf. Coat. Technol*, 155(2002) 231-235.
- [20] H.L. Chen, Y.M. Lu, Jun-Yi Wu, Effects of Substrate Temperature and Oxygen Pressure on Crystallographic Orientations of Sputtered Nickel Oxide Films, *Materials Transactions*, 46(2005) 2530-2535.
- [21] Y. Zhao, H. Wang, C. Wu, Structures, electrical and optical properties of nickel oxide films by radio frequency magnetron sputtering, *Vacuum*, 103(2014) 14-16.
- [22] H. Sato, T. Minami, S. Takata, T.Yamada, Transparent conducting p-type NiO thin films prepared by magnetron sputtering, *Thin Solid Films* 236(1993) 27-31.
- [23] C.M. Mahajan, M. Pendharkar, Y.A. Chaudhari, Spray Deposited Nanocrystalline ZnO Transparent Electrodes: Role of Precursor Solvent, *journal of nano and electronic physics*, 8(2) (2016) 02026.
- [24] H.L. Chen, Y.M. Lu, W.S. Hwang, Effect of film thickness on structural and electrical properties of sputter-deposited nickel oxide films, *Materials Transactions*, 46(2005) 872-879.
- [25] J. Wang, P. Yang, X. Wei, and Z. Zhou, Preparation of NiO two-dimensional grainy films and their high-performance gas sensors for ammonia detection, *Nanoscale Research Letters*, 10(2015) 1-6.
- [26] N. Khedmi, M. Ben Rabeh, M. Kanzari, Structural morphological and optical properties of SnSb₂S₄ thin films grown by vacuum evaporation method, *Journal of Materials Science and Technology*, 30 (2014) 1006–1011.
- [27] A. Lagashetty, V. Havanoor, S. Basavaraja, S. D. Balaji, A. Venkataraman, Microwave-assisted route for synthesis of nanosized metal oxides, *Science and Technology of Advanced Materials*, 8 (2007) 484-493.
- [28] A. S. a. P. S.Kumar, Synthesis and characterization of NiO-ZnO nano composite, *Nano Vision*, 1 (2011) 112-115.
- [29] M. El-Kemary, N. Nagy, and I. El-Mehasseb, Nickel oxide nanoparticles: synthesis and spectral studies of interactions with glucose, *Materials Science in Semiconductor Processing*, 16 (2013) 1747-1752.
- [30] A. Rahdar, M. Aliahmad, Y. Azizi, NiO nanoparticles: synthesis and characterization, *Journal of Nanostructures*, 5 (2015) 145-151.
- [31] A. S. Adekunle, J. A. O. Oyekunle, O. S. Oluwafemi, Comparative catalytic properties of Ni(OH)₂ and NiO nanoparticles towards the degradation of nitrite (NO₂) and nitric oxide (NO), *International Journal of Electrochemical Science*, 9(2014) 3008–3021.
- [32] K. Sajjalal and A. Moses Ezhil Raj, Effect of thickness on physico-chemical properties of p-NiO (bunsenite) thin films prepared by the chemical spray pyrolysis (CSP) technique, *Optik*, vol. 127(2016) 1442-1449.
- [33] P. C. Yu, G. Nazri, and C. M. Lampert, Spectroscopic and electrochemical studies of electrochromic hydrated nickel oxide films, *Solar Energy Materials*, 16 (1987) 1–17.

- [34] P. Baraldi, G. Davolio, G. Fabbri, T. Manfredini, spectral and thermal study on nickel(II) hydroxides, *Materials Chemistry and Physics*, 21 (1989) 479- 493.
- [35] P.V. Kamath, G.N. Subbanna, Electroless nickel hydroxide: synthesis and characterization, *Journal of Applied Electrochemistry*, 22(1992) 478-482.
- [36] R. Cerc Korošec, P. Bukovec, B. Pihlar, A. Šurca Vuk, B. Orel, G. Držić, Preparation and structural investigations of electrochromic nanosized NiOx films made via the sol-gel route, *Solid State Ionics*, 165(2003) 191–200.
- [37] Y. Wang, J. Zhu, X. Yang, L. Lu, and X. Wang, Preparation of NiO nanoparticles and their catalytic activity in the thermal decomposition of ammonium perchlorate, *Acta*, 437(2005) 106–109.
- [38] P. Oliva, J. Leonardi, J. F. Laurent et al., Review of the structure and the electrochemistry of nickel hydroxides and oxy-hydroxides, *Journal of Power Sources*, 8(1982) 229–255.
- [39] A. Al-Hajry, A. Umar, M. Vaseem, Low-temperature growth and properties of flower- shaped β -Ni(OH)₂ and NiO structures composed of thin nanosheets networks, *Super lattices and Microstructures*, 44(2008) 216–222.
- [40] X. Song , L. Gao, Facile synthesis of polycrystalline NiO nanorods assisted by microwave heating, *Journal of the American Ceramic Society*, 91 (2008) 3465–3468.
- [41] F. Davar, Z. Fereshteh, M. Salavati-Niasari, Nanoparticles Ni and NiO: synthesis, characterization and magnetic properties, *Journal of Alloys and Compounds*, 476(2009)797-801.
- [42] D. M. Fernandes, A. A. W. Hechenleitner, M. F. Silva, Preparation and characterization of NiO, Fe₂O₃, Ni_{0.04}Zn_{0.96}O and Fe_{0.03}Zn_{0.97}O nanoparticles, *Materials Chemistry and Physics*, 118 (2009) 447-452.
- [43] N. S. Das, B. Saha, R. Thapa, G. C. Das, K. K. Chattopadhyay, Band gap widening of nanocrystalline nickel oxide thin films via phosphorus doping, *Physica E: Low-Dimensional Systems and Nanostructures*, 42 (2010) 1377-1382.
- [44] A. C. Sonavane, A. I. Inamdar, P. S. Shinde, H. P. Deshmukh, R. S. Patil, P. S. Patil, Efficient electrochromic nickel oxide thin films by electrodeposition, *Journal of Alloys and Compounds*, 489 (2010) 667- 673.
- [45] K. Ashok, Characterization of nickel oxide thin film– DC reactive magnetron sputtering, *Surface Review and Letters*, 18(2011) 11-15.
- [46] M. Alagiri, S. Ponnusamy, C. Muthamizhchelvan, Synthesis and characterization of NiO nanoparticles by sol-gel method, *Journal of Materials Science: Materials in Electronics*, 23(2012) 728-732.
- [47] S. V. Ganachari, R. Bhat, R. Deshpande, A. Venkataraman, Synthesis and characterization of nickel oxide nanoparticles by self-propagating low temperature combustion method, *Recent Research in Science and Technology*, 4(2012) 4.
- [48] L. G. Teoh, K.-D. Li, Synthesis and characterization of NiO nanoparticles by sol-gel method, *Materials Transactions*, 53 (2012) 2135-2140.
- [49] D. Devadatha, R. Raveendran, Structural and dielectric characterization of nickel-cobalt oxide nanocomposite, *Journal of Material Science & Engineering*, 11(2013).

- [50] W. Yuan, F. Liu, and Z. Zhang, Preparation and characterization of mesoporous Nickel oxide templated by different mixed surfactants, *Chinese Journal of Inorganic Chemistry*, 29 (2013) 803–809.
- [51] A. E. A. A. Said, M. M. A. El-Wahab, S. A. Soliman, and M. N. Goda, Synthesis and characterization of nano CuO-NiO mixed Oxides, *Nanoscience and Nano engineering*, vol. 2(2014) 17–28.
- [52] W. O. George and P. S. McIntyre, *Infrared Spectroscopy*, John Wiley & Sons, Inc, NJ, USA, 1987.
- [53] S. Benramache, B. Benhaoua, influence of substrate temperature and Cobalt concentration on structural and optical properties of ZnO thin films prepared by Ultrasonic spray technique Superlattices and Microstructures, 52 (2012) 807–815.
- [54] J.D. Desai, S. K. Min, K.-D. Jung, O. S. Joo, Spray pyrolytic synthesis of large area NiO_x thin films from aqueous nickel acetate solutions *Applied Surface Science*, 253(2006) 1781–1786.
- [55] H. A. Juybari, M. M. Bagheri-Mohagheghi, M. Shokoooh- Saremi, Nickel-lithium oxide alloy transparent conducting films deposited by spray pyrolysis technique, *Journal of Alloys and Compounds*, 509 (2011) 2770-2775.
- [56] S. L. S. Rao, G. Ramadevudu, M. Shareefuddin, A. Hameed, M. N. Chary, and M. L. Rao, Optical properties of alkaline earth borate glasses, *International Journal of Engineering, Science and Technology*, 4(2013) 25-35.
- [57] K. J. Han, K. S. Kang, Y. Chen, K. H. Yoo, J. Kim, Effect of annealing temperature on the conduction mechanism for a sol-gel driven ZnO Schottky diode, *Journal of Physics D: Applied Physics*, 42 (2009) 125110.
- [58] P. Mohanty, C. Rath, P. Mallick, R. Biswal, N. C. Mishra, UV-visible studies of nickel oxide thin film grown by thermal oxidation of nickel *Physica B: Condensed Matter*, 405(2010) 2711–2714.
- [59] S. Nandy, B. Saha, M. K. Mitra, and K. K. Chattopadhyay, Effect of oxygen partial pressure on the electrical and optical properties of highly (200) oriented p-type Ni_{1-x}O films by DC sputtering *Journal of Materials Science*, 42 (2007) 5766–5772.
- [60] R. Sharma, A. D. Acharyaa, S.B. Shrivastavaa, T. Shripathi, V. Ganesan, Preparation and characterization of transparent NiO thin films deposited by spray pyrolysis technique, *Optik*, 125(2014) 6751-6756.
- [61] P.S. Patil, L.D. Kadam, Preparation and characterization of spray pyrolyzed nickel oxide (NiO) thin films, *Appl. Surf. Sci.*, 199(2002) 211-212.
- [62] M.A. Islam, M.S. Hossain, M.M. Aliya, M.M. Aliyu, J. Husna, M.R. Karim, K. Sopian, N. Amin, Comparison of Structural and Optical Properties of CdS Thin Films Grown by CSVT, CBD and Sputtering Techniques, *IEEE Phot.Spec. Conf.*, 38(2012) 000151.
- [63] I. G. Morozov, C.V. Belousova, D. Ortega, M.-K. Mafinac, M.V. Kuznetcov, Structural, optical, XPS and magnetic properties of Zn particles capped by ZnO nanoparticles, *J. Alloy. Compd.*, 633(2015) 237-245.
- [64] V. Biju, M. Abdul Khadar, Fourier transform infrared spectroscopy study of nanostructured nickel oxide, *Spectrochim. Acta A*, 59 (2003) 121-134.

- [65] N. Dharmajar, P. Prabu, S. Nagarajan, C.H. Kim, J.H. Park, H.Y. Kim, Synthesis of nickel oxide nanoparticles using nickel acetate and poly (vinyl acetate) precursor, *Mat. Sci. Eng. B*, 128(2006) 111-114.
- [66] R.A. Ismail, S. Ghafari, G.A. Kadhim, Preparation and characterization of nanostructured nickel oxide thin films by spray pyrolysis, *Appl. Nanosci.*, 3(2013) 509-514.
- [67] A. Mhamdi, R. Dridi, A. Arfaoui, C. Awada, M. Karyaoui, I.A. Velasco-Davalos, A. Ruediger, M. Amlouk, Structural, surface morphology and optical properties of NiSnO₃ thin films prepared using spray technique, *Opt. Mater.*, 47(2015) 386-390
- [68] M. Aghazadeh, A.N. Golikand, M. Ghaemi, Synthesis, characterization, and electrochemical properties of ultrafine β -Ni(OH)₂ nanoparticles *Int. J. Hyd. Energy.*, 36(2011) 8674-8679.
- [69] C. Mrabet, M. Ben Amor, A. Boukhachem, M. Amlouk, T. Manoubi, Physical properties of La-doped NiO sprayed thin films for optoelectronic and sensor applications, *Ceram. Int.*, 42(2016) 5963-5978.
- [70] M.R. Islam, J. Podder, Optical properties of ZnO nano fiber thin films grown by spray pyrolysis of zinc acetate precursor, *Cryst. Res. Tech.*, 44(2009) 286-292.
- [71] W.L. Jang, Y.M Lu, W.S Hwang, W.C Chen, Electrical properties of Li-doped NiO films, *Journal of the European Ceramic Society* 30 (2010) 503-508.
- [72] P. Prathap, Y.P.V. Subbaiah, k.T. Ramakrishna Reddy, R.W. Miles, Influence of growth rate on microstructure and optoelectronic behaviour of ZnS films, *J. Phys. D: Appl. Phys.* 40 (2007) 5275.
- [73] W. Zhang , S.H. Brongersma , T. Clarysse , T. Terzieva , E. Rosseeel , W. Vandervorst , K. Maex , Surface and grain boundary scattering studied in beveled polycrystalline thin copper films , *J. Vac. Sci. Technol. B*22 (2004) 1830-1833 .
- [74] F. Paraguay D. , W. Estrada L. , D.R. Acosta N. , E. Andrade , M. Miki-Yoshida , Growth, structure and optical characterization of high quality ZnO thin films obtained by spray pyrolysis, *Thin Solid Films* 350 (1999) 192-202 .

Chapter IV

Synthesis And Characterizations Of doped NiO Thin Films

4.1 Introduction

Metal oxide nanoparticles have a large surface area, which gives the nanomaterials greater advantage over conventional materials in many applications. Metal oxides in general, are often slightly non-stoichiometric, resulting in either an excess or deficiency in metal ions compared to oxygen ions giving either n or p-type semiconductors. Non-stoichiometry is essentially important in transition metal oxides and it varies with the surrounding atmosphere, impurities, and morphologies and is regarded as a typically mixed valence semiconductor [1].

The most important methods to enhance the characteristics of the materials is the incorporation of dopant in the materials [2]. On the other hand doping with metallic elements like Li, Cd, Al, K, La, and Cu are an effective way to change physical properties of NiO thin films [3-8]. In this study, Copper (Cu) and lithium (Li) doped nickel oxide thin films were elaborated using spray pyrolysis technique. The dependence of Cu and Li doping concentration on the structural, compositional, optical, photoluminescence and electrical properties have been discussed in this section.

4.2 Effect of Copper doped NiO thin films

Recently few researchers have been achieved to the influence of doping copper (Cu) in NiO thin films, in this regard, doping with Cu elements in NiO film have been focused in this work. In this section, the influence of Cu content on the structural, compositional, optical, photoluminescence, and electrical properties of the deposited NiO films using spray pyrolysis method were considered in detail.

4.2.1 Experimental procedure

4.2.2 Synthesis of thin films

Undoped NiO and copper doped NiO thin films were synthesized using spray pyrolysis. The starting solution was prepared from 0.1 M (Ni (NO₃)₂, 6H₂O) nickel nitrate dissolved in 40 ml double distilled water. For copper doping, copper chloride (CuCl₂, 2H₂O) was added to the above solution with appropriate weight ratios of Cu to Ni varied from 0 to 5 wt. %. The mixture solution was stirred at 50°C using a magnetic stirrer for half an hour to get a green and homogenous solution. After that, the solution was sprayed onto heated substrates at 500°C. The distance between the nozzle and the substrate was kept constant at 45 cm, whereas sprayed flow rate of the solution was taken 2 ml/min, each spray time took 10s separated by 10s as the time interval of stay to maintain the heat of substrates constant. The substrates were (R217102) microscopic glass slide in size of (75×25×1.1 mm³). Before

deposition process, a standard cleaning of substrates was kept as follow: rinsing in acetone and distilled water respectively for 10min, and then blowing dry with a compressed air. After deposition, the films were allowed to cool to room temperature.

4.2.3 Thin films characterization

The structural properties of prepared thin films were investigated using X-ray diffraction (BRUKER-AXS type D8) equipped with X'Pert High Score under Cu K α ($\lambda=1.5406\text{\AA}$) radiation in the range of 20° and 70° . The functional group present in the sample was recorded using Fourier transformed infrared spectroscopy (FTIR-Perkin Elmer Spectrum 1000); the Scan of the FTIR measurements is performed over the range between $400\text{--}4000\text{ cm}^{-1}$. The optical transmission spectra were carried out by using UV–Vis spectrophotometer (Shimadzu, Model 1800) in the wavelength range $300\text{--}900\text{ nm}$. For PL measurements, the excitation wavelength was fixed at 266 nm . The electrical conductivity of the films was measured with Keithley Model 2400 low voltage source meter instrument. Film thickness (t) was measured by using weight difference method considering the density of the bulk nickel oxide, using the following formula [9]:

$$t = m/A.\rho \quad (\text{IV.1})$$

where t is film thickness; m is the mass of deposited film on the substrate; ρ is the density of nickel oxide (6.67 g/cm^3) and A is the effective area on which the film was deposited [9]. All the measurements were performed at room temperature.

4.2.4 Result and discussions

4.2.4.1 Structural properties

X-ray diffraction was used in order to understand the structure of the deposited undoped and Cu-doped NiO thin films at 500°C heated substrates. FigureVI.1 represents the XRD patterns of undoped and Cu-doped NiO thin films. As can be observed, three orientation peaks were observed in the all films identified as (111) , (200) and (220) corresponding diffraction angle 37.24° , 43.27° and 62.87° respectively. All these diffraction peaks can be perfectly indexed to the face-centered cubic (fcc) crystalline structure of NiO, which is in conformity with that of the joint committee powder diffraction system (JCPDS card No. 47-1049) under the space group $Fm3m$ (225) [10]. All the films show the polycrystalline nature with the peaks (111) , (200) and (220) . (111) peaks present the highest intensity indicating the preferred orientation. At the limit of XRD detection, no other phase, such as copper or copper oxides was observed, this result reveals that the structures of doped

NiO are not distorted by the incorporation of Cu doping. The same result is found by Chen et al. [11] revealing that, all Cu-doped NiO films displayed only NiO peaks.

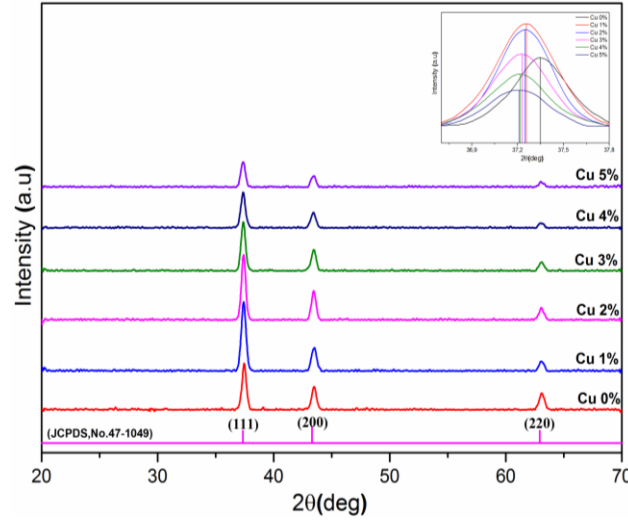


Figure IV.1: X-ray patterns of undoped and Cu-doped NiO thin films variation of diffraction intensity in the range 2θ (36.8° – 37.9°) corresponding to the (111) peak for undoped and Cu-doped NiO thin films.

It was also established that with increasing Cu doping, the diffraction peak (111) shifts toward the lower angles as observed from the Figure IV.1, which means that the doping process behaviors in increasing the lattice parameter of the NiO product. The unit cell suffers from elongation of strain, as seen in the Table IV.1. Such behavior may be attributed to the difference in the ionic radii of Cu^{2+} (0.96 \AA) and Ni^{2+} (0.69 \AA) entering in substitution in the NiO lattice which results in the expansion of NiO crystal. Similar results are also reported in the literature [12, 13]. From the XRD analysis, one can view that the intensity of the (111) peak gradually decreases with increasing Cu doping level, followed by a gradual decrease in the crystallinity of the films.

As the unit cell of the NiO is cubic in structure, its lattice constants a can be estimated using the equation [14]:

$$a = d_{hkl} \cdot \sqrt{(h^2 + k^2 + l^2)} \quad (\text{IV.2})$$

where d_{hkl} the interplanar distance and (hkl) are Miller indices.

The crystallite size of undoped and Cu-doped NiO thin films is calculated using Scherrer's formula [15]:

$$D = \frac{0.9\lambda}{\beta \cos\theta} \quad (\text{IV.3})$$

where D is the grain size, λ is the X-ray wavelength (1.54056 \AA), β is the full width at half-

maximum (FWHM) at (111) peak, and θ is the Bragg angle at the considered peak.

The mean strain ε is calculated using the following relation [16]:

$$\varepsilon = \left(\frac{a - a_0}{a_0} \right) \times 100\% \quad (\text{IV.4})$$

where a is the lattice constant of NiO thin films and a_0 the standard lattice constant of bulk material ($a_0 = 4.1769 \text{ \AA}$) according to JCPDS standard card (JCPDS, No. 47-1049).

The dislocation density δ , defined as the length of dislocation lines per unit area of the crystal, was evaluated from the formula [17]:

$$\delta = \frac{1}{D^2} \quad (\text{IV.5})$$

The structural parameters like crystallite size, dislocation density and means strain of the films are evaluated and given in Table IV.1.

Cu Concentration wt.(%)	2θ (deg)	Lattice constant (\AA)		Crystallite size (nm)	Dislocation density $\delta \times 10^{15}$ (lines /m ²)	Mean strain ε (%)
		a	$\Delta a = a - a_0$			
0	37.348	4.1689	-0.0079	37.108	7.2610	-0.1895
1	37.265	4.1779	0.0010	34.477	8.4120	0.0240
2	37.263	4.1781	0.0012	26.191	14.577	0.0299
3	37.246	4.1799	0.0030	20.150	24.628	0.0740
4	37.229	4.1818	0.0049	14.905	45.010	0.1181
5	37.215	4.1833	0.0064	11.783	72.016	0.1541

Table IV.1: Values of Bragg angle 2θ , lattice constants a , crystallite size D , mean strain ε and dislocation density δ for the (111) plane of NiO thin films as a function to the copper concentration.

As mentioned above when Cu doping increase, the variation in the lattice constant a cause to the difference in the ionic radii of Cu^{2+} and Ni^{2+} as results an expansion in the lattice constant. From Figure IV.2 the crystallite size value was found to be decreased from 37.1 to 11.7nm as the Cu doping level increases confirming the deterioration in the crystallinity of the films due to Cu doping. This phenomenon may be related to the starting nucleation generated by the presence of copper in the earlier deposition of the product on the substrate.

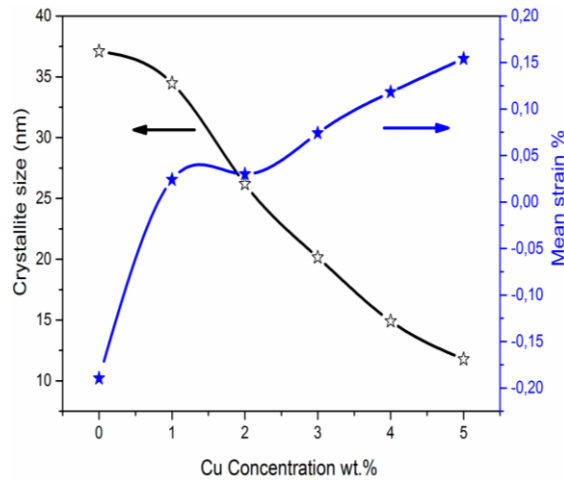


Figure IV.2: Variation of crystallite size and mean strain size of NiO thin films as a function to the copper concentration.

4.2.4.2 Fourier Transform Infrared (FT-IR) analysis

Figure IV.3 shows the FTIR spectra of undoped and Cu doped NiO thin films. The obtained spectra show an absorbed band centered around 460cm^{-1} , which assigned to the Ni-O stretching vibration mode [18, 19]. Another absorption peak is observed at 640cm^{-1} only in the Cu doped NiO films, as it was shown in the insert of Figure IV.3, which corresponds to Cu-O vibrational energy band and indicates the presence of copper within NiO samples [20, 21].

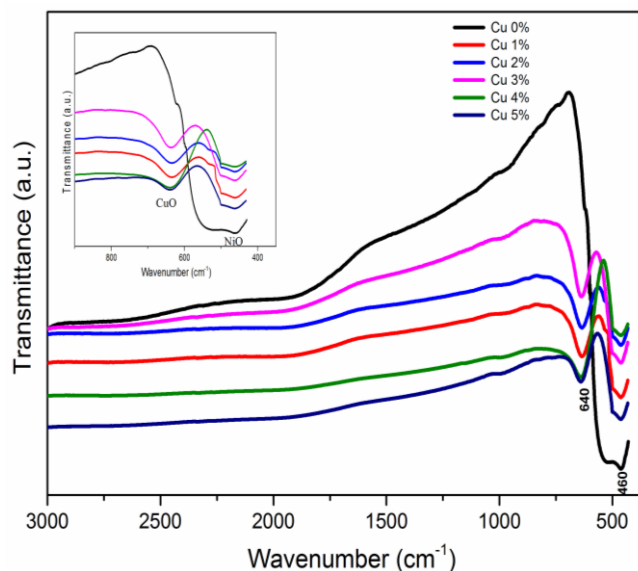


Figure IV.3: FT-IR spectra of undoped and Cu-doped NiO thin films.

4.2.4.3 Optical properties

The optical transmittance spectra of the sprayed undoped and Cu doped NiO thin films, in the wavelength ranged from 300 to 900 nm, are shown in Figure IV.4. As can be seen, the NiO samples exhibit a low transmittance and the average transmission in the visible range dramatically decreases from 64% to 35% with further increases of the Cu concentration. This decreasing in the optical transmittance may be related by the increasing thickness, photon scattering, doping with copper may also be another reason for this decreasing in the optical transmittance [22]. In the range below 350nm, it was observed the inter-band absorption in this region deduced E_g proceeded from Tauc's plot as described below.

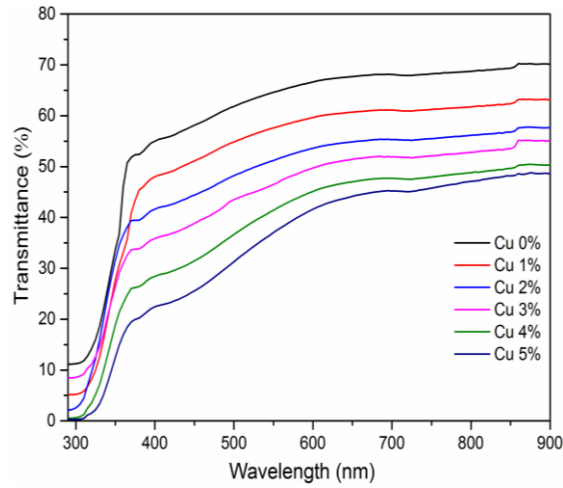


Figure IV.4: Transmittance spectra of undoped and Cu-doped NiO thin films.

The absorption coefficient α can be calculated from the transmittance T values and thickness t at the absorption edge from the Lambert's law [23]:

$$\alpha = \frac{1}{t} \ln \left(\frac{1}{T} \right) \quad (\text{IV.6})$$

The optical band gap energy E_g of the films can be determined from the transmission spectra using the following relation, known as the Tauc's relation [24]:

$$\alpha h\nu = A(h\nu - E_g)^{\frac{1}{2}} \quad (\text{IV.7})$$

where A is a constant, α is the absorption coefficient, $h\nu$ is the photon energy and E_g is the band gap energy. For directly allowed transitions the optical band gap can be obtained from the plot of $(\alpha h\nu)^2$ versus $h\nu$. Extrapolating the linear portion of the graph with energy axis gives the band gap as shown in Figure IV.5. Optical band gap values for undoped and Cu doped NiO films were estimated to be 3.60 to 3.95 eV as is tabulated in Table IV.2.

Cu concentration wt. %	Thickness t (nm)	Optical gap energy E_g (eV)	Urbach energy E_u (meV)	Conductivity σ ($\Omega^{-1} \cdot \text{cm}^{-1}$) $\times 10^{-2}$
0	102	3.60	330.79	2.33
1	114	3.62	327.97	2.77
2	125	3.64	315.05	3.25
3	131	3.73	310.26	3.04
4	138	3.77	307.50	4.30
5	144	3.95	299.94	5.91

Table IV.2: Values of thickness t , optical band gap energy E_g , Urbach energy E_u and Conductivity σ of NiO thin films as a function to the copper concentration.

For undoped NiO film, the value of E_g is 3.60 eV, which is closed in a good agreement with that obtained from the NiO bulk [25]. It is clearly seen that E_g values increase with increasing Cu concentration; this change in the E_g maybe refer to the influence of various factors such as the condition of preparation, film thickness, grain size, lattice strain and presence of impurities in the films [26-28].

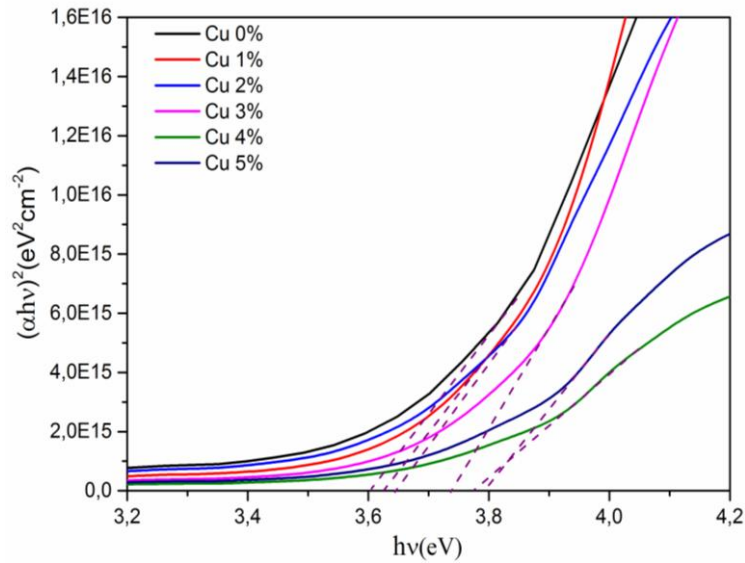


Figure IV.5: Estimation of band gap energy (E_g) from Tauc's relation of undoped and Cu-doped NiO thin films.

The Urbach energy (E_u) gives the width of the tails of the localized states within the optical band gap, which has been considered as a useful parameter to evaluate the structural disorder [29, 30]. The Urbach tail of the films can be evaluated using the following relation [31]:

$$\alpha = \alpha_0 \exp\left(\frac{hv}{E_u}\right) \quad (\text{IV.8})$$

where α_0 is a constant, $h\nu$ is the photon energy. E_u can be determined from the plot of $\ln(\alpha)$ versus $(h\nu)$ and its straight line slopes. The evaluated E_u values are listed in Table IV.2. Calculated E_u values found to be varied from 330.79 to 299.94meV. E_u values exhibit a decrease as Cu concentration increases. The decreases in E_u values may be referred to the reduced structural disorder and creation of less localized states. E_u values change inversely with the optical band gap as clearly seen from Table IV.2.

4.2.4.4 Photoluminescence studies

As it was known photoluminescence (PL) study is a helpful tool to study the generated defects in the lattice. Figure IV.6 shows the PL spectra of undoped and Cu-doped NiO prepared thin films using fixed wavelength (266nm) for excitation. As seen from PL spectra that all samples exhibit emission bands centered around 470 nm, which can be attributed to the existence of the inter-band gap deep defect levels related to nickel vacancies or interstitial oxygen in the NiO structure [32, 33]. Also, it is clearly seen that the PL spectra are strongly related to the Cu doping level hence the intensity of PL spectra increases with increasing Cu doping concentration. This result confirms the incorporation of Cu^{2+} ions in the NiO lattice as it was reported in the literature [34].

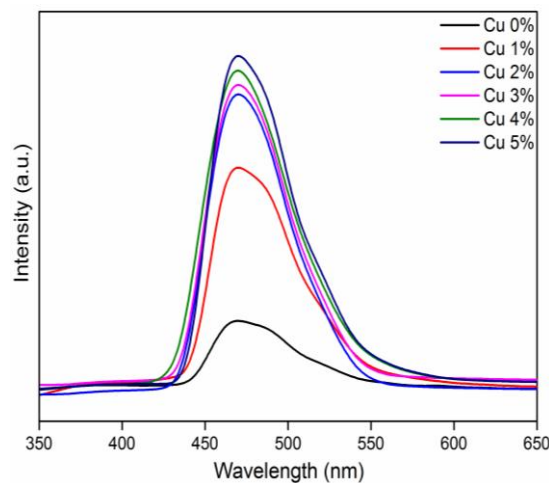


Figure IV.6: Photoluminescence spectra of undoped and Cu-doped NiO thin films.

For more investigation and survey of the energetic levels introduced before and after doping, deconvolution of the spectra was used. Figure IV.7 shows the deconvoluted spectra using Gaussian fitting in wavelength range 350-650nm. Two peaks, in the case of undoped NiO, centered at 469 and 496 nm respectively are observed which are related to (nickel vacancies and/or interstitial oxygen) as discussed above. After doping, in the deconvoluted spectra, an additional peak emission in the visible region around 478 nm was observed. In general, apart from the case of 1% Cu doped NiO, the peak which is around 478nm, slightly

shifts when the Cu doping increases. Similar results are reported in the literature [35, 36]. Area of those peaks, exhibiting the number of defects related to Cu incorporation, increases with Cu increasing. New energy level around 2.59eV below the conduction band is created with Cu incorporation in NiO samples.

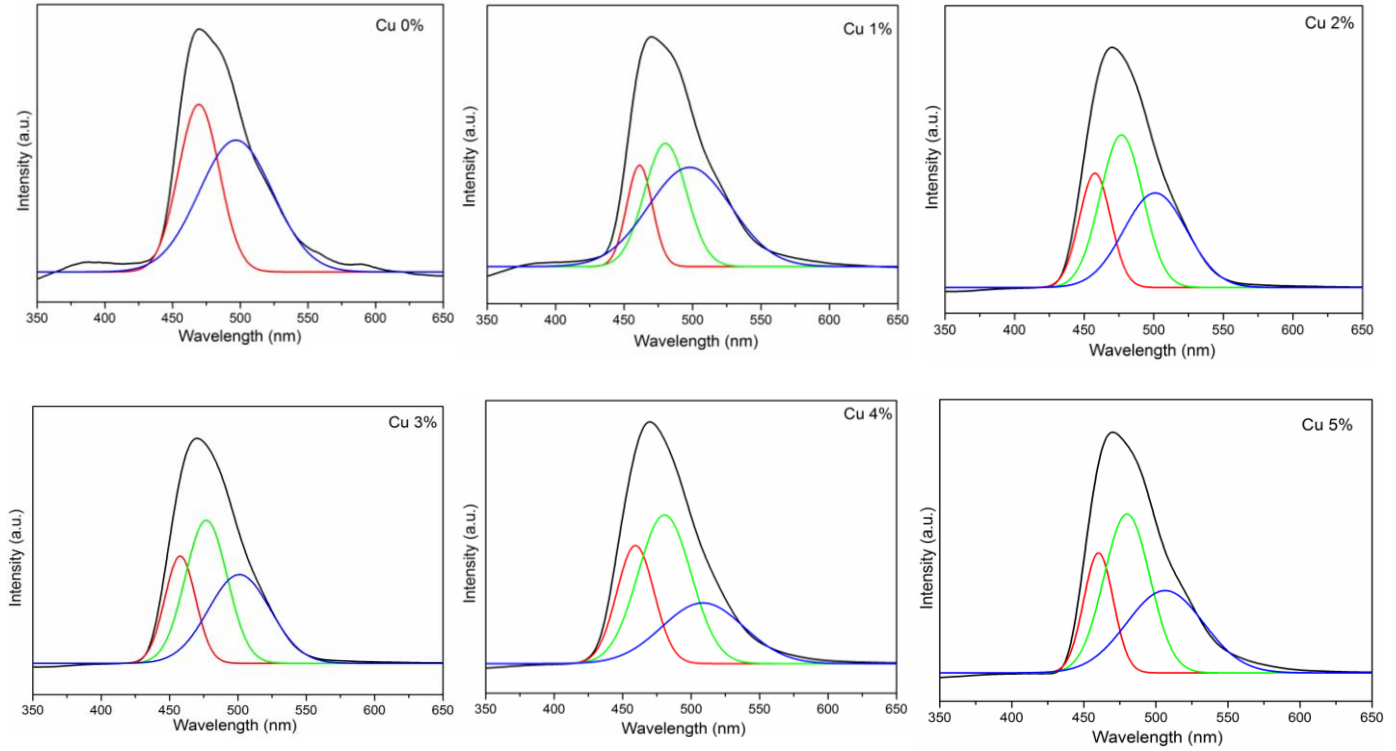


Figure IV.7: Deconvoluted photoluminescence spectra of undoped and Cu-doped NiO thin films.

In Figure IV.8 an energetic diagram is proposed for the three defects related to nickel vacancies, interstitial oxygen and incorporated copper which may be considered as acceptor defect in the band gap of the material. This level may have its effect on the electrical properties as the following paragraph will describe.

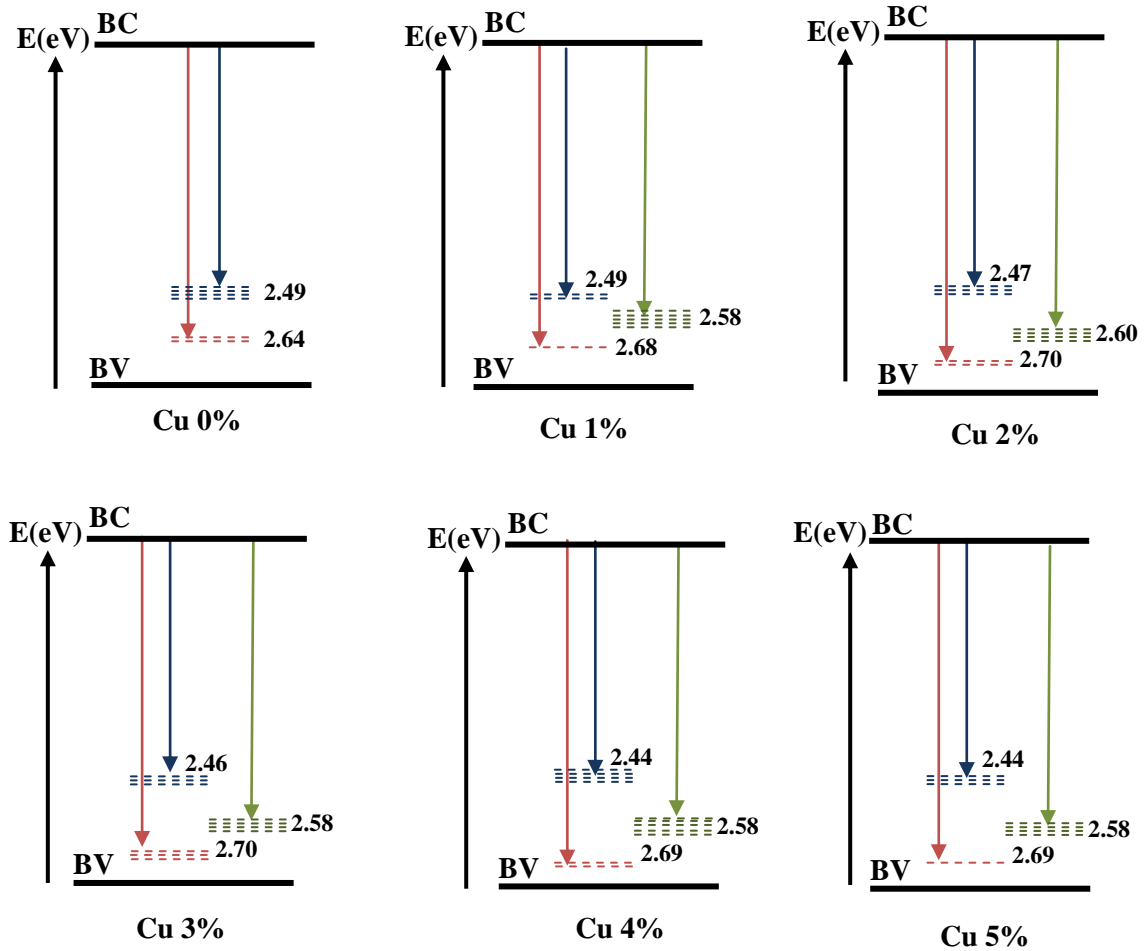


Figure IV.8: Schematic energy level diagram of undoped and Cu-doped NiO thin films.

4.2.4.5 Electrical properties

In order to determine the nature of the NiO films p or n-type semiconductor, hot probe method (Seebeck effect) was examined. A positive sign confirms the p-type conductivity of the deposited samples was observed. Whereas resistivity of NiO films was measured by the four probe method using the following relation [29]:

$$\rho = 4.532 \times \left(\frac{V}{I} \right) \times t = \frac{1}{\sigma} \quad (\text{IV.9})$$

where ρ is the resistivity, V is the measured voltage, I is the current applied, σ is the conductivity and t is the thickness of the film.

Figure IV.9 shows the variation of films conductivity of undoped and Cu doped NiO samples. As can be seen the conductivity of the films increases from 2.3 to $5.9 \times 10^{-2} \Omega^{-1} \cdot \text{cm}^{-1}$, when the Cu doping concentration is increased from 1 to 5wt. % Cu doping. For the undoped sample case, the conductivity ($\sigma = 2.3 \times 10^{-2} \Omega^{-1} \cdot \text{cm}^{-1}$) may be attributed to the presence of microstructural defects existing in NiO crystallites such as nickel interstitials and oxygen

vacancies [37, 38]. But for doped samples, it increases with Cu doping increasing which may be due to the substitution of Ni^{2+} by Cu^{2+} creating more acceptor levels close the valence band edge as it was seen in the PL section study and therefore more electrical conduction as Cu doping level increases [8, 39,40].

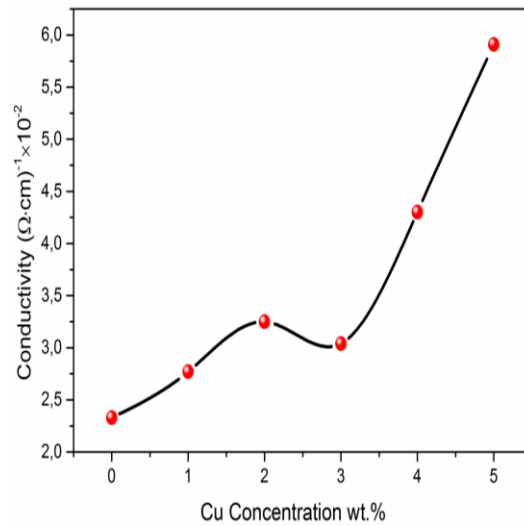


Figure IV.9: Variation of the conductivity of NiO thin films as a function to the copper concentration.

4.3 Effect of Lithium doped NiO thin films

Undoped NiO thin films have drawn much attention in view to their low cost, high transmittance, and low p-type conductivity. The performance of NiO thin films can be adapted and improved by appropriate impurity doping. Due to the great applications of lithium (Li) doped NiO films (an electrode in electrochromic devices, smart windows, and displays, energy storage devices); there is a considerable interest to improve certain physical properties of NiO, such as its transparency and electrical conductivity. In this section, the effect of Li concentration on the structural, optical, photoluminescence, electrical and properties of the deposited NiO films synthesized using spray pyrolysis method.

4.3.1 Experimental procedure

4.3.2 Synthesis of thin films

Undoped NiO and Lithium doped NiO thin films were synthesized using spray pyrolysis. The starting solution was prepared from 0.1 M (Ni (NO₃)₂, 6H₂O) nickel nitrate dissolved in double distilled water. For lithium doping, Lithium chloride (LiCl₂.H₂O) was added to the above solution with appropriate weight ratios of Li to Ni varied from 0 to 20 wt. %. The mixture solution was stirred at 50°C using a magnetic stirrer for half an hour to get a green and homogenous solution. After that, the solution was sprayed onto heated substrates glasses at 500°C. The preparative condition is; the distance between the nozzle and the substrate was kept constant at 45 cm, sprayed flow rate of the solution was taken 2 ml/min, spray time took 10s separated by 10s as the time interval of stay to maintain the heat of substrates constant. The glass substrates types are (R217102) microscopic glass slide in size of (75×25×1.1 mm³). Before deposition process, a standard cleaning of substrates was kept as follow: rinsing in acetone and distilled water respectively for 10min, and then blowing dry with a compressed air. After deposition, the films were allowed to cool to room temperature.

4.3.3 Thin films characterization

The structural properties of prepared thin films were investigated using X-ray diffraction (BRUKER-AXS type D8) equipped with X'Pert High Score under Cu K α ($\lambda=1.5406\text{\AA}$) radiation in the range of 20° and 70°. The functional group present in the sample was recorded using Fourier transformed infrared spectroscopy (FTIR-Perkin Elmer Spectrum 1000), the Scan of the FTIR measurements is performed over the range between 400-4000 cm⁻¹. The optical transmission spectra were carried out by using UV-Vis

spectrophotometer (Shimadzu, Model 1800) in the wavelength range 300–900 nm. For PL measurements, the excitation wavelength was fixed at 266 nm. The electrical conductivity of the films was measured with Keithley Model 2400 low voltage source meter instrument. Film thickness (t) was measured by using weight difference method considering the density of the bulk nickel oxide.

4.3.4 Result and discussions

4.3.4.1 Structural properties

Figure IV.10 shows the XRD patterns of undoped NiO and Li-doped NiO thin films with different Li doping concentration. As seen there are three main diffraction peaks positioned at $2\theta = 37.2^\circ$, 43.3° and 62.8° assigned to the (111), (200) and (220) crystal planes respectively. These peaks correspond precisely to the NaCl crystalline structure of NiO and matched well with the standard spectrum (JCPDS, No.47-1049) under the space group $Fm\bar{3}m$ (225) [41]. The presence of such peaks indicates that the films are polycrystalline in nature. From the XRD analysis, no secondary phase that corresponds to Li or their oxides can be observed, which imply that the diffraction pattern affirms that the all samples are single phase. Similar results are reported by *I. Sta et. al*, they explained the absence of lithium atoms in NiO structure indicates that incorporated in the NiO lattice [42]. The intensity of (111) diffraction peak is higher compared with other observed peaks indicating the preferred orientation. Furthermore, we can clearly see from the inset of Figure IV.11 that the position of the diffraction peaks with increasing Li concentration did not change significantly, which could be due to the comparable ionic radius of Li^+ (0.68 Å) and Ni^{2+} ion (0.69 Å)[43].

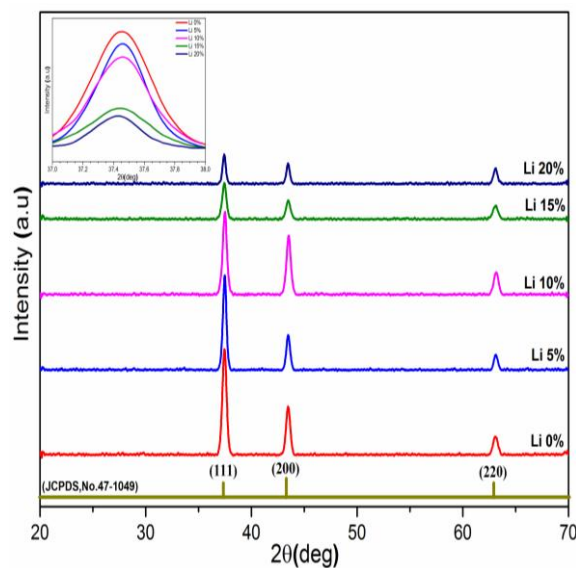


Figure IV.10: X-ray patterns of undoped and Li-doped NiO thin films variation of diffraction intensity in the range 2θ (37–38) corresponding to the (111) peak for undoped and Li-doped NiO thin films.

From the XRD patterns, we can see that the intensity of the (111) peak slowly decreases as the Li doping concentration increases, this behavior indicating a decrease in the crystallinity of the films.

The lattice parameter a of the deposited films were evaluated from the values of 2θ and inter-planar spacing relation for the cubic structure, as given below [44]:

$$\frac{1}{d_{hkl}^2} = \frac{h^2 + k^2 + l^2}{a^2} \quad (\text{IV.10})$$

where d_{hkl} is inter-planar spacing, (hkl) are the Miller indices of the planes taken in consideration.

The mean strain ε developed in the prepared NiO thin films was evaluated using the next formula [45]:

$$\varepsilon = \left(\frac{a - a_0}{a_0} \right) \times 100\% \quad (\text{IV.11})$$

where ε is the mean strain, a is the lattice constant of NiO thin films and a_0 the standard lattice constant of bulk material ($a_0 = 4.1769 \text{ \AA}$) similar to standard card (JCPDS, No. 47-1049).

The average crystallite size G was calculated from Debye-Scherrer formula [46]:

$$G = \frac{0.9\lambda}{\beta \cos \theta} \quad (\text{IV.12})$$

Where β is the full width at half-maximum (FWHM) of the most intense diffraction peak, λ is the X-ray wavelength (1.54056 \AA) and θ is the Bragg angle at (111) peak.

The calculated values, deduced from (111) plane, of lattice constant a , mean strain ε and crystallite size G of the NiO thin films with variation of Li doping concentration are listed in TableIV.3.

Li Concentration wt.(%)	2θ (deg)	Lattice constant (\AA)		Crystallite size (nm)	Mean strain ε (%)
		a	$\Delta a = a - a_0$		
0	37.467	4.156	-0.0199	30.86	-0.478
5	37.464	4.159	-0.0176	22.82	-0.422
10	37.444	4.154	-0.0222	23.81	-0.533
15	37.451	4.157	-0.0190	17.99	-0.457
20	37.433	4.162	-0.0140	26.41	-0.337

Table IV.3: Values of Bragg angle 2θ , lattice constants a , crystallite size D and mean strain ε for the (111) plane of NiO thin films as a function to the Li concentration.

The obtained results indicate that the lattice constant change from 4.156 \AA in undoped NiO films to 4.162 \AA as Li concentration increases from 5 to 20 wt.%, this may be referred to the substitution of Ni^{2+} sites by Li^+ ions in the NiO lattice, we note that all values of lattice

constant is smaller than to the bulk standard a_0 of NiO, which proves the presence of internal strain and defects in the films as it seen from Table IV.3 and confirm the previous discussion [47]. The values of the average crystallite sizes are found to be varied from 30.86 to 17.99 nm as increasing of Li doping concentration from 0 to 20 wt.% as it observed from Figure IV.11. These results improve the effect of Li doping in the crystallinity of the NiO films.

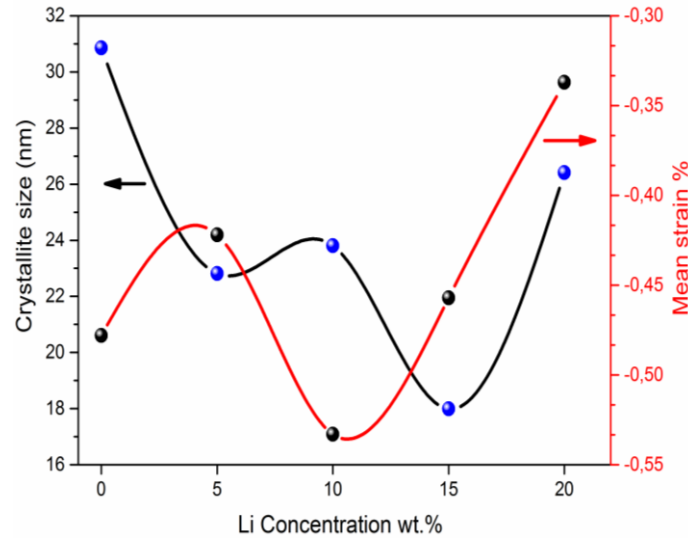


Figure IV.11: Variation of crystallite size and mean strain size of NiO thin films as a function to the Li concentration.

4.3.4.2 Fourier Transform Infrared (FT-IR) analysis

FT-IR transmission spectrum of the undoped and Li-doped NiO thin film prepared at 500°C in the range between 400 and 4000 cm^{-1} is shown in Figure IV.12. The existence of absorption bands depends on crystal structure and chemical composition [48]. The absorption band positioned at 688 cm^{-1} appeared in the all samples is correlated to the Ni-O stretching vibration mode [49]. Broad absorption band in the region of 850-986 cm^{-1} corresponds to metal-oxygen (Ni-O) vibrational modes; (Metal oxides generally give absorption bands below 1000 cm^{-1} arising from inter-atomic vibrations, the broadness of the absorption band indicates that the NiO thin films are nanocrystals as confirmed through the XRD results [50]. With the increases of Li concentration from 5 to 20 wt. %, we can observe absorption peak located at 1160 cm^{-1} , this peak is assigned to the presence of lithium oxide (LiO_2) bond vibrational modes [51].

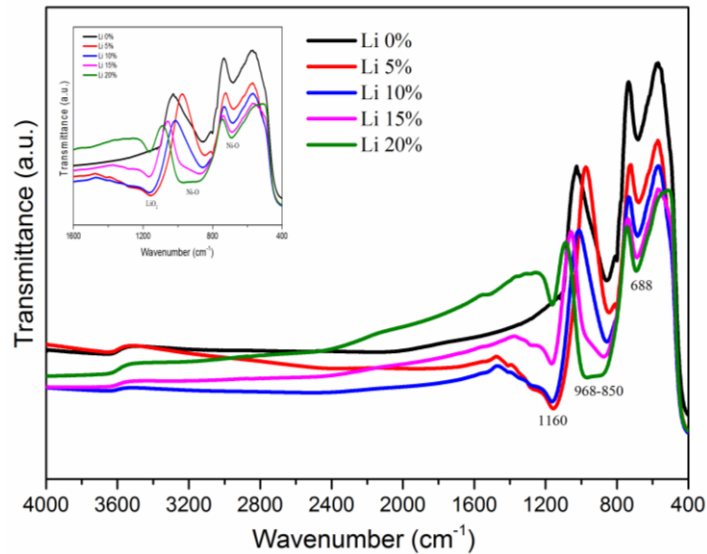


Figure IV.12: FT-IR spectra of undoped and Li-doped NiO thin films

4.3.4.3 Optical properties

The optical transmission spectra of undoped and NiO: Li thin films in the wavelength range 300-900 nm using UV-Vis spectroscopy are shown in Figure IV.13. As can be seen, the prepared films exhibit high transparency into the visible range with an average transmittance varied between 70% and 87%. This indicates a good optical quality as a result of low scattering or absorption losses. From Figure IV.13, the average transmission value exhibits the most transparent for undoped NiO film, which is around 87% in the visible wavelength range.

However, we can view that with the increase of Li concentration from 5 to 20 wt. % there is a decrease in the optical transparency. The reason of decreasing transmittance refers to the variations in the film thickness, Li doping concentration and defect structure, which in turn decreased the optical transmittance; similar results were confirmed by the many researchers [52, 53]. In the wavelength region between 300 and 360 nm, it was observed that all samples have sharp absorption edges, this because of the transition between valence and conduction bands due to onset fundamental absorption.

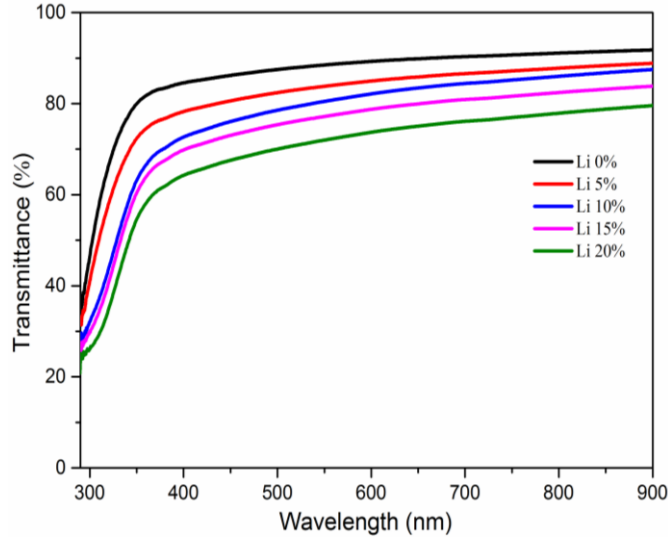


Figure IV.13: Transmittance spectra of undoped and Li-doped NiO thin films.

The absorption coefficient can be calculated according to the optical transmission transmittance T values and thickness t at the absorption edge using Lambert's formula [54]:

$$\alpha = \frac{1}{t} \ln \left(\frac{1}{T} \right) \quad (\text{IV.13})$$

In the case of a direct transition, the optical band gap energy E_g is giving by the following Tauc's relation [55]:

$$\alpha h\nu = A(h\nu - E_g)^{\frac{1}{2}} \quad (\text{IV.14})$$

where A is a constant, α is the absorption coefficient, $h\nu$ is the photon energy and E_g is the band gap energy. The band gap has been estimated by extrapolating the linear region of the plots $(\alpha h\nu)^2$ versus $h\nu$ on the energy axis as shown in Figure IV.14. The calculated values of E_g are represented in Table IV. 4. The value of band gap E_g is 3.88 eV for undoped NiO film, whereas the value of E_g gradually decreases from 3.84 to 3.57 eV for samples prepared as of Li doping concentration increased from 5 to 20 wt.%. This was in good accord with the earlier reports on the band gap of NiO films from 3.4 eV to 4.0 eV by different research groups [56, 57]. The band gap is found to decrease with an increase in the Li doping concentration; this suggests a change in the NiO electronic structure. This may refer to the crystallite growth, defects or vacancies in the NiO crystal which can create new energy level. This behavior leads to the reduction in the band gap energy [58, 59].

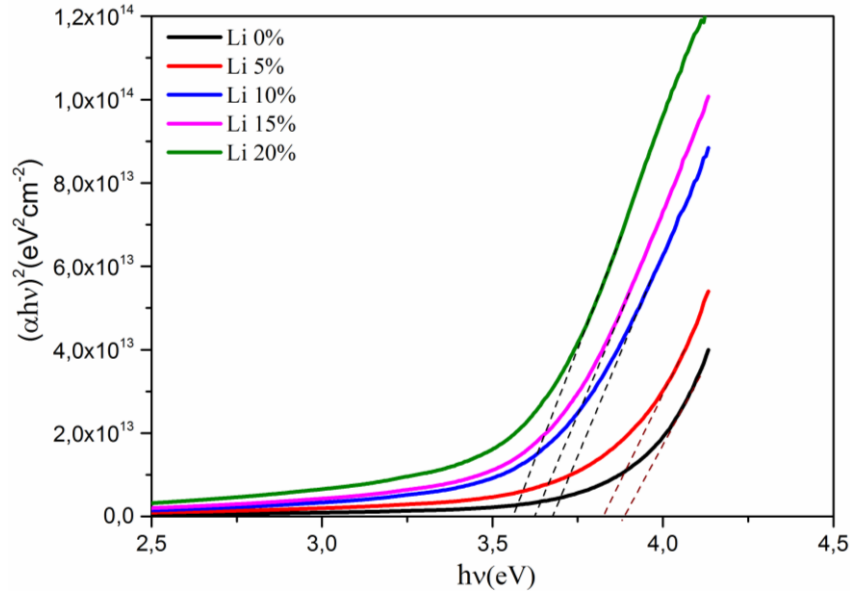


Figure IV.14: Estimation of band gap energy (E_g) from Tauc's relation of undoped and Cu-doped NiO thin films.

The absorption coefficient α near the band edge shows an exponential dependence on photon energy called Urbach energy, which gives the width of the tails of the localized states within the optical band gap. This dependence is given by the following relation [31]:

$$\alpha = \alpha_0 \exp\left(\frac{h\nu}{E_u}\right) \quad (\text{IV.15})$$

where α_0 is a constant, $h\nu$ is the photon energy and E_u is the Urbach energy which refers to the width of the exponential absorption edge. The estimated E_u values are found to be averaged between 325.73 and 422.27 meV as Li doping concentration increases from 0 to 20 wt.% as shown in Figure IV.15. The E_u value is comparatively high for samples doped with Li. the incorporation of Li ions causes an increase in disorder and defects in the Li-doped NiO thin films. The presence of a band tail implies that the structural inhomogeneous and disorder are important.

Li concentration (wt.%)	Thickness t (nm)	Optical gap energy E_g (eV)	Urbach energy E_u (meV)	Resistivity ρ (Ω .cm)
0	102	3.88	325.73	$6.7 \cdot 10^8$
5	114	3.84	351.49	$5.2 \cdot 10^8$
10	125	3.67	387.14	$3.4 \cdot 10^7$
15	131	3.62	401.14	$2.1 \cdot 10^7$
20	138	3.57	422.47	$1.6 \cdot 10^6$

Table IV.4: Values of thickness t , optical band gap energy E_g , Urbach energy E_u and resistivity ρ of NiO thin films as a function to the Li concentration.

From Table IV.4 we can observe that E_u and E_g values correlate very well; it is clear that the E_g values are opposite to the disorder's variation. Li doping produces localized states within

the forbidden band gap. As a result, both a decrease in the E_g and an expansion of the Urbach tail occurred. This behavior means that the obtained optical band gaps are governed essentially by the disorder variations in such films.

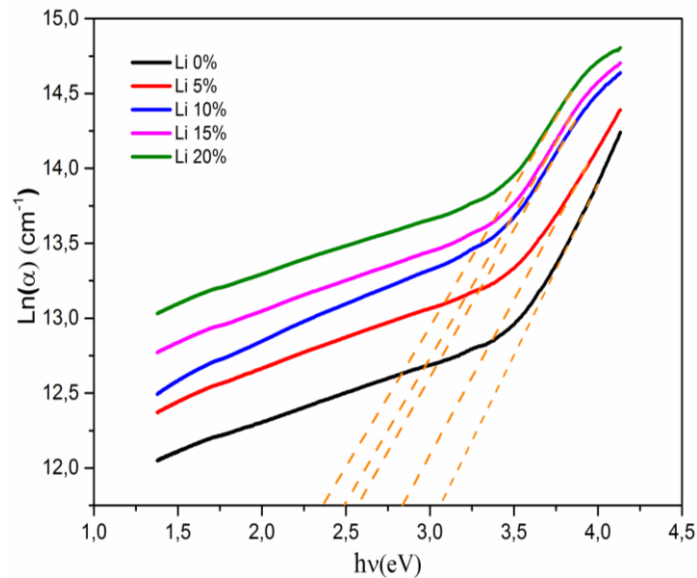


Figure IV.15: Estimation of Urbach energy (E_u) of undoped and Li-doped NiO thin films.

4.3.4.3 Photoluminescence studies

To get more information about defaults inside NiO thin film, the room temperature photoluminescence (PL) spectroscopy was achieved in the wavelength, between 300-600 nm using 266nm wavelength excitation. Figure IV.16 shows PL spectra of undoped and Li-doped NiO thin films. Figure IV.16 shows PL spectra of undoped and Li-doped NiO thin films. Two peaks located at 416 and 443 nm in the all samples corresponding to the presence of nickel vacancies and/or interstitial oxygen [60], Mochizuki et al. [33] reported that nickel vacancies can occur for the reason of charge transfer between Ni^{2+} and Ni^{3+} . it is noted that the vacancy thus created increase the defect levels in the NiO crystal and hence enhances the visible emission in the PL spectra. Furthermore, from the same figure, it can be seen that Li-doped NiO samples showed high PL intensities compared with intensities of undoped NiO films. Change in the intensities confirmed the dependence of PL intensities with the doping concentration.

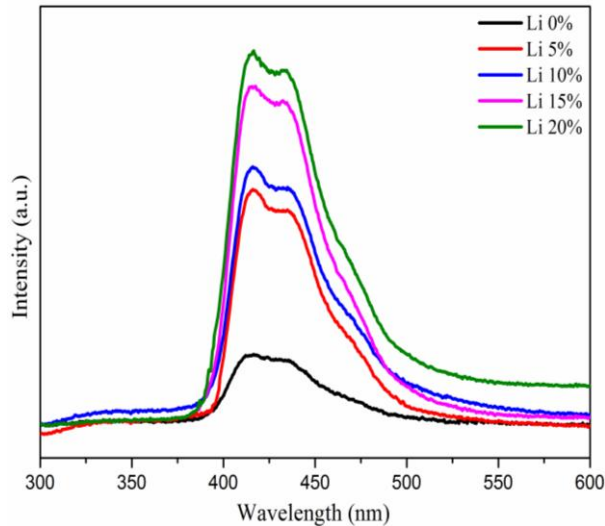
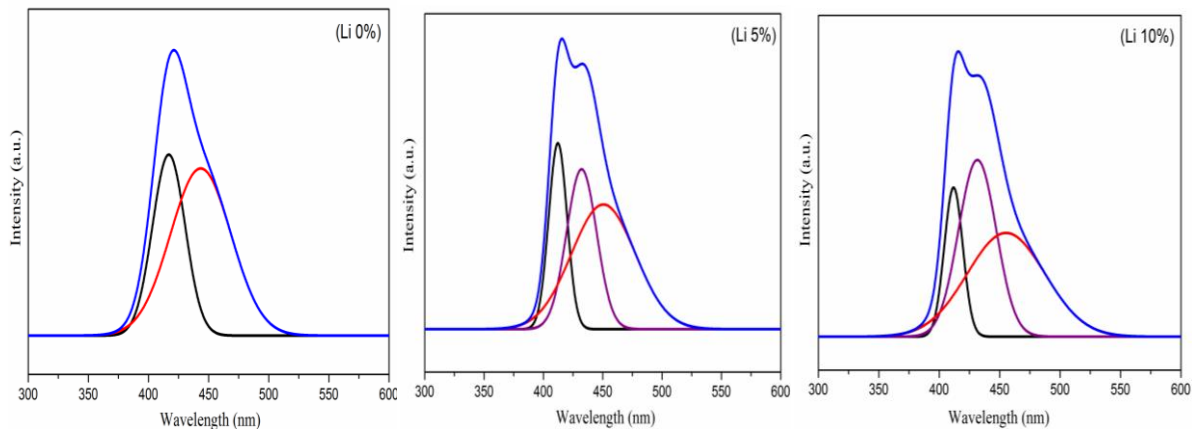


Figure IV.16: Photoluminescence spectra of undoped and Li-doped NiO thin films.

A deconvolution analysis was performed to interpret the effect of Li doping and give an idea about the approximate peak position and the number of emission bands present in the whole spectrum in NiO structure. Figure IV.17 shows the deconvoluted spectra using Gaussian fitting in wavelength range 300-600nm. In the case of undoped NiO, two emission peaks in the violet region including 416 and 443 nm respectively are observed which are related to (nickel vacancies and/or interstitial oxygen) as discussed above. The appearance of additional emission peak in the visible region around 432 nm was observed after doping with lithium and shifted to 437 nm; these results confirm incorporation of Li ions in the NiO crystal. Furthermore, the analyses of the area of those peaks who present the number of defects related to the NiO structure were observed increases with increasing of Li concentration.



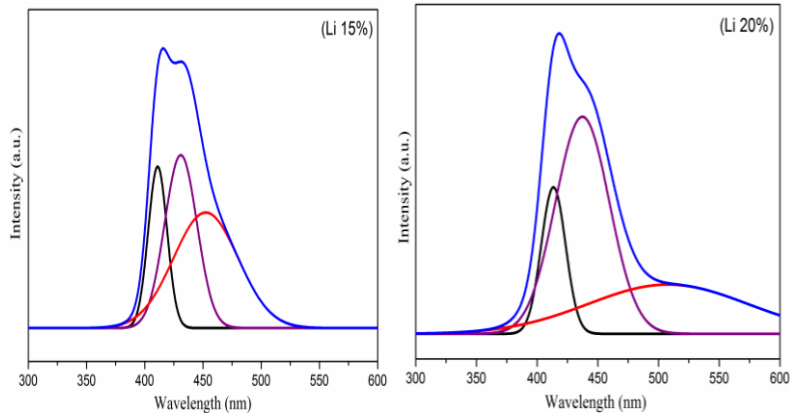


Figure IV.17: Deconvoluted photoluminescence spectra of undoped and Li-doped NiO thin films.

Figure IV.18 represent the energetic diagram of proposed for the three defects related to nickel vacancies, interstitial oxygen and incorporated lithium which give details about the previous discussion. From the results obtained, it is clear that the Li doping plays a vital responsibility in modifying the optical properties of the NiO materials. These results show that lithium doped NiO films have an important application potential for optoelectronic devices such as solar cells, electrochromic display devices, smart windows, lasers and luminescent materials,... etc.

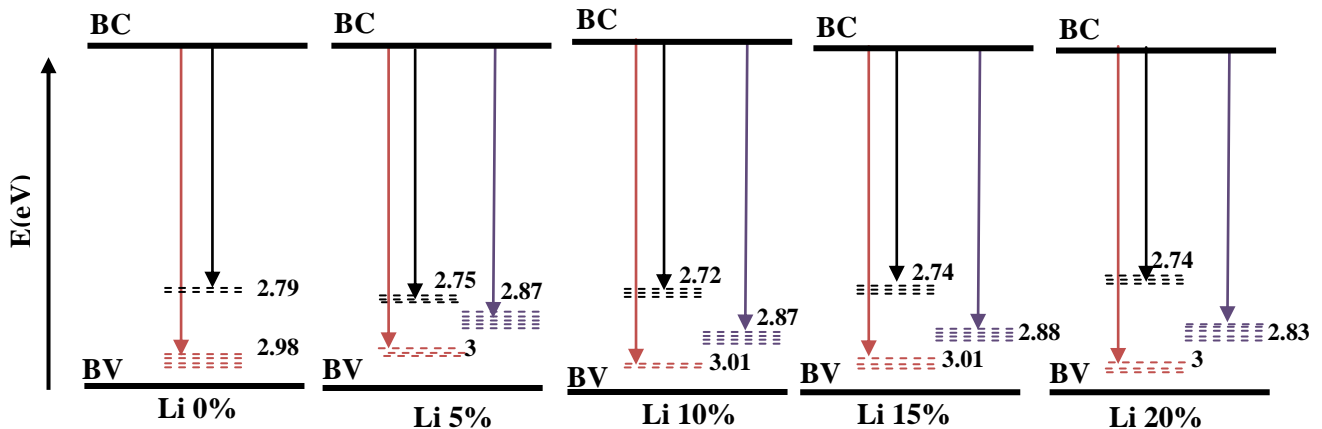


Figure IV.18: Schematic energy level diagram of undoped and Li-doped NiO thin films.

4.3.4.4 Electrical properties

The two hot probe (Seebeck effect) techniques were used to evaluate the nature of the material being studied. From the sign of voltage, it has been found that all the samples exhibit p-type conductivity. This indicates that nickel vacancies are responsible for conduction. Figure IV.19 shows the change in resistivity as a function of lithium concentration. It was found that the resistivity decreased from $6.7 \cdot 10^8$ to $1.6 \cdot 10^6$ ($\Omega \cdot \text{cm}$) as the Li content was increased. Undoped NiO thin films usually exhibit p-type semiconductor and the electrical conduction is associated with presence of nickel vacancies and/or interstitial oxygen, which

implies the formation of Ni^{3+} ions in the NiO crystal [61]. after doping with Li the resistivity of the NiO films decreased, this results may be referred that the incorporation of Li^+ ions in NiO crystal contribute to the conduction and creation of new acceptor levels near the valence band, this behavior confirmed with previous PL study, which the area of the peaks increases after doping as lithium doping concentration increases [62].

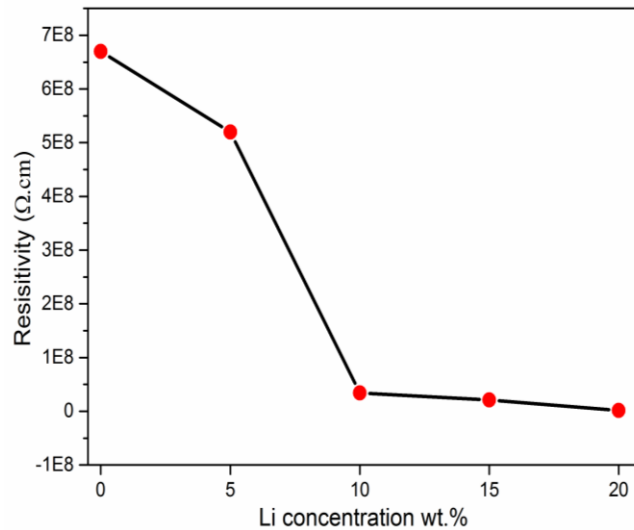


Figure IV.19: Variation of the resistivity of NiO thin films as a function to the Li concentration.

References

- [1] B.Sasi, Preparation and characterization studies of nanostructured nickel oxide and lithium doped nickel oxide thin films, PhD thesis, University of Kerala, 2007.
- [2] A. Shareef Ahmed, Structural optical and electrical properties of some metal oxide nanomaterials, PhD thesis, Aligarh Muslim University, 2013.
- [3] Yan Li ,Xinhai Li, Zhixing Wang ,Huajun Guo,Tao Li, One-step synthesis of Li-doped NiO as high-performance anode material for lithium ion batteries, *Ceramics International* 42(2016) 14565–14572.
- [4] Ahmed Alshahrie, I.S. Yahiac, Atteiah Alghamdi , P.Z. Al Hassan, Morphological, structural and optical dispersion parameters of Cd-doped NiO nanostructure thin film, *Optik* ,127(2016) 5105–5109.
- [5] J. Shi, L. Lai, P. Zhang, H. Li, Y. Qin, Y. Gao, L. Luo, J. Lu, Aluminum doped nickel oxide thin film with improved electrochromic performance from layered double hydroxides precursor in situ pyrolytic route, *Journal of Solid State Chemistry*, 241(2016)1–8.
- [6] N. Wang, C.Q. Liu, C.Q. Liu, B. Wen, H.L. Wang, S.M. Liu, W.W. Jiang, W.Y. Ding, W.P. Chai, Structural, electrical and optical properties of K-doped NiO films prepared by rapid pyrolysis sol-gel technique, *Thin Solid Films* ,616 (2016) 587–593.
- [7] C. Mrabet, M. Ben Amor, A. Boukhachem, M. Amlouk, T. Manoubi, Physical properties of La-doped NiO sprayed thin films for optoelectronic and sensor applications, *Ceramics International*, 42 (2016) 5963–5978.
- [8] S.C. Chen, T.Y. Kuo, Y.C. Lin, H.C. Lin, Preparation and properties of p-type transparent conductive Cu-doped NiO films, *Thin Solid Films*, 519 (2011) 4944–4947.
- [9] V. Patil, S. Pawar, M. Chougule, Effect of annealing on structural, morphological, electrical and optical studies of nickel oxide thin films, *Journal of Surface Engineering Materials and Advanced Technology*, 1 (2011) 35.
- [10] K. Martin, G. McCarthy: North Dakota State Univ., Fargo, ND, USA, ICDD Grant-in-Aid, 1991.
- [11] S. C. Chen , T. Y. Kuo , Y. C. Lin , C. L. Chang, Preparation and properties of p-type transparent conductive NiO films, *Advanced Materials Research* , 123 (2010) 181-184.
- [12] M. Yang, Z. Shi, J. Feng, H. Pu, G. Li, J. Zhou, Q. Zhang, Copper doped nickel oxide transparent p-type conductive thin films deposited by pulsed plasma deposition, *Thin Solid Films*, 519 (2011) 3021–3025.
- [13] S. Moghe , A.D. Acharya , R. Panda , S.B. Shrivastava , M. Gangrade ,T. Shripathi , V. Ganesan, Effect of copper doping on the change in the optical absorption behaviour in NiO thin films, *Renewable Energy*, 46 (2012) 43-48.
- [14] H. L. Chen, Y. M. Lu ,W. S. Hwang, Effect of film thickness on structural and electrical properties of sputter-deposited nickel oxide films', *Mater. Trans.*, 46(2005) 872–879.
- [15] B. D. Cullity, *Elements of X-ray diffraction*, Addison-Wesley, Reading, MA, (1987) 294.
- [16] S. Benramache, B. Benhaoua, Influence of substrate temperature and Cobalt concentration on structural and optical properties of ZnO thin films prepared by ultrasonic spray technique, *Superlattices and Microstructures*, 52(2012) 807.

- [17] G. B. Williamson, R. C. Smallman, Dislocation densities in some annealed and cold-worked metals from measurements on the X-ray debye-scherrer spectrum, *Philos. Mag.* 1, 34 (1956).
- [18] R. Cerc Koros̆ec, P. Bukovec, B. Pihlar, A. Šurca Vuk, B. Orel, G. Draz̆ic̆, Preparation and structural investigations of electrochromic nanosized NiOx films made via the sol–gel route, *Solid State Ionics*, 165 (2003) 191–200.
- [19] B. Subramanian, M. Mohamed Ibrahim, V. Senthilkumar, K. R.Murali, VS. Vidhya, C. Sanjeeviraja, M. Jayachandran, Optoelectronic and electrochemical properties of nickel oxide(NiO)films deposited by DC reactive magnetrons puttering, *Physica B*, 403(2008)4104–4110.
- [20] N. R. Dhineshababu, V. Rajendran, N. Nithyavathy, R. Vetumperumal, Study of structural and optical properties of cupric oxide nanoparticles, *Applied Nanoscience* , 6 (2016) 933–939.
- [21] S. Gandhi, R. Hari Hara Subramani, T. Ramakrishnan , A. Sivabalan , V. Dhanalakshmi ,M. R. Gopinathan Nair, R. Anbarasan, Ultrasound assisted one pot synthesis of nano-sized CuO and its nanocomposite with poly(vinyl alcohol), *J Mater Sci* , 45 (2010) 1688–1694.
- [22] K. S. Usha, R. Sivakumar, C. Sanjeeviraja, Optical constants and dispersion energy parameters of NiO thin films prepared by radio frequency magnetron sputtering technique, *Journal Of Applied Physics*, 114 (2013) 123501-123510.
- [23] S. Benramache, B. Benhaoua, Influence of annealing temperature on structural and optical properties of ZnO:In thin films prepared by ultrasonic spray technique, *Superlattices and Microstructures*, 52(2012) 1062.
- [24] J. Tauc, *Amorphous and Liquid Semiconductors*, Plenum Press, New York, 1974.
- [25] E. Avendaño, L. Berggren, G.A. Niklasson, C.G. Granqvist, A. Azens, Electrochromic materials and devices: brief survey and new data on optical absorption in tungsten oxide and nickel oxide films, *Thin Solid Films*, 496 (2006) 30.
- [26] M. Ben Amor, A. Boukhachem, K. Boubaker, M. Amlouk, Structural, optical and electrical studies on Mg-doped NiO thin films for sensitivity applications, *Materials Science in Semiconductor Processing*, 27 (2014) 994–1006.
- [27] B.S. Reddy, S.V. Reddy, N.K. Reddy, J.P. Kumari, Synthesis, structural, optical properties and antibacterial activity of co-doped (Ag, Co) ZnO nanoparticles, *Res. J. Mater.Sci.* 1 (2013) 11-20.
- [28] A.I. Oliva, O.S. Canto, R.C. Rodrigues, P. Quintana, Formation of the band gap energy on CdS thin films growth by two different techniques, *Thin Solid Films* 391 (2001) 28-35.
- [29] CR. Bamford, *Colour generation and control in glass*, Glass science & technology, Amsterdam, the Netherlands, Elsevier, 1977.
- [30] G. D. Cody, T. Abeles, B. Brooks, B. Goldstein, Disorder and the Optical-Absorption Edge of Hydrogenated Amorphous Silicon, *Phy. Rev. Lett.*, 47(1981) 1480.
- [31] F. Urbach, the longwavelength edge of photographic sensitivity and of the electronic absorption of solids, *Phys. Rev.*, 92 (1953) 1324-1325.

- [32] Jang, W. L., Lu, Y. M., Hwang, W. S., Hsiung, T. L., Wang, H. P., Point defects in sputtered NiO films, *Appl. Phys. Lett.*, 94(2009) 062103-06216.
- [33] S. Mochizuki, T. Saito, Intrinsic and defect related luminescence of NiO, *Physica B*, 404 (2009) 4850-4853.
- [34] Y. Qi, H. Qi, C. Lu, Y. Yang, Y. Zhao, Photoluminescence and magnetic properties of β -Ni(OH)₂ nanoplates and NiO nanostructures. *J. Mater. Sci.: Mater. Electron.* 2008, 20, 479-483.
- [35] M.V. Kumar, S. Muthulakshmi, A.A. Paulfrit, J. Pandiarajan, N. Jeyakumaran, N. Prithivikumaran, Structural and optical behaviour of thermally evaporated p-type nickel oxide thin film for solar cell applications, *Int. J. Chem. Tech. Res.*, 6(2014) 5174-7.
- [36] M.H. Zhou, J.G. Yu, S.W. Liu, P.C. Zhai, L. Jiang, Effects of calcination temperatures on photocatalytic activity of SnO₂/TiO₂ composite films prepared by an EPD method, *J. Hazard. Mater.* 154 (2008) 1141–1148.
- [37] S. Benramache, A. Rahal, B. Benhaoua, The effects of solvent nature on spray-deposited ZnO thin film prepared from Zn (CH₃COO)₂, 2H₂O, *Optik*, 125 (2014) 663– 666.
- [38] S. Nandy, B. Saha, M. K. Mitra, K. K. Chattopadhyay, Effect of oxygen partial pressure on the electrical and optical properties of highly (200) oriented p-type Ni_{1-x}O films by DC sputtering, *Journal of Materials Science*, 42(2007) 5766.
- [39] M. Jlassi, I. Sta, M. Hajji, H. Ezzaouia, Optical and electrical properties of nickel oxide thin films synthesized by sol–gel spin coating, *Materials Science in Semiconductor Processing*, 21(2014) 7–13.
- [40] H.L. Chen, Y.M. Lu, W. S. Hwang, Thickness dependence of electrical and optical properties of sputtered Nickel oxide films, *Thin Solid Films*, 514 (2006) 361–365.
- [41] M. El-Kemary, N. Nagy, I. El-Mehasseb, Nickel oxide nanoparticles: Synthesis and spectral studies of interactions with glucose, *Mat. Sci. Semi. Proc.*, 16(2013) 1747-1752.
- [42] I. Sta, M. Jlassi, M. Kandyala, M. Hajji, P. Koralli, R. Allagui, M. Kompitsas, H. Ezzaouia, Hydrogen sensing by sol–gel grown NiO and NiO:Li thin films, *Journal of Alloys and Compounds*, 626(2014) 87-92.
- [43] E. Martins, S.L. baldochi, S.P. Morato, N.D. Vieira Junior, A. Luci, M. Casalboni, U.M. Grassano, G. Baldacchini, M.Cremona, R.M. Montereali, E.Krausz, M.Riley, Fine structure of the absorption and emission spectra of Ni²⁺-ions in BALiF₃, *Radiation Effects and Defects in Solids*, 135 (1995)15-18.
- [44] A. Boukhachem, R. Boughalmi, M. Karyou, A. Mhamdi, K. Boubaker, M. Amlouk, R. Chtourou, Study of substrate temperature effects on structural, optical, mechanical and opto-thermal properties of NiO sprayed semiconductor thin films, *Materials Science and Engineering B*, 188 (2014) 72-77.
- [45] S. Benramache, F. Chabane, B. Benhaoua, F.Z. Lemmadi, Influence of growth time on crystalline structure, conductivity and optical properties of ZnO thin films, *Journal of semiconductors*, 34(2013) 023001.
- [46] P.Scherrer, *Nachr. Ges.Wiss. Göttingen*, 26 (1918) 98.
- [47] M. Krunk, J. Soon, T. Unt, A. Mere, V. Mikli, Deposition of p-type NiO films by chemical spray pyrolysis, *Vacuum*, 107(2014) 242-246.

- [48] F.A. Sigoli, M.R. Davalos, M.J. Jafelicci, Morphological evolution of zinc oxide originating from zinc hydroxide carbonate, *J Alloys Compd*, 262 (1997) 292-295.
- [49] H. Qiao, Z. Wei, H. Yang, LZhu, X. Yan, Preparation and Characterization of NiO Nanoparticles by Anodic Arc Plasma Method, *Journal of Nanomaterials* 2009 (2009)1-5.
- [50] C. N. R Rao, *Chemical Applications of Infrared Spectroscopy*, Academic Press, NewYork and London (1963).
- [51] L. Andrews, Infrared Spectrum, Structure, Vibrational Potential Function, and Bonding in the Lithium Superoxide Molecule LiO_2 , *the Journal of Chemical Physics*, 50 (1969) 4288.
- [52] D.P. Joseph, M. Saravanan, B. Muthuraaman, P. Renugambal, S. Sambasivam, S. Philip Raja1, P Maruthamuthu, C Venkateswaran, Spray deposition and characterization of nanostructured Li doped NiO thin films for application in dye-sensitized solar cells, *Nanotechnology* 19 (2008) 485707.
- [53] W.Chia-Ching, Y. Cheng-Fu, Investigation of the properties of nanostructured Li-doped NiO films using the modified spray pyrolysis method, *Nanoscale Research Letters*, 8(2013)33.
- [54] J.P. Borah, K.C. Sarma, *Acta Phys. Pol. A*, Optical and Optoelectronic Properties of ZnS Nanostructured Thin Film, 114 (2008) 713-719.
- [55] J. Tauc, *the Optical Properties of Solids*, Academic Press, New York, 1966.
- [56] I.A. Gardunõ, J. C. Alonso, M. Bizarro, R. Ortega, L. Rodríguez-Fernández, A. Ortiz, Optical and electrical properties of lithium doped nickel oxide films deposited by spray pyrolysis onto alumina substrates, *Journal of Crystal Growth*, 312(2010)3276–3281.
- [57] X. Chen, L. Zhao, Q. Niu, Electrical and Optical Properties of p-Type Li, Cu-Codoped NiO Thin Films, *journal of electronic materials*, 41(2012) 3382–3386.
- [58] P. A. Sheena, K. P. Priyanka, N.A. Sabu, B. Sabu, T. Varghese, Effect of calcination temperature on the structural and optical properties of nickel oxide nanoparticles, *Nanosystems: physics, chemistry, mathematics*, 5 (2014) 441–449.
- [59] U.S. Joshi, K. Itaka, Y. Matsumoto, H. Koinuma, Combinatorial fabrication and magnetic properties of homoepitaxial Co and Li co-doped NiO thin-film nanostructures, *Journal of Magnetism and Magnetic Materials* 321(2009) 3595–3599.
- [60] K. Anandan, V.Rajendran, Structural, optical and magnetic properties of well-dispersed NiO nanoparticles synthesized by CTAB assisted solvothermal process, *Nonosci. Nanotechnol.:Int. J.*, 2 (2012) 24-29.
- [61] T. Dutta, P. Gupta, A. Gupta, J. Narayan, Effect of Li doping in NiO thin films on its transparent and conducting properties and its application in heteroepitaxial p-n junctions, *Journal of Applied Physics*, 108 (2010) 083715.
- [62] I. Sta, M. Jlassi, M. Kandyla, M. Hajii, P. Koralli, R. Allagui, M. Kompitses , H. Ezzaouia, Hydrogen sensing by sol-gel grown NiO and NiO:Li thin films, *Journal of alloys and compound*, 626(2015) 87-92.

*Summary and
Conclusion*

Summary and conclusion

In this thesis, spray pyrolysis techniques (SPT) have been chosen to deposit NiO films on glass substrate. Optimization of different parameters in spray pyrolysis method can be done by variation of substrate temperature, the volume of the solution, molarity, distance nozzle, and substrate, in order to produce thin films with good quality. The prepared films have been done using; DRX, UV-Vis, FTIR, PL, and four probes method. The examine parameters in this study were; solvents nature, precursor concentration and volume of solution.

In other hands to improve several physical properties of NiO thin films like transparency, conductivity, defect structure, Incorporation of doping using metal element is effective method to modify the physical properties of thin films. During this study investigation, the effects of copper (Cu) and lithium (Li) doping concentration on, structural, compositional, optical, photoluminescence and electrical properties of NiO thin films elaborated using SPT method will be studied.

We present a brief summary of our findings discussed in earlier chapters and enlist the conclusions as follow:

Effect of solvents nature

- The XRD analyses indicate that all NiO films are polycrystalline structure and (111) plane is preferential orientation with strong intensity
- The grain size of films is found to be in the range 22-39 nm.
- All films showed a high optical transparency between 84% and 71% in the visible region.
- The calculated band gap was in the range 3.58 to 3.65 eV.
- The film elaborated using the de-ionized water solvent present maximum value of the conductivity compared with other solvents used.

Effect of precursor concentration

- The obtained films preserve their (111) preferential orientation.
- The best crystallinity is found for films prepared at 0.1M concentration.
- FT-IR analysis of spectra confirmed the existence of Ni-O bonds vibrations modes in the composition of the product.
- Transmittance spectra showed that transparency of the films ranged from 57 to 88%.

- Band gap energy of the films decreases from 3.68 to 3.60 eV
- The electrical conductivity is varied from 0.11 to 0.53 $\Omega^{-1} \text{ cm}^{-1}$. The high electrical conductivity is obtained for the film deposited at 0.1M.
- The elaborated films, having p-type character.

Effect of sprayed solution volume

- XRD results show that the deposited film with the volume lower than 10 ml was amorphous structure.
- Thin films structure become polycrystalline with cubic structure and (111) as a preferential orientation with volume upper than 10 ml.
- The grain size increased with increasing volume solution averaged in 10.13-27.81nm.
- FT-IR analysis of product confirms the NiO bond formation
- All films exhibit an average optical transparency between 50% and 80%.
- The band gap values were ranged in 3.38-3.62eV.
- The resistivity of NiO films decreases from 52.208 to 8.662 ($\Omega \cdot \text{cm}$) with the increase in precursor solution volume from 5 to 30 ml, and inversely with grain size.

Effect of Copper doped NiO thin films

- XRD characterization revealed that the undoped and Cu doped NiO thin films are polycrystalline with FCC structure.
- A decrease in the crystallite size from 37.1 to 11.7 nm as dopant concentration increased.
- SEM reveals that the Cu-doped NiO films become dense, smooth, with an increased agglomeration upon Cu concentration.
- FTIR measurements proved of absorbed bands related to NiO and CuO structure.

A decrease in the average optical transmission of the films from 64% to 35% with increased Cu concentration.

- The optical band gaps are ranged in 3.62-3.95eV.
- The PL spectra reveal the presence of peaks related to defects of Cu doping in NiO structure.
- All films are a p-type semiconductor and their conductivity increased with increasing the Cu doping level.

Effect of Lithium doped NiO thin films

- XRD results studies confirmed that the deposited film is mostly polycrystalline in all cases.
- No impurity peaks are identified from the XRD pattern.
- The grain size of the NiO thin films varies between 21.99 and 35.19 nm was affected by Li concentration.
- FTIR measurements devoted the presence of bands corresponding to NiO and LiO₂ structure.
- All films exhibit a high optical transparency and transmittance is found to decrease with the increase in Li concentration between 70% and 87%.
- Calculated band gap has been found to decrease with the increase in the Li concentration from 3.84 to 3.57 eV.
- The room temperature PL spectra reveal two main emissions located at 416 and 443 nm for undoped NiO, and appearance of new peaks shifted as Li doping concentration increases from 0 to 20 %.
- The resistivity has been found to decrease with the increase in Li concentration, giving the lowest value in case of 20% Li doping.

In summary, we concluded that the results obtained from structural, optical, and electrical measurements are found to be in good accord with the results obtained by the previous researcher and confirm that NiO films are feasible candidates for optoelectronic applications like a transparent conductor, light emitting devices, smart window and solar cells.

Suggestions for future work:

- Future work may be focused to study of co-doped NiO thin films in order to improve several optoelectronic properties of NiO thin films.
- More extensive characterizations are necessary such us (Raman spectroscopy, measurements of Hall effect, study of the current-voltage (I–V) characteristics as function of temperature, etc...).
- Application of the deposited films in, PN junction, laser diode, gas sensor, photocatalyst and antibacterial etc...

Publications

Publications

[1] **S. Benhamida**, B. Benhaoua, R. Barir, A. Rahal, A. Benhaoua, Effect of Sprayed Solution Volume on Structural and Optical Properties of Nickel Oxide Thin Films, Journal of Nano- and Electronic Physics, 9,3, (2017).03004.

[2] R. Barir, B. Benhaoua, **S. Benhamida**, A. Rahal, T. Sahraoui, R. Gheriani, Effect of precursor concentration on structural optical and electrical properties of NiO thin films prepared by spray pyrolysis, Journal of Nanomaterials, Volume 2017, Article ID 5204639.

ABSTRACT:

The aim of this thesis focused on the elaboration and characterization of nickel oxide (NiO) thin films using spray pyrolysis method at 500°C heated glass substrate. In order to study and optimize the spray deposition condition, the effect of preparative parameters such as solvents nature, the concentration of precursor and volume of the sprayed solution on structural, optical and electrical properties of undoped NiO thin films will be carried in this work. Furthermore, to enhance some characteristics of NiO materials, the incorporation of dopant in the materials are the effective way to change several physical properties (transparency, conductivity and defect structure...etc). In this study, Copper (Cu) and lithium (Li) doped nickel oxide thin films were elaborated using spray pyrolysis technique. The dependence of Cu and Li doping concentration on the structural, optical, photoluminescence and electrical properties of NiO thin films will be reported. X-ray diffraction (XRD), UV-visible spectrophotometer, Fourier transformed infrared (FT-IR) spectroscopy, photoluminescence (PL) spectroscopy, Seebeck effect and four-point probe method were used to characterize the deposited films.

The obtained results show that:

- The XRD analysis indicated that undoped NiO films deposited at different solvent nature present polycrystalline nature with (111) preferential orientation. The crystallite size of films varies between 22-39 nm as function of solvent nature. All films exhibit a high optical transparency between 84% and 71% in the visible range. However, the optical band gap was found to vary in the range 3.58 to 3.65 eV. The obtained results confirm that the films prepared with de-ionized water have better crystallinity, with good optical and electrical properties.
- With variation of precursor concentration, the (111) peak intensity becomes more significant, when precursor concentration reaches 0.1 M leading to an increment in NiO crystallite size close to 37nm. FT-IR analysis of spectra confirmed the existence of Ni-O bonds vibrations modes. The band gap energy of the films decreases from 3.68 to 3.60 eV with increasing precursor concentration.
- From XRD results it was shown that the deposited thin film with the volume lower than 10 ml was amorphous and with increasing volume up to 10 ml NiO thin films structure become polycrystalline with cubic structure and (111) as preferential orientation. All films exhibit an average optical transparency between 50% and 80% in the visible range and their band gap values were ranged in 3.38-3.62eV. The minimum resistivity of the NiO films is 8.662 Ω .cm from film prepared at 30ml solution volume.
- the XRD patterns showed that undoped and doped NiO films structure are polycrystalline with (111) preferred orientation and the observation of shift orientation of the peaks after doping with Cu, whereas doping with Li in the NiO material did not change position of the diffraction peaks significantly. The grain size decreases as doping concentration increase in NiO samples. From the transmittance spectra, it observed that the optical transparency decrease with the increase of Cu or Li doping concentration. The band gap energy is found to vary from 3.62-3.95eV in the case of Cu doped NiO films, however from the films prepared with Li doped NiO films the band gap is ranged from 3.84 to 3.57 eV. The type conductivity of all samples are P-type semiconductor, whereas a low conductivity was obtained for the undoped NiO thin films, after doping the conductivity increases as a function of Cu or Li doping level.

Keywords: NiO thin films; Cu; Li; Spray Pyrolysis; X-ray diffraction; FTIR.

RESUME :

Le but de cette thèse a porté sur l'élaboration et de caractérisation des couches minces d'oxyde de nickel (NiO) en utilisant la méthode spray pyrolyse dans des substrats en verre chauffé à 500°C. Afin d'étudier et d'optimiser les conditions de dépôt, l'effet des paramètres de préparation tels que la nature des solvants, la concentration de précurseur et le volume de la solution pulvérisée sur les propriétés structurales, optiques et électriques des couches minces de NiO. En plus, pour améliorer certaines caractéristiques de ce matériau, l'incorporation de dopants dans le matériau constitue le moyen efficace pour modifier plusieurs propriétés physiques (transparence, la conductivité et la structure de défauts, etc.). Dans cette étude, des couches minces d'oxyde de nickel dopées par cuivre (Cu) et par lithium (Li) ont été élaborées en utilisant la technique de spray pyrolyse. La dépendance de la concentration de dopage par Cu et par Li sur les propriétés structurales, optiques, photo-luminescentes et électriques des couches minces de NiO sera rapportée. La diffraction des rayons X (DRX), le spectrophotomètre UV-visible, la spectroscopie infrarouge par transformée de Fourier (FT-IR), la spectroscopie de photoluminescence (PL), l'effet Seebeck et la méthode de quatre points ont été utilisés pour caractériser les films déposés.

Les résultats obtenus montrent que:

- L'analyse par DRX a montré que les films de NiO non dopés déposés à des solvants différents présentent un caractère polycristallin avec une orientation préférentielle (111). La taille de cristallite des films varie entre 22 et 39 nm en fonction de la nature du solvant. Tous les films présentent une transparence optique élevée entre 84% et 71% dans le visible. Cependant, il a été constaté que la bande interdite optique varie dans la plage de 3,58 à 3,65 eV. Les résultats obtenus confirment que les films préparés avec de l'eau dé-ionisée ont une meilleure cristallinité, avec de bonnes propriétés optiques et électriques.
- Avec la variation de la concentration de précurseurs, l'intensité maximale sur le plan (111) devient plus importante lorsque la concentration de précurseurs atteint 0,1 M, entraînant une augmentation de la taille de cristallite de NiO proche de 37 nm. L'analyse FT-IR des spectres a confirmé l'existence de modes de vibrations des liaisons Ni-O. L'énergie de la bande interdite des films diminue de 3,68 à 3,60 eV avec une concentration croissante de précurseurs.
- À partir des résultats XRD, il a été montré que le film mince déposé de volume inférieur à 10 ml était amorphe et que, avec un volume croissant, jusqu'à 10 ml, la structure des couches minces NiO devient polycristalline avec une structure cubique et le plan (111) possède une orientation préférentielle. Tous les films déposés présentent une transparence optique moyenne entre 50% et 80% dans le visible et leurs valeurs de bande interdite sont comprises entre 3,38 et 3,62 eV. La résistivité minimale des films de NiO est de 8,662 Ω .cm à partir du film préparé à 30 ml de la solution pulvériser.
- les diagrammes de XRD ont montré que les films de NiO non dopés et dopés sont de structure polycristalline avec l'orientation (111) préférée et l'observation de décalage des pics après le dopage avec Cu, alors que le dopage par Li dans le matériau NiO n'a pas modifié la position des pics de diffraction significativement. La taille des grains diminue avec l'augmentation de la concentration de dopage dans les échantillons de NiO. À partir des spectres de transmittance, il a été observé que la transparence optique diminuait avec l'augmentation de la concentration en dopage de Li ou Cu. L'énergie de la bande interdite varie de 3,62 à 3,95 eV dans le cas des films de NiO dopés au Cu, cependant, les films de NiO dopés par Li, possèdent d'une bande interdite comprise entre 3,84 et 3,57 eV. Le type de conductivité de tous les échantillons est un semi-conducteur de type P, tandis qu'une faible conductivité a été obtenue pour les couches minces NiO non dopées, après le dopage, la conductivité augmente en fonction de niveau de dopage par Cu ou par Li.

Mots clé: NiO couche minces; Cu; Li; Spray Pyrolyse; X-ray diffraction; FTIR.

المخلص :

يهدف هذا العمل إلى ترسيب طبقات رقيقة من أكسيد النيكل (NiO) باستخدام طريقة الرش الحراري على مساند زجاجية تم تسخينها لتصل إلى 500°C. من أجل دراسة وتحسين شروط الترسيب، تم التركيز على دراسة بعض العوامل التالية: طبيعة المذيب، تركيز المحلول وحجم محلول الرش على الخواص البنيوية، البصريّة والكهربائية للأغشية الرقيقة من أكسيد النيكل. و من أجل تحسين خصائص المادة المرسيبة، تم إضافة بعض المواد المطعمة في المادة حيث يشكل هذا وسيلة فعالة لتحسين العديد من الخصائص الفيزيائية (الشفافية ، الناقلية الكهربائية والعيوب البلورية ... إلخ). في هذه الدراسة ، تم تطوير طبقات رقيقة من أكسيد النيكل المطعمة بالنحاس (Cu) و الليثيوم (Li) باستخدام تقنية الرش الحراري. كما تم دراسة تأثير تركيز التطعيم ب: Cu و Li على الخصائص البنيوية، البصرية، الاستشعاعية والكهربائية لطبقات NiO الرقيقة. ومن أجل هذا ،تم استعمال الأجهزة التالية: حيود الأشعة السينية (XRD)، مطياف الأشعة فوق البنفسجية المرئية ، مطياف الأشعة تحت الحمراء بواسطة تحويل فورييه (FT-IR)، مطياف الإستشعاع (PL)، تأثير سيبيك (Seebeck) وطريقة المسابر الأربعة. تظهر النتائج التي تم الحصول عليها:

- أظهر تحليل الأشعة السينية أن الطبقات الرقيقة لNiO غير الم طعمة الم حضرة بواسطة مذيبات مختلفة ذات تبلور متعدد مع اتجاه بلوري تفضيلي نحو المتجه (111). حجم البلورات المتحصل عليها يتراوح بين 22 و 39 نانومتر حسب طبيعة المذيب. جميع الطبقات الرقيقة ذات شفافية بصرية عالية بين 71 و 84% في المجال المرئي. وجد أن طاقة العصابة الممنوعة كانت بين 3.58 إلى 3.65 إلكترون فولت. تؤكد النتائج التي تم الحصول عليها أن الطبقات الرقيقة المحضرة بالماء ثنائي التقطير لها تبلور أفضل ، مع خصائص بصرية وكهربائية جيدة.
- مع تغيير تركيز المحلول، وجد أن أقصى شدة للمستوى البلوري (111) هي عند التركيز 0.1 مولاري ، و هذا ما يؤدي إلى زيادة في حجم البلورات NiO تصل 37 نانومتر. أكد تحليل FT-IR للأطياف وجود أنماط اهتزاز للرابطة البلورية Ni-O. بينما تنخفض طاقة العصابة الممنوعة للشرائح من 3.68 إلى 3.60 إلكترون فولت مع زيادة تركيز المحلول.
- تبين من تحليل نتائج الأشعة السينية XRD أن الشرائح المحضرة عند حجم المحلول أقل من 10 مل أنها غير متبلورة، و مع زيادة حجم المحلول، تصبح بنية الشرائح متبلورة ذات تركيب بلوري متمركز الأوجه لبلورة أكسيد النيكل، مع ملاحظة أن المستوى البلوري (111) هو التوجه المفضل لأغلب الشرائح. بيّنت النتائج أن جميع الشرائح تتمتع بشفافية بصرية متوسطة تتراوح بين 50% و 80% في المجال المرئي، بينما تتراوح قيم طاقة العصابة الممنوعة بين 3.38 و 3.62 إلكترون فولت. الحد الأدنى للمقاومية الكهربائية تم تسجيله عند الشرائح المحضرة بحجم 30 مل و كانت قيمتها 8.662Ω.cm.
- تبين من خلال ما أظهرته نتائج الأشعة السينية XRD أن جميع الطبقات الرقيقة المطعمة و الغير مطعمة ذات تبلور متعدد و توجه مفضل نحو المستوى البلوري (111)، لوحظ أيضا انزياح في زوايا الانعراج عند زيادة التطعيم بشوارد النحاس، بينما لا نلاحظ تغييرات معتبرة في زوايا الانعراج عند التطعيم بشوارد الليثيوم. يتناقص حجم الحبيبات مع زيادة تركيز التطعيم في عينات أكسيد النيكل. أظهرت أطياف النفاذية أن الشفافية البصرية تنخفض مع زيادة تركيز التطعيم بشوارد النحاس و الليثيوم. تتراوح قيم طاقة العصابة الممنوعة من 3.62 إلى 3.95 إلكترون فولت عند تطعيم طبقات أكسيد النيكل NiO بشوارد النحاس ، بينما كانت قيم طاقة العصابة الممنوعة تتراوح بين 3.84 و 3.57 إلكترون فولت عند تطعيم طبقات أكسيد النيكل NiO بشوارد الليثيوم. أظهرت النتائج أن نوعية التوصيل في جميع العينات هي من النوع P، في حين تم الحصول على موصلية منخفضة عند العينات الغير مطعمة، بينما لوحظ تحسن في الناقلية الكهربائية لعينات أكسيد النيكل NiO عند الزيادة في تركيز التطعيم بشوارد النحاس أو الليثيوم.

الكلمات المفتاحية: طبقات أكسيد النيكل NiO، النحاس، الليثيوم، الرش الحراري، الأشعة السينية، الأشعة تحت الحمراء بتحويل فورييه.